2021

Thermal Performance of AlGaN/GaN Based Power Switching Devices for Transformerless Inverters

Mahesh B. Manandhar
University of Denver

THERMAL PERFORMANCE OF AlGaN/GaN BASED POWER SWITCHING DEVICES FOR TRANSFORMERLESS INVERTERS

_____

A Dissertation

Presented to

the Faculty of the Daniel Felix Ritchie School of Engineering and Computer Science

University of Denver

_____

In Partial Fulfillment

of the Requirements for the Degree

Doctor of Philosophy

_____

by

Mahesh B. Manandhar

August 2021

Advisor: Dr. Mohammad Matin

Author: Mahesh B. Manandhar
Title: THERMAL PERFORMANCE OF AlGaN/GaN BASED POWER SWITCHING DEVICES FOR TRANSFORMERLESS INVERTERS
Advisor: Dr. Mohammad Matin
Degree Date: August 2021

Abstract

Wide Bandgap (WBG) semiconductors like Silicon Carbide (SiC), Gallium Nitride (GaN) and Aluminum Gallium Nitride (AlGaN) have superior material properties as compared to Silicon (Si) like higher electrical breakdown voltages and bandgap energies as well as lower leakage currents as compared to Si which make them ideal to operate at higher voltage with lower thermal losses. These properties make WBG materials ideal for power devices like Vertical Double-diffused Metal Oxide Semiconductor Field Effect Transistors (VDMOSFETs). The use of digital prototyping through computer simulation increases the speed and flexibility of the design iterations while reducing the cost and time required for the design process. COMSOL Multiphysics is a Finite Element Method simulation software that has capabilities of combining different physics interfaces to simulate the effects of multiple interdependent physical phenomena. The use of these materials in switching devices like VDMOSFETs have been modelled in COMSOL Multiphysics in 2D and 3D for the purposes of this research dissertation. The electrical and thermal advantages of WBG materials, specifically SiC, GaN and AlGaN, as compared to Si as semiconductor materials for VDMOSFET structures for the exact same VDMOSFET structures are demonstrated and quantified from the results obtained.

The inverter is the most important component in a Photo Voltaic (PV) system that needs to be improved. Transformerless inverters have higher efficiencies at lower weight and size specifications as compared to ones with transformers. A modified topology of a single phase transformerless inverter with new current paths and improved efficiencies is proposed and its performance is analyzed in PSIM software with Si and WBG material power switching devices. The advantages of the WBG devices over Si in terms of power losses are also exhibited in this research. The power losses obtained from the models in PSIM are then used as inputs to COMSOL models for temperature comparisons of the switching device modules. The improved temperature performance of the WBG devices are then demonstrated by the reduction in heatsink requirements as compared to identical Si switching modules.

Acknowledgements

I would like to acknowledge my deepest gratitude to Dr. Mohammad Matin, my academic advisor, for his constant supervision and guidance throughout the entirety of my research period. His mentorship and encouragement has been vital in the pursuit of my degree. My colleagues Dr. Khaled Alatawi and Dr. Fahad Almasoudi deserve my utmost gratitude for all their collaboration and inputs to my own research.

I would like to thank my graduate committee, Dr. David Gao, Dr. Haluk Ogmen and Dr. Yun Bo Yi for their guidance and expertise throughout the dissertation procedures. I must express my appreciation to Tim Sheu, our IT director, and the entire COMSOL support team for being patient with me and helping me with all my constant queries.

Lastly, I would like to thank my family and friends for all their encouragement and support.

Table of Contents

List of Figures

List of Acronyms

2D	Two Dimensional
3D	Three Dimensional
4G	Fourth Generation
5G	Fifth Generation
AC	Alternating Current
AlGaN	Aluminum Gallium Nitride
AlGaAs	Aluminum Gallium Arsenide
AlN	Aluminum Nitride
BFOM	Baliga Figure Of Merit
BJT	Bipolar Junction Transistor
CAD	Computer-Aided Design
CM	Common Mode
C_{MV}	Common Mode Voltage
C_{PV}	Stray PV Capacitance
CTE	Coefficient of Thermal Expansion
DC	Direct Current
DMOS	Double-diffused Metal Oxide Semiconductor
E_c	Conduction Band Energy
EMI	Electromagnetic Interference
EV	Electric Vehicle
FEA	Finite Element Analysis

FEM	Finite Element Method
FET	Field Effect Transistor
f_G	Grid frequency
f_{sw}	Switching frequency
Ga_2O_3	Gallium Oxide
GaN	Gallium Nitride
GaAs	Gallium Arsenide
HEMT	High Electron Mobility Transistor
HEV	Hybrid Electric Vehicle
HFET	Heterojunction Field Effect Transistor
HTE	High Temperature Electronics
IC	Integrated Circuit
I_{CM}	Common Mode Current
IGBT	Insulated Gate Bipolar Transistor
InN	Indium Nitride
JFET	Junction Field Effect Transistor
LDMOSFET	Lateral Double-Diffused MOSFET
LED	Light Emitting Diode
MEMS	Micro Electro Mechanical System
MESFET	Metal Semiconductor Field Effect Transistor
MOSFET	Metal Oxide Field Effect Transistor
PV	Photovoltaic

$R_{DS(ON)}$	Drain to Source ON Resistance
RMS	Root Mean Squared
SAW	Surface Acoustic Wave
SCR	Silicon Controlled Rectifier
Si	Silicon
SiC	Silicon Carbide
SOA	Safe Operating Area
THD	Total Harmonic Distortion
UBWG	Ultra Wide Bandgap
UV	Ultra Violet
VDMOSFET	Vertical Double-diffused MOSFET
VDS	Drain to Source Voltage
VGS	Gate to Source Voltage
WBG	Wide Bandgap

1. Introduction

1.1 Background

Power electronics is an important bridge between the different stages of electrical energy generation and consumption. Silicon (Si) based semiconductor technology has been the primary basis for power electronics converters used within the different transformation stages of electrical energy. Although Silicon based power devices have a well-established market, they have been known to be matured in terms of maximum voltage and high operating temperatures and so, newer power devices with higher power and temperature functionalities are needed to fulfill these requirements [1] [2] [3] [4]. Wide Bandgap (WBG) materials like Silicon Carbide (SiC), Gallium Nitride (GaN) and alloys of Aluminum Nitride (AlN) and GaN (i.e. AlGaN) have much better material properties than Silicon in terms of operating temperature, breakdown voltage and switching frequencies [1] [2] [3] [5]. These materials have been used in power devices like Bipolar Junction Transistors (BJTs), Metal Oxide Field Effect Transistors (MOSFETs), Metal Semiconductor Field Effect Transistors (MESFETs), Junction Field Effect Transistors (JFETs), and High Electron Mobility Transistors (HEMTs) as reported in literature [1] [2] [5]. The higher bandgap energies of WBG materials results in higher carrier mobility and higher operating temperature before breakdown [1] [2] [3] [6]. WBG materials have higher electrical/thermal conductivities and breakdown voltages that

reduces their electrical and thermal resistances while increasing the switching frequency capabilities [1] [2] [6]. WBG semiconductor devices are the less expensive simpler options as opposed to using complex techniques to stretch Silicon's limited capabilities in this regard [1] [3] [4] [7] [8].

BJTs are simpler in design as compared to other switching devices but as they are current controlled devices, they suffer from leakage current problems [9]. MOSFETs are voltage controlled and so do not suffer from current leakage problems [9] [10]. MOSFETs have higher switching speeds but have higher power losses at high currents [9] [10]. Insulated Gate Bipolar Transistors (IGBTs) are a hybrid of BJTs and MOSFETs and are used in medium power-medium frequency devices but are slower than MOSFETs [9] [10] [11].

Power MOSFETs are majority carrier Field Effect Transistors (FETs) that can operate at low gate currents with very high input impedances and fast switching capabilities [9] [10] [12]. Lateral Double-Diffused MOSFETs (LDMOSFETs) and Vertical Double-diffused MOSFET (VDMOSFETs) are MOSFETs that employ double-diffusion doping techniques to achieve high precision in channel length [13] [14]. The major difference between LDMOSFET and VDMOSFET is the location of the Drain contact relative to the Source terminal. VDMOSFETs have their Drain at the bottom of the device substrate as compared to the Drain being laterally across the channel from the source in LDMOSFETs [14]. VDMOSFETs can have higher operational voltages without breaking down due to the advantage of having a bigger separation between the Drain and Source terminals within the same surface area [12] [14] [15]. The Source area can be

increased to reduce the current density and overheating problems in the case of VDMOSFETs [14].

The development life cycle of a device consists of multiple stages starting from the conception of the device design and ending in the manufacturing of the final product. The use of digital prototyping software can accelerate the design process by reducing the time and cost multiple iterations in design, feedback and manufacturing processes [16] [17]. The usage of software to simulate power devices has been done in software like SPICE, PISCES-II, Silvaco© ATLAS Technology Computer-Aided Design (TCAD), COMSOL Multiphysics etc., as reported in literature [15] [16] [17] [18] [19] [20]. These software have been used with different techniques like Finite Element Analysis (FEA) and other numerical methods along with CAD tools to simulate electrical and thermal characteristics of WBG power MOSFETs.

The conversion of electrical energy from Direct Current (DC) to Alternating Current (AC) can be done from different DC sources like Photovoltaic (PV) solar arrays or batteries. The inverters that convert PV voltage to AC Isolated inverters can either be single phase or 3-phase converters. Such inverters can have galvanic isolation between output and input terminals with transformers. However, the use of transformers cause reduction in efficiency while increasing the size, weight and cost of the system [21]. Non-isolated inverters without transformers have reduced size and weight and have higher efficiencies at lower costs but lack galvanic isolation. In such non-galvanically isolated systems, high frequency common mode (CM) voltage causes leakage current to flow through parasitic capacitances within the system which leads to unwanted power losses,

safety issues as well as Electromagnetic Interference (EMI) [21] [22] [23] [24]. The topology and switching techniques of such transformer-less inverters need to be efficient to remove the leakage currents that lead to power losses.

1.2 Problem Statement

The power switching devices used in inverters like HEMTs and MOSFETs dissipate leakage current losses in terms of heat [25]. In addition to losing energy in the form of heat, the electrical performance as well as device structural stability can get compromised due to high temperatures. The use of WBG switching devices as compared to Si devices have shown to have lower power losses as well as lower temperatures of the devices themselves [16] [17] [26] [27]. Physical testing of such power switching devices requires the use of expensive equipment and a long time frame of experimental observations. The use of Digital Prototyping software like COMSOL and PSIM can accurately predict the power losses incurred at specific operating conditions so that analysis of the merits of different semiconductor materials as well as Inverter topologies can be done faster and cheaper.

1.3 Methodology

This dissertation discusses the use of COMSOL for the study of the thermal performance of different WBG materials as semiconductors for VDMOSFETs. COMSOL divides the geometry of the VDMOSFET into multiple subdomains and evaluates the Joule heating caused by currents flowing within the device in each of the

subdomains by solving the corresponding differential equations. The input parameters like material properties, initial dopant concentrations and different terminal voltages are used to solve the equations. The merits of WBG materials, specifically SiC, GaN and AlGaN are discussed for the VDMOSFET structure as compared to Silicon. The electrical circuit simulator PSIM is used to compare different WBG power switching device modules with those made of Silicon and their power losses are calculated for a specific inverter topology. These power loss values are then added to COMSOL as inputs for heat sources in the switching modules to analyze the thermal performance of each material device.

1.4 Motivation

Power switching devices have been modelled using different simulation software like Silvaco© ATLAS Technology Computer-Aided Design (TCAD), SPICE, PISCES-II, COMSOL Multiphysics etc. as reported in literature [15] [18] [19] [20]. FEA analysis with CAD tools have been used to simulate electrical and thermal characteristics of specific WBG power MOSFETs in 2D but comparative studies under the same conditions for different WBG materials has not been done in either 2D or 3D. AlGaN has higher bandgap energy (E_G) as compared to SiC and GaN and its bandgap energy values lie between AlN and GaN, depending on the molar concentrations of Al and Ga [28]. AlGaN is classified as Ultra Wide Bandgap (UBWG) due to its E_G value being greater than 3.4 eV and AlGaN devices have shown promising electrical performance as compared to their SiC and GaN counterparts [28] [29] [30]. The modified H5 Inverter topology with

WBG materials have been tested with SiC and GaN with improved efficiencies as compared to Si but not with AlGaN. The use of PSIM simplifies power loss calculations by applying the device characteristics available from datasheets. The prime motivation for this dissertation is to compare the thermal performance of AlGaN VDMOSFET structures with other semiconductor materials in COMSOL and then to compare AlGaN power device modules in the modified H5 Inverter topology using PSIM. The power loss calculations from PSIM are then used to compare the thermal performance of the modules and heatsink requirements with other semiconductor material devices in COMSOL.

1.4 Objectives

The main objectives of this research work are:

- To compare different WBG devices in terms of temperature profiles for different operating voltages and dopant concentrations.
- To find the merit of AlGaN/GaN power switching devices.
- To find the merit of the modified H5 inverter topology with an AlGaN/GaN HEMT module in terms of power losses.
- To use power losses to simulate thermal losses and cooling requirements.

1.5 Limitations

The results of the simulations are dependent on the input parameters set in the models. As such, the results cannot accurately predict real world deviations of individual

power devices. The assumptions, parameters and initial conditions for the models are further discussed in the Methods chapters and are justified accordingly. Structural stability of device structures are not simulated in the models and only temperatures are solved for in COMSOL. Steady state studies were analyzed while time dependence of the results were not considered. The physical dimensions, input voltage conditions and doping concentrations for all the devices in each comparative simulation were kept the same for all the materials. Real life semiconductor devices of different materials do not have the same dimensions, voltage inputs and dopant concentrations. This was done to make the comparisons between the materials as simple as possible. Economic feasibility was also not studied for the scope of this research work.

1.6 Dissertation Organization

This dissertation consists of chapters differentiated by their respective topics. The first chapter is an introduction to the research work that has been done. Chapter 2 reviews scientific literature related to the research work. Chapter 3 discusses the methodology of the studies in COMSOL and PSIM in detail. Chapter 4 consists of results of the simulations and discusses these results. This report concludes with a summary of the research work in Chapter 5 and future work.

2. Literature Review

2.1 Semiconductor Power Devices

The semiconductor industry had a global market of $426 billion in 2020 and is estimated to rise up to $452 billion in the year 2021 with a third of the market being covered by communication electronics as shown in Figure 1 [31]. With an estimated 50% of the global electricity being controlled by power devices inside electronics in the industrial, medical, consumer, and many other sectors, these devices have an enormous impact on the world economy [32]. The innovation of solid state devices began in the 1950s based on Silicon as the semiconductor material for power devices [32]. These power devices convert electrical energy from one form to another and are considered breakthrough technologies since the start of electrical power systems [33].

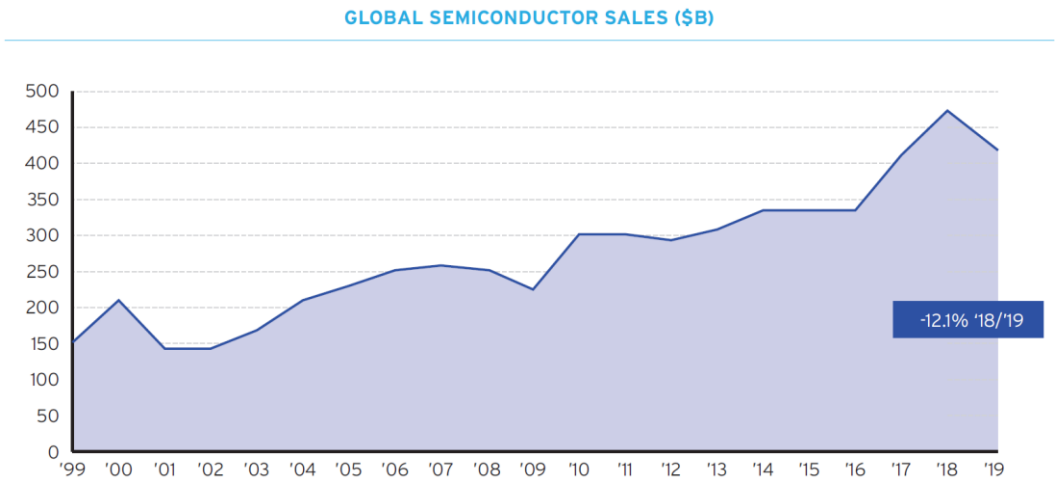

Figure 1. Global Semiconductor sales from 1999 to 2019.

The field of power electronics came into existence about 70 years ago, with the invention and commercial introduction of Silicon Controlled Rectifiers (SCR) and Bipolar Junction Transistors [32] [33] [34]. By the 1970s power BJTs with maximum current capabilities of hundreds of Amps and blocking voltages of over 500 V had become available [32]. BJTs had the disadvantage of low current gains and MOSFETs became the next new power switching technology [32] [33] [35]. The power MOSFET also became available in the 1970s and although it was initially predicted to replace all BJTs as power devices owing to its fast switching speed and high input impedance, the power MOSFET could only rule the high frequency switching low power market but failed to capture the high voltage market [32] [35]. This is due to the fact that power MOSFET ON-Resistance values go up very rapidly with increase in the breakdown voltage which increases conduction losses and reduces the overall efficiency of the system [32] [35].

The IGBT was the next innovation in power switching devices first introduced in the early 1980s and became more widely adopted for most medium power applications [32]. IGBTs are a combination of BJTs and MOSFETs into a single Integrated Circuit (IC) and have very highs power gains, high input impedances with a wide range of switching speeds dependent on the operating frequency required by the application [32] [35] [36]. Other types of Field Effect Transistors (FETs) like JFETs, MESFETs and HEMTs have also matured in the markets with HEMTs emerging from the recent developments in WBG semiconductor technology [2] [35]. HEMTs employ a heterojunction of two different semiconductors as the conduction channel with WBG

materials like GaN and AlGaN and are leading the way in new research developments [37] [38] [39] [40]. The inherent material properties and device structure of the WBG HEMTs allow for low ON resistances, high switching frequency capabilities and high blocking voltages and thus have attracted attention in the research sectors [2] [37] [38] [39] [40].

2.1.1 MOSFET structures

Low power MOSFETs have a structure as shown in Figure 2 with the Source, Drain and Gate Terminals situated lateral to each other and a single region for either the n-type or p-type dopants [33]. These MOSFETs operate in the Enhancement Mode i.e. the device is normally OFF and only turns ON when a Gate to Source Voltage (VGS) greater than the Threshold Voltage is applied [33]. These structures are not suitable for high Drain to Source Voltage (VDS) applications and for voltage applications of over 10 V, a structure called the DMOS (Double-diffused MOS) as shown in figure 3 is used [33]. The difference between the Lateral MOSFET and the LDMOSFET structure is the addition of the lightly doped n^- drift region which allows for higher breakdown voltage with better reduced distortion [41]. Although LDMOSFETs are used in power ICs in a single monolith structure, they suffer from low current capacity and instabilities caused due to trapped electrons [33] [41].

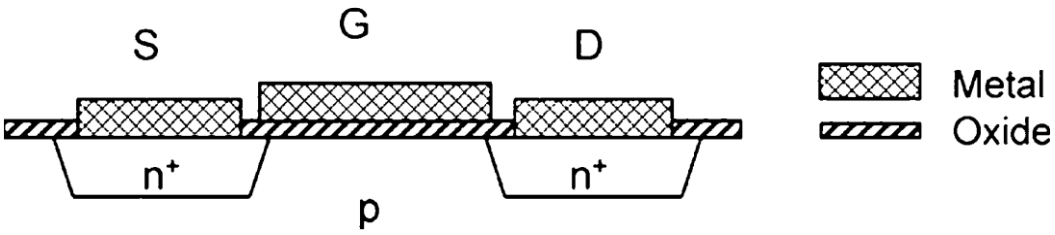

Figure 2. Cross section of Lateral MOSFET structure.

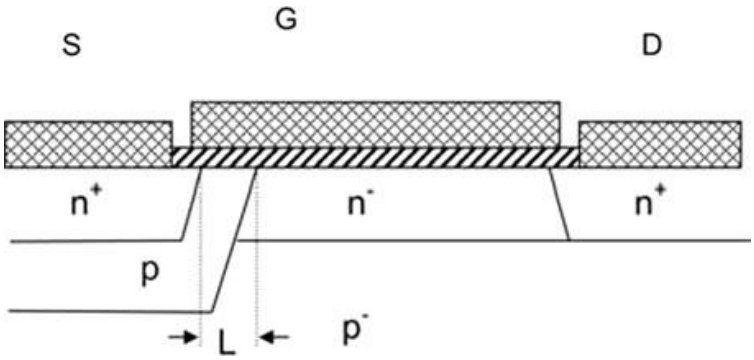

Figure 3. Cross section of LDMOSFET Structure.

The VDMOSFET structure (Figure 4) solves this issue of low current/power capacities as compared to the LDMOSFET while keeping the advantages of high voltage blocking and high switching frequency capabilities [32] [33]. The name for VDMOSFETs comes from the fact that the Drain terminal is vertically below the Gate and Source terminals on the upper surface and the electric field is applied vertically as opposed to laterally as in LDMOSFETs. The entire volume of the MOSFET structure can be utilized while the surface is used to form cells as shown in figure 5 [33]. Instead of having the entire surface act as the MOSFET without utilizing the volume as in LDMOSFETs, the VDMOSFET structure can have multiple MOSFET cells created within the volume [33].

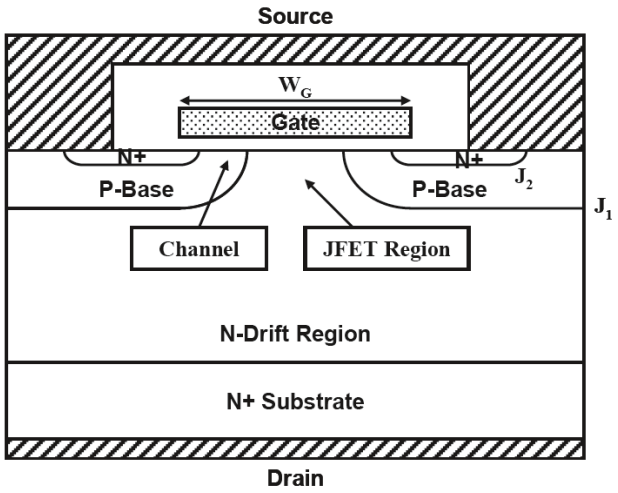

Figure 4. Cross section of VDMOSFET structure.

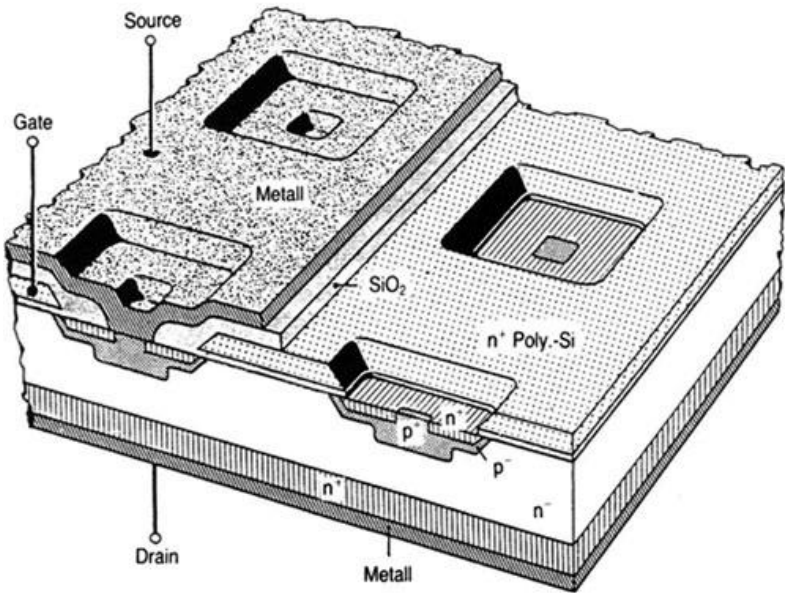

Figure 5. Cell structure of VDMOSFETs.

The drain current in the VDMOSFET structure is created when a positive VGS is applied. An inversion layer at the surface of the P-base region is created below the gate terminal which provides a path for movement of electrons from the source to the drain terminals [14] [33]. The larger separation between the Source and Drain terminals means

the VDMOSFET structure can withstand larger VDS before breakdown and lowers the current density as well. VDMOSFETs have comparatively larger ON-resistances which led to the development of trench-gate power MOSFETs starting in the 1990s [32]. The emergence of etching trenches in to semiconductor substrates gave rise to the trench-gate or U-MOSFET structure where the gate terminal is placed inside a trench after oxidation of the walls surrounding the terminal is completed as seen in Figure 6 [32]. The conduction mechanism of drain current for U-MOSFETs is similar to VDMOSFETs with the added benefit of having low ON resistances.

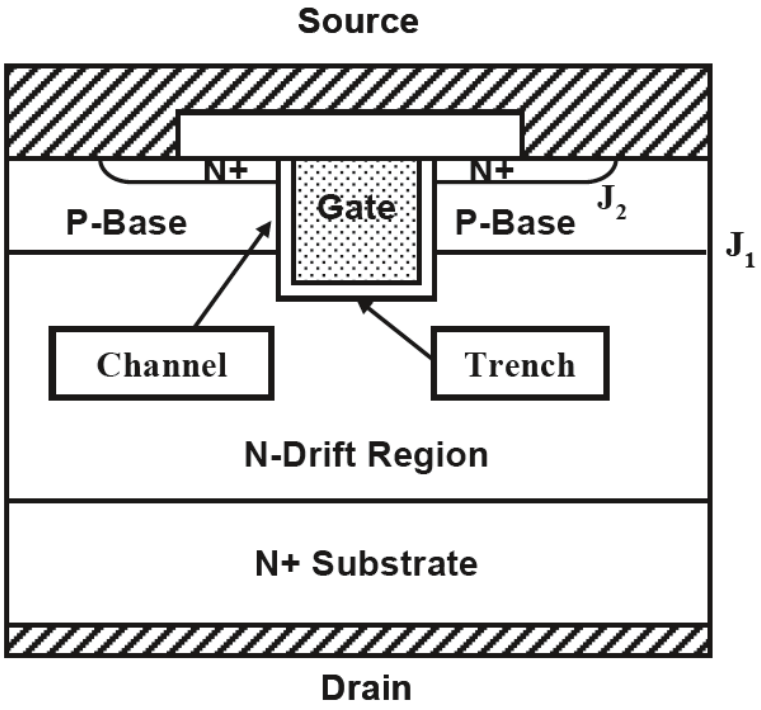

Figure 6. Cross section of U-MOSFET structure.

The improvement of the performance of VDMOSFETs has been a topic of research since the 1990s. The work in [42] aimed to reduce capacitive power losses in VDMOSFETs at high switching frequencies while [43] demonstrated the shift in

threshold voltages in VDMOSFETs under different biasing conditions. There are numerous examples of VDMOSFET structures with Si and WBG materials and their characterizations as reported in [44] for Silicon on Glass VDMOSFETs, [45] [46] [47] and many more on SiC VDMOSFET fabrication, characterization and testing.

2.1.2 HEMTs

A HEMT is a semiconductor device similar to other FET devices but differ on the way the conduction channel is created on the semiconductors. A typical FET consists of multiple semiconductor layers stacked on top of one another with the terminals on the top layer [48]. The arrangement of terminals, thickness of the material layers determine the type of FET device [48]. A HEMT device structure consists of a WBG semiconductor layer grown on top of another semiconductor material layer with a narrower bandgap which forms a heterojunction [48]. Takahashi Mimura of Fujitsu® first invented the concept of a HEMT in 1980 with GaAs as a replacement for high speed Si MOSFETs but HEMTs these days are made with materials like GaN, AlGaN and other WBG materials as well [48] [49] [50]. Although Diamond has much superior properties, GaAs, GaN and SiC are preferred as the material of choice for HEMTs owing to Diamond's high production and fabrication costs [48].

FET devices operate by controlling the current in the conduction channel by applying a VGS along the channel space [48]. On the other hand, the channel thickness is negligible in HEMTs and thus the channel is considered 2D instead of a 3D volume of the semiconductor material which is why the channel is called as a two-dimensional

electron gas or 2DEG [48]. The channel is not contained within the n-type material that forms the Schottky barrier which is a metal/semiconductor junction as in FET devices and instead exists in the undoped WBG semiconductor layer [49]. The High Electron Mobility name comes from the absence of doping which eliminates impurity scattering [49].

Figure 7 [51] shows a type of AlGaAs/GaAs HEMT structure while figure 8 [48] [49] shows the cross section and 3D view of one with AlGaN/GaN. Both HEMTs have a similar layered structure with a semi-insulating material serving as the base substrate and the terminals on the topmost layer. The wider bandgap material layer lies below the topmost layer with the narrower bandgap material above the base substrate. The semiconductor with the wider bandgap (AlGaN or AlGaAs) creates a heterojunction with the terminal metal contacts and also another heterojunction with the channel layer [49].

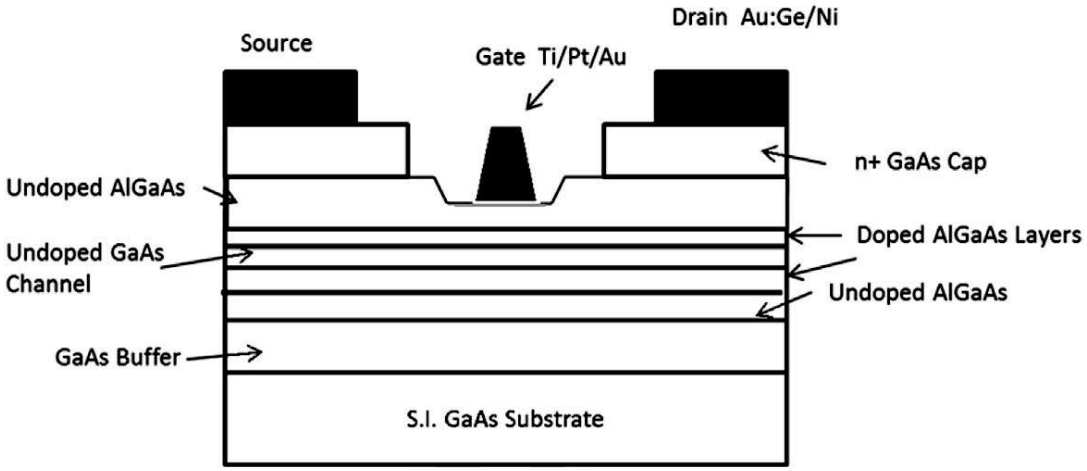

Figure 7. AlGaAs/GaAs HEMT cross section.

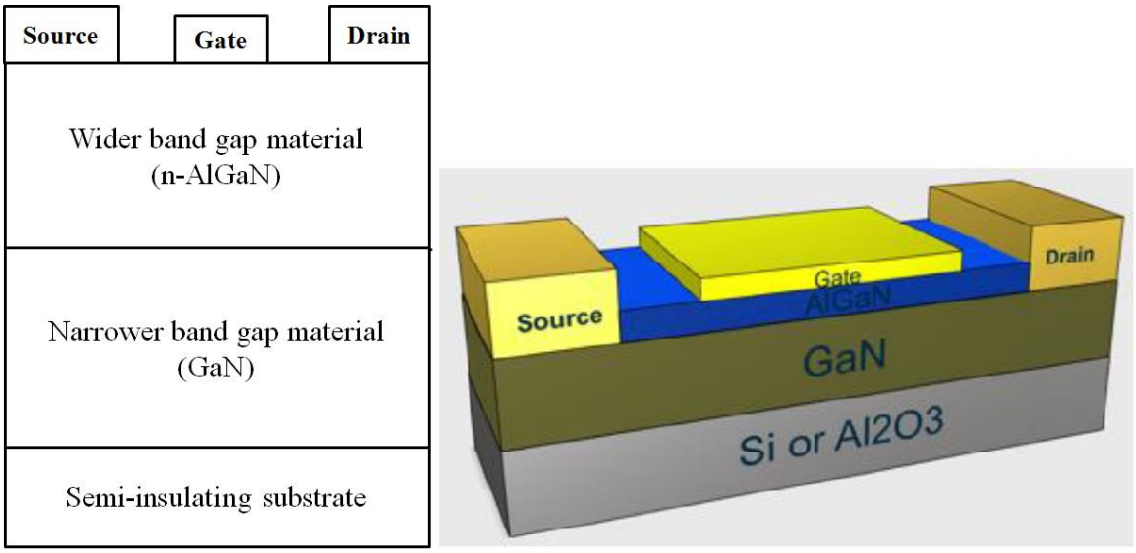

Figure 8. AlGaN/GaN HEMT Structure.

Electrons get transferred at the semiconductor heterojunction from the semiconductor with the higher conduction band energy (E_c) to the one with the lower E_c in order to occupy a lower energy state [49] [50]. This creates a discontinuity in the conduction band edge for the entire structure and forms quantum wells at the heterojunction which is where the 2DEG channel exists [48] [49] [50].

HEMTs have found a multitude of applications from radioastronomy and satellite receivers to cellphone RF amplifier circuits depending on the materials they use [52]. Although WBG material properties are better than Si, LDMOSFETs made of Si are extensively used in power amplifiers in the transmitters of radio base stations, due to their better ratio of price versus performance [48]. Si LDMOSFETs are currently the prime commercial semiconductor power devices for power amplifiers of base stations, fabricated by major companies [48]. However, AlGaN/GaN HEMTs are being projected to dethrone LDMOSFETs as the major power switching device owing to their higher switching frequency, current density capabilities as well as better efficiencies [48].

AlGaN/GaN HEMTs have high linearity and frequency range and a system with a single one of them can raise the efficiency to 28% from the efficiency of a system with three Si LDMOSFETs [48]. These WBG HEMTs have better performance attributes like low noise, high breakdown voltage, extreme high/low temperature operating conditions and so are ideal for high power Low Noise Amplifier (LNA) applications [48] [53]. GaN HEMTs have high current capabilities due to their 2DEG channels and can operate in either Enhancement mode (normally OFF) or Depletion mode (normally ON) [54]. HEMTs made with WBG and UWBG materials is an exciting field of research for both academia and manufacturers. Some of the many examples of works on characterization, fabrication and modeling of GaN, AlGaN, AlN HEMTs in literature are [55] [56] [57] [58] [59].

2.2 WBG Materials

High power semiconductor devices are the main components of electric power converters. Semiconductor devices like transistors and diodes are used in power converters as switches or rectifiers along with passive components to cater to different electric specifications like voltage, current and frequency requirements [60]. Sustainable technological development are in need of increase in electrical power efficiencies in and better energy savings which require better power converters. The devices and circuitry inside of the power converters come in a variety of size, capacity and functionalities and Si has been the primary material for such devices owing to its reliability and versatility [60].

Si power devices are approaching their limits in terms of material properties and capabilities and WBG devices are thus emerging as the novel components for power converters owing to their superior properties. The core objective of advancing information electronics is to fabricate smaller submicron device tips for faster large data capacity processing while power electronics fabrication focuses on larger device tips (in the mm^2 region) [60]. Information electronics uses the conventional semiconductors like Si and GaAs but the next generation of power electronics is looking towards WBG materials as the alternative as Si approaches its limitations [60]. These next generation power electronics devices are evolving in two directions towards higher voltage applications and higher energy savings [60]. The WBG materials of SiC and GaN are leading the research in these two directions with SiC IGBTs geared toward higher voltage applications while GaN HEMTs and SiC MOSFETs spearheading the charge towards lightweight energy saving direction [60].

The impressive mechanical, thermal, chemical and electronic properties of Diamond, SiC and GaN have the potential for fabricating high power high temperature power devices resistant to extreme voltage, temperature and radiation conditions [61] [62]. The physical properties of bandgap energy, dielectric field strength, thermal conductivity and charge carriers saturation velocity are comparably better for WBG materials than Si and thus they exhibit higher blocking voltages, operating temperatures, lower ON resistances and switching frequencies [2] [3] [63] [64] [65]. Figure 9 shows these properties graphically with the WBG properties demonstrating better numbers in each property [63].

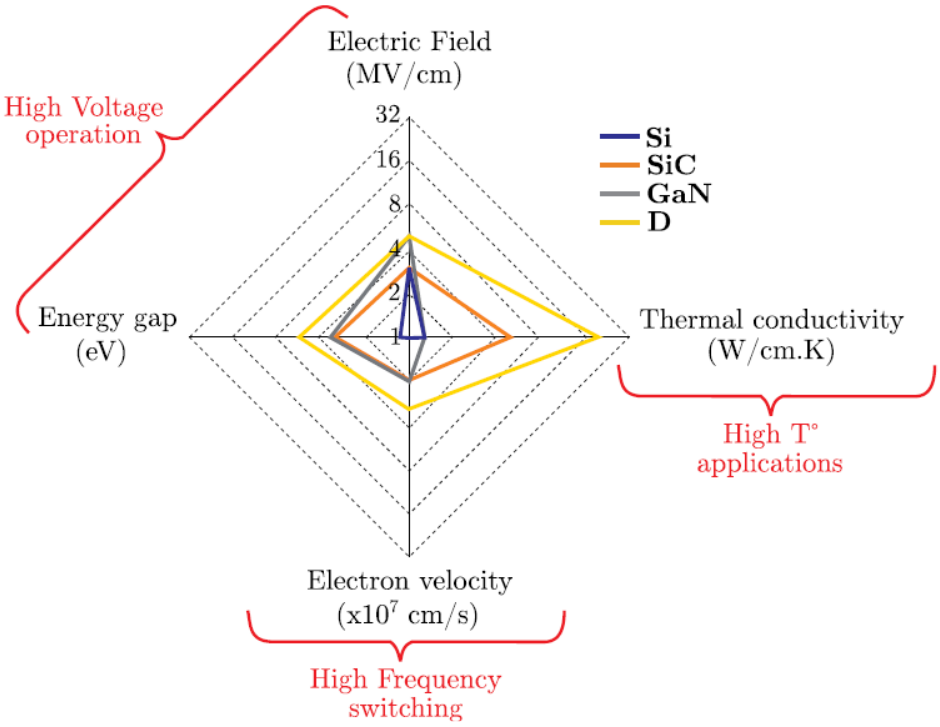

Figure 9. Material property comparisons between Si, SiC, GaN and Diamond.

Another property of WBG materials that makes them suitable for power devices is that their Coefficient of Thermal Expansion (CTE) values are close to ceramics used in power device packaging [65]. Having CTE values similar to the packaging ceramics material is more suitable for high power and high temperature applications as compared to Si [65]. A semiconductor material's ability to switch signals at high frequency is directly proportional to its drift velocity and since WBG materials have their drift velocities more than twice that of Si, they have the ability to have higher frequency switching capabilities [66]. This higher drift velocity also means that charges in the depletion region of diodes are removed faster and so the reverse recovery current and reverse recovery time of WBG materials are also smaller [66].

The lower junction temperatures that can be achieved in the power devices due to the better thermal properties of WBG materials also make them ideal for Hybrid Electric Vehicles (HEVs)/Electric Vehicles (EVs) where low power losses and lower cooling requirements are a premium [63]. Si diodes and IGBTs are currently the industry standard for HEV/EV power systems but WBG semiconductors like SiC, GaN, Gallium Oxide (Ga_2O_3) have the potential to replace the Si devices in EV applications [63].

Although figure 9 shows why Diamond is considered the ultimate semiconductor, difficulty in fabrication and costs have limited its utility in commercial power devices. The device packaging also affects how well the device can actually utilize the material properties to their fullest [63]. With the maturity in research and development of GaN and SiC fabrication technologies, these two materials have been very attractive to high power and High Temperature Electronics (HTE) manufacturers [2]. SiC has the best balance of commercial availability and material properties although GaN does have better frequency and high voltage performance [2].

Before moving on to each of the WBG materials individually, some of the drawbacks and challenges of these materials need to be mentioned. One drawback of WBG materials is that the electron and hole mobilities are not in the same order of magnitude and their ratios large enough to not be suitable for bipolar devices [65]. Although WBG switching devices are being commercially available and utilized in power supplies, smart grids and motor controls, the long-term reliability of the devices during extreme operating conditions needs to be studied and addressed since failures of power devices can lead to failure of entire systems [64] [67]. For instance, a majority of

WBG commercial power diodes are not avalanche rated and their Safe Operating Area (SOA) under high temperatures are rarely mentioned in their manufacturer's datasheet [64]. Some of the industry-best SiC power MOSFETs and GaN power transistors have been shown to suffer from high reverse leakage currents at high temperatures and their gate dielectrics also have reliability issues [64].

Developing low defect-density wafers with high current handling capability is a key challenge for GaN and SiC wafer manufacturers [64] [65]. The on the field reliability of the power devices in high-volume commercial applications needs to be demonstrated and documented [64]. Reliability of the devices in terms of switching performance at specific blocking voltages and high temperatures needs to be addressed by manufacturers [64]. Most importantly, the fabrication process needs to be optimized to reduce manufacturing costs while maintaining device reliability to make the devices commercially viable [64] [67].

The following discusses the more notable WBG materials used in industry today for power devices.

2.2.1 SiC

Although Si has been the top semiconductor material for high voltage applications, the advancements in SiC bulk material fabrication processes has made SiC the frontrunner in dethroning Si [2] [63]. Si power devices are approaching their physical limits of blocking voltages of 6.5 kV and maximum operating temperatures of 175 ˚C and improving the devices with these limitations is becoming more and more difficult [66]

[68]. SiC has higher breakdown field strength, higher switching frequency, higher thermal conductivity and higher carrier drift velocity as compared to Si and so can surpass the voltage and temperature limits of Si [2] [63] [68] [69]. The high thermal conductivity of SiC compared to Si and GaAs allows for devices to operate at higher current density while minimizing the cooling requirements [2]. Higher breakdown voltages mean the SiC MOSFETs can be made thinner with higher dopant concentrations, lower parasitic capacitances and faster switching speeds [63] [66]. The higher bandgap of SiC means that the level of thermally induced carriers that make Si almost metal-like at 200 ˚C does not occur in SiC until 1000 ˚C making it ideal for high temperature applications [70].

The bulk growth of SiC had been the biggest obstacle in limiting the usefulness of SiC in electronic applications back in the early 1990s caused due to higher density of micropipes in the crystal growth structure [5]. Micropipes are bulk defects that can start at the seed crystal and then propagate through subsequent epitaxially grown SiC layers and can cause the device to electrically and structurally fail [5]. However, the progress in SiC substrate manufacturing in the past two decades have drastically reduced the micropipe densities to almost nonexistence [2] [68] [70].

Although the cost of producing a SiC wafer can be up to 50 times that for a Si wafer, the material costs in a full system with a SiC chip is often lower than this cost of fabrication, packaging and overheads [70] [68]. The higher cost can also be justified by the higher payback from SiC devices in terms of reduction in cooling costs, system size and weight as well as increase in overall efficiency [70] [68].

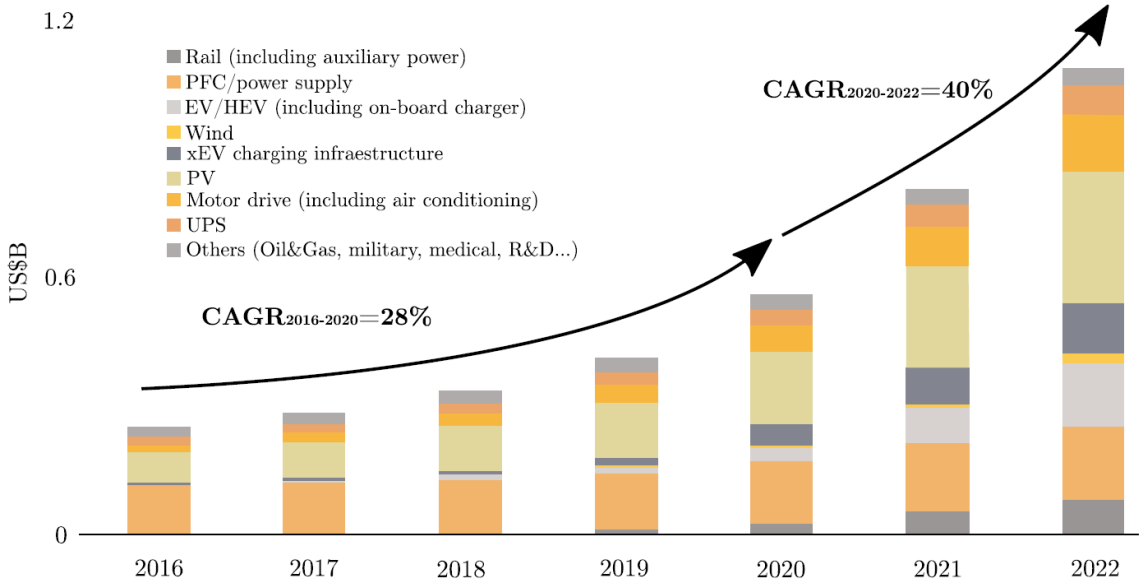

Figure 10. Current and future market of SiC devices.

The current and future applications market of SiC devices is shown in figure 10 with projections of over US$1 billion in 2022 and a growth rate increase of 12% [63]. SiC-MOSFETs are commercially available with low ON-state resistances and high blocking voltages making them suitable for applications such as EVs, PVs and motor drives [66] [63]. The two biggest competitors of SiC power devices in the 600 V range are the Si power MOSFETs and the Si IGBTs [2]. The ON-resistance of SiC MOSFETs is four times smaller than that of Si IGBTs and the resistances have been decreasing at the rate of 30% every three years [68]. Si IGBTs also have high dynamic losses at high switching frequencies [2]. SiC devices also require between 10 to 20 times less switching energy with 20 times higher switching frequencies as compared to Si devices [68]. SiC IGBTs are also commercially available these days and perform better as compared to their Si counterparts in high voltage, high switching speed applications [71]. SiC has also shown promising applications in MEMS devices like accelerometers that require accurate

and reliable functionalities at high temperatures as successfully demonstrated in the 500 ˚C to 900 ˚C range [72].

2.2.2 GaN

GaN has a wider bandgap and higher breakdown electric field as compared to both Si and SiC and so can go higher on the high voltage capabilities with its devices [70]. GaN has about three times the bandgap energy as compared to Si and about 1.1 times that of SiC with breakdown field strength 11 times that of Si and slightly smaller to that of SiC [73]. GaN however has a smaller value for thermal conductivity as compared to SiC. These properties as well as the high charge mobilities of GaN, just like SiC, allows for devices with thinner drift regions and consequently, lower specific ON-resistances [74]. Although the thermal conductivity of GaN is similar to Si and not as high as SiC, it does have a very stable Drain to Source ON Resistance ($R_{DS(ON)}$) with respect to temperature and makes it suitable for high power applications [75]. The lower $R_{DS(ON)}$ also means a smaller die size can be fabricated for a given current specification with lower capacitances [74] [76]. The lower capacitances allow for devices to operate at higher frequencies in high power density converters [76]. GaN HEMTs can switch up to 2 MHz as compared to about 500 kHz for SiC MOSFETs [76]. Typical SiC MOSFETs have electron mobilities of 28 $cm^2/(V.s)$ whereas the 2DEG formed in a GaN HEMT can have electron mobilities of up to 2000 $cm^2/(V.s)$ which again promotes for a smaller die size [70] [76].The material properties of GaN are more superior to SiC for high efficiency

and high frequency power converters even though SiC is more suitable for higher temperature applications [74] [76].

GaN wafers are mostly fabricated as an epitaxial layer on a holding wafer substrate, usually Sapphire, SiC or Si since high quality mono-crystalline GaN is not available yet [63] [70] [73]. GaN fabrication also suffers typical fabrication issues like packaging concerns, cheap fabrication processes etc. due to its relatively less mature history [73]. Sapphire was originally more widely used as the base substrate but Si is gaining ground due to the thermal insulating nature of Sapphire preventing Vertical device fabrication [70]. Although Si has poor thermal conductivity and has a high degree of lattice mismatch with GaN, GaN on Si is preferred due to the cheap availability of defect-free large diameter silicon wafers [76]. Although the lattice structure of SiC closely matches GaN, which reduces leakage and improves efficiency, GaN-on-SiC is limited to high performance RF devices due to the lack of availability of high quality large diameter SiC wafers [76].

Lateral devices like HFETs and HEMTs as opposed to vertical MOSFETs are the most widely produced GaN power devices with the lateral devices utilizing the band-bending effects of AlGaN on GaN that creates the 2DEG with high electron mobilities [70] [75]. Si GaN HEMTs are currently the most successful approach for fabricating switching devices rated up to 650 V for power electronics applications although GaN LDMOSFETs have also been reported with up to 2.5 kV blocking voltage [2] [70] [76]. However, the biggest problem with HEMTs is current collapse or dynamic on-resistance where the maximum drain current is decreased due to pulsed or high voltage operation of

the device [70]. Currently, HEMTs are the only commercially available GaN power devices, made up of AlGaN/GaN thin layers grown on Si wafers [63]. High voltage AlGaN/GaN HEMTs with over 1 kV blocking voltage was reported as early as 2006 and low $R_{DS(ON)}$ high voltage AlGaN/GaN HEMTs on semi insulating SiC were also reported in 2010 [2]. GaN HEMTs do have some drawbacks though like requiring a large lateral separation between gate and drain terminals to create large blocking voltages which increases the device surface area and hence, increasing the cost to current ratio [73]. Also, these HEMTs are typically Depletion mode which means they are normally ON and a negative gate bias is required to turn them OFF [73]. Enhancement mode HEMTs are available as well though.

GaN as a semiconductor material for LEDs started off in 1993 with GaN high brightness blue LEDs and has covered the visible and deep-UV range with GaN alloys with InN and AlN [67]. Figure 11 shows the current and future market prospects of GaN with its value projected to cross US$450 million in 2022 [63]. This market is estimated to cross the US$ 700 million by 2025 due to expansion to the automotive EV sector [63] [76]. The overall GaN market is also expected to exceed US$ 2 billion by 2024 with contributions from the defense and telecom sectors in RF and 5G [76]. Currently, GaN-on-SiC is predominantly used in 4G LTE cellular wireless infrastructure and is expected to do the same with the innovations of 5G [76]. GaN power technology also has a significant market share of fast chargers for smartphones with OEMs like Samsung, Xiaomi, Oppo etc. developing and launching newer and higher powered fast chargers [76].

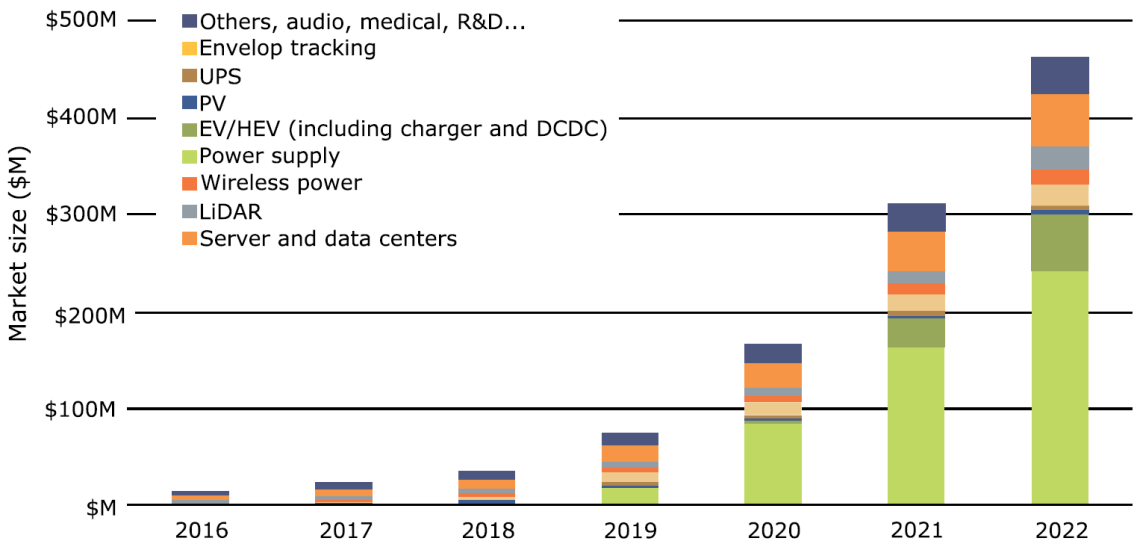

Figure 11. Current and future market prospects of GaN.

2.2.3 UWBG semiconductors and AlGaN

Ultrawide-bandgap (UWBG) semiconductors have bandgap energies larger than the 3.4 eV of GaN materials and include AlGaN, AlN, Ga_2O_3, diamond, and cubic BN [28]. The figures of merit of these devices made from these materials scale up non linearly and so have the potential to have much better performance than WBG devices [28]. The Baliga Figure of Merit (BFOM), which is a measure of the reduction of conduction losses in unipolar devices, is shown in figure 12 for different semiconductor devices in log-log scale [28]. The lower right corner shows UWBG materials which have lower specific on resistances and higher BFOM and hence better theoretical performance [28].

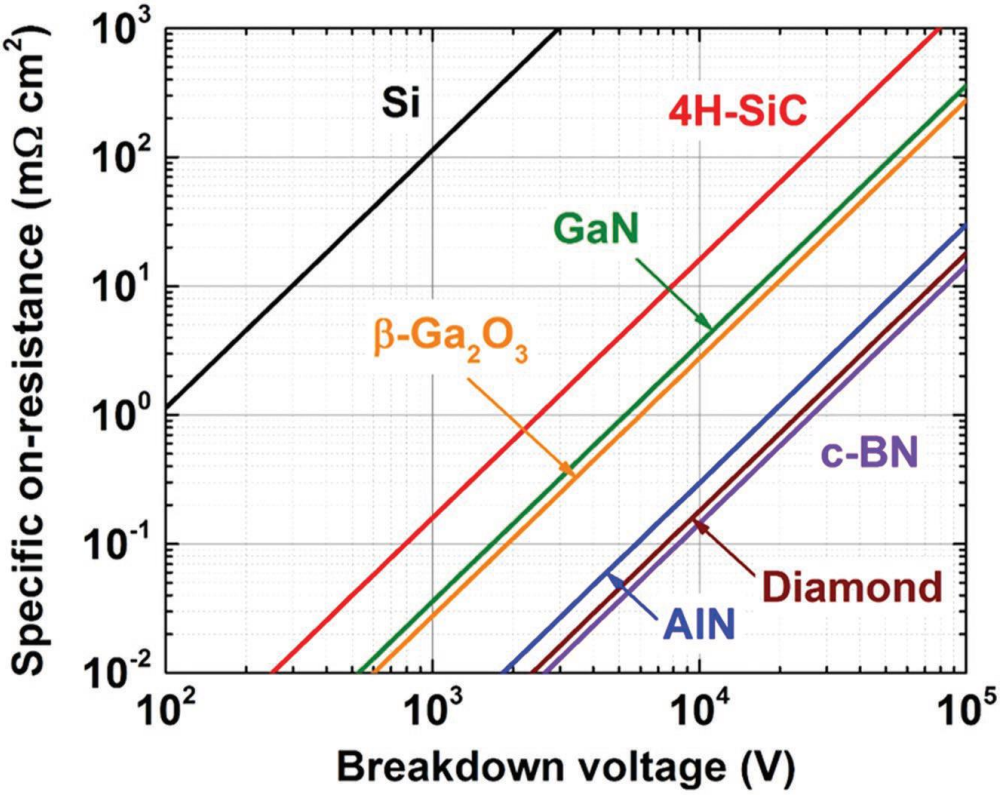

Figure 12. BFOM for different semiconductors.

AlN, GaN and Indium Nitride (InN) are called III-Nitrides and have exceptional material properties like their large bandgaps and stable Wurzite hexagonal crystal structures making them ideal for power and optical device applications [77]. These III-Nitrides have elements with large differences in electronegativity between the group III (Al = 1.18, Ga = 1.13) and group V (N = 3.0, In = 0.99) elements and produce very strong chemical bonds. Stronger chemical bonds result in physical properties like higher melting points and mechanical strengths which means possibility of applications in more rugged conditions [77]. The ability to create alloys within these III-Nitrides also provides a means to modulate material properties as required for the specific application like bandgap energy values ranging from 3.4 eV to 6 eV depending on the Al and Ga molar

contents in AlGaN [28]. The III-Nitrides are also direct bandgap which allows them to be used in optoelectronic applications covering the entire visible spectrum and the UV region [77]. They also have lower leakage and dark currents owing to their low intrinsic carrier concentrations which are exponentially decaying functions of bandgap energies [77].

AlGaN is an alloy of AlN and GaN with its material properties dependent on the molar fraction of Al and Ga content and is expressed as $Al_xGa_{1-x}N$ where x ($0 \leq x \leq 1$) represents the molar fraction of the group III element in the alloy. This means a wide range of bandgap energies, electric breakdown fields >10 MV/cm, high electron mobilities up to 1000 $cm^2/(V.s)$ and saturation velocities $>10^7$ cm/s [28]. The electron affinity of AlGaN is found to decrease with increase in the AlN content which can be used to modulate the band bending of the 2DEG channels in HEMTs as per requirement [78]. The thermal conductivity of AlGaN is also found to be exceptionally high and in between the values for AlN and GaN with potential for high performance thermal management applications, although it is counterintuitive to the notion that alloying usually lead to the lowering of thermal conductivities [79]. AlGaN also shares the same crystal structure as the more matured semiconductor device material of InGaN which allows it to take advantage of the already existing manufacturing technologies of InGaN [28].

As mentioned earlier, AlGaN/GaN HEMTs use the creation of 2DEGs in the heterostructure and are the only commercially available power AlGaN devices mostly suitable for high power, high temperature and high frequency switching applications [80].

The content of Al and Ga determines the transport properties of the 2DEG channel and the addition of a thin AlN layer between the GaN and AlGaN creates a double heterostructure which increases the electron mobility and reduces $R_{DS(ON)}$ as well [81]. High Al content AlGaN/GaN HEMTs have their barrier layer more insulator-like which allows for higher operating temperatures [57].

However, there are some issues facing AlGaN power devices that hinder their reliability and performance. Higher bandgap energy increases dopant ionization energies which decreases free carriers and reduces mobilities [28]. AlGaN layers on GaN substrates have tensile stress which are susceptible to cracks that might cause heterostructure failure [28]. Self-heating within the epitaxial structure of the HEMTs is another issue which restricts the power limits in high voltage applications due to lack of thermal dissipation [82] [55] [56]. This self-heating issue can cause abrupt increase in temperatures, decrease in drain currents, current collapse and thermal breakdown of the device at lower operating voltages [83]. The availability of single-crystal substrates and the nascence of scientific understanding of the heteroepitaxial fabrication is another challenge for AlGaN/GaN HEMTs production [28]. Despite these difficulties, AlGaN/GaN HEMTs have found applications in high power RF radar applications like air traffic control and surveillance [84] [85]. AlGaN has a tunable bandgap energy depending on the Al and Ga content and allow for fabrication of AlGaN optical devices with wavelengths ranging from 200 nm and 365 nm that can have applications include in UV curing and printing, phototherapy and medical applications [86]. AlGaN and III Nitrides have also found application in waste heat recovery through thermoelectric

devices capable of converting heat into electricity [87]. The direct bandgap material properties of AlGaN also allows the integration of Surface Acoustic Wave (SAW) devices with optoelectronic devices [88].

2.3 Transformerless Inverter Topologies

Renewable energy sources, most notably PV power, are considered to be clean and unlimited and hence essential in fulfilling to current and future energy requirements [89] [90] [91] [92]. PV system are continually becoming cheaper and more efficient with advancements in PV research and it has grown rapidly from 200 MW in 2006 to 300 GW in 2016 [89] [90] [91]. The biggest advantages of PV systems are their long lifetime, low maintenance, zero fuel requirement and easy installation in remote areas [91]. Although standalone PV systems are preferable due to ease of not requiring a grid, such systems are more costly to install. Due to higher efficiencies and reliability and lower weight and costs, most PV systems are grid connected [89] [90]. To better utilize the PV power, grid interconnection of PV system is needed. Grid-connected PV systems require power devices like inverters to connect the PV panel to the grid and such inverters are separated into either galvanic isolated or non-galvanic isolated inverters [89]. The galvanic isolated inverters have a high frequency DC side transformer or a low frequency AC side transformer for safety and efficiency purposes [89]. Inverters with high frequency transformers aren’t always bigger and heavier than those with low frequency transformers or those without transformers altogether [90]. However, non-galvanic

isolated inverters do not have these transformers and are usually lighter and smaller with higher efficiencies [89].

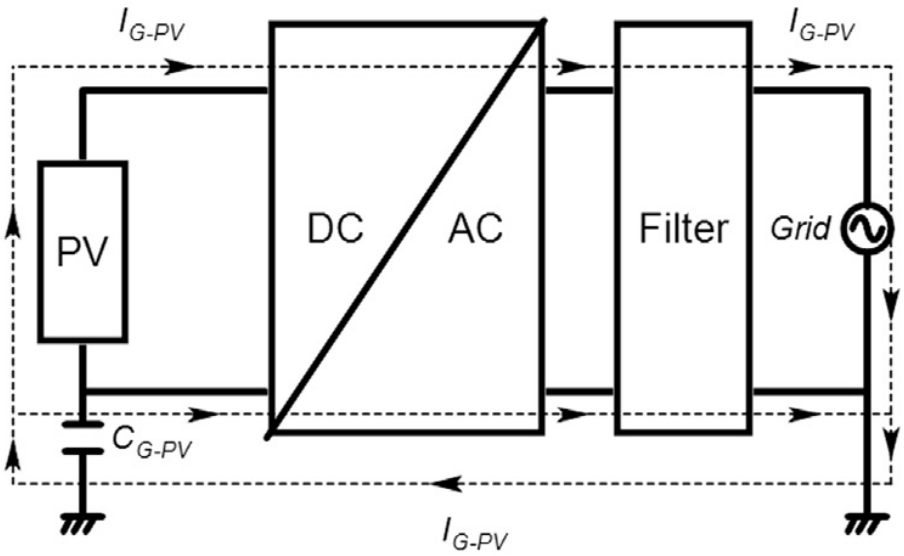

Figure 13. Generic tranformerless PV inverter.

Figure 13 shows a general schematic of a transformerless PV inverter with a filter and it shows that a large stray parasitic capacitance (C_{PV}) between the PV panel and the grid can cause a direct ground-current path to be formed [89] [91] [93]. C_{PV} is formed due to electrically chargeable surfaces on the PV module and the value of this C_{PV} depends upon factors like solar panel and frame structure and surface area, weather and operating conditions like humidity and dust particles on the PV panels and is very unpredictable [93]. The common voltage (C_{MV}) can cause resonance on the circuit formed by the filter inductor and C_{PV} which can produce a large Common Mode ground Current (I_{CM}) [89] [93]. This I_{CM} can create harmonic frequencies to be injected into the grid current which can increase system losses and produce unnecessary Electromagnetic Interference (EMI) and safety issues [89]. Although transformerless inverters have an

issue of leakage currents, this issue has been solvable through various techniques to varying degrees and so such inverters are gaining market popularity [89] [90] [91] [92]. Many decoupling techniques have been implemented in different inverter topologies to reduce I_{CM} like decoupling the DC and AC sides, clamping the CMV during the freewheeling period, modifying the switching sequences in the topologies, grounding the PV frame to reduce C_{PV} etc. [89] [90] [91] [92] [93]. Several techniques to reduce the common mode current have been proposed in literatures with varying improvements in efficiencies [94] [95] [96].

Grid connected PV systems need to fulfil certain parameters to maintain a particular performance level such as minimum allowable Total Harmonic Distortion (THD), Grid frequency range, acceptable power factor and I_{CM} ranges, harmonics in the current injected into grid, DC current injection into the grid to avoid transformers saturation etc. [89] [90]. There are several standards set by different organizations like Institute of Electrical and Electronics Engineers (IEEE), International Electro technical Commission (IEC), National Electrical Code (NEC) in order to regulate and quantify these requirements with the most popular standards being IEC 61727, IEEE 1547–2003, IEEE 929–2000 etc. [90].

There are different ways to categorize PV inverters like on the basis of the number of power processing stages and power switching devices, location of power decoupling capacitor, presence of transformers, connection to grids etc. [90]. Grid connected PV inverters can be categorized as Central, String, Multistring and AC module inverters in terms of methods of connecting multiple PV modules [89] [90] [91] [92]

[97]. Central inverters integrate several PV modules separated into series connections each of while produce voltages high enough to not require further amplification [91]. String inverters are smaller versions of central inverters with a single PV module and Multistring inverters are string inverters equipped with Maximum Power Point Tracking (MPPT) systems and DC/DC converters [91]. AC module inverters have the PV module and inverter integrated into a single design [91].

Based on the leakage current characteristics and the methods of decoupling, non-isolated single phase transformerless grid-tied PV inverter topologies can be categorized as zero-state decoupled, zero-state mid-point clamped and solidity clamped topologies [90] [92]. Zero-state decoupled topologies can decouple the PV module from the grid during the freewheeling mode when the DC source is not exciting the inverter [92] [93]. Zero-state mid-point clamped topologies decouple the PV module during the freewheeling mode and also clamp the short circuited output voltage to the mid-point of the DC-link [93]. Solidity clamped topologies have a solid connection between the PV module and the grid during the freewheeling mode [93] [98]. Figure 14 shows different single phase transformerless topologies categorized according to this decoupling basis with H5 and H6 MOSFET topologies falling under the Zero-state decoupled while the H6 falling under the Zero-state mid-point clamped categories [98].

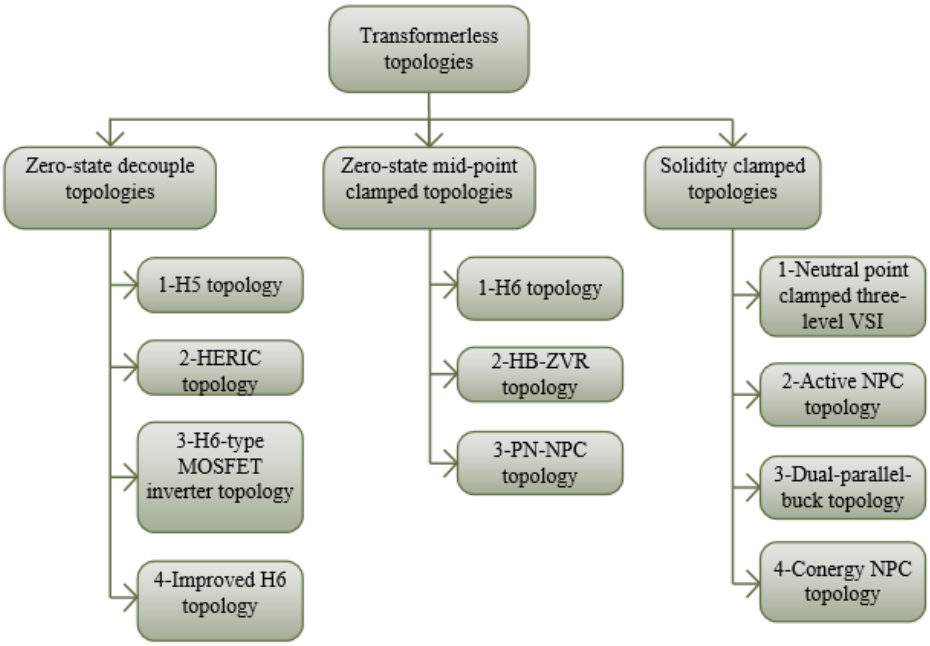

Figure 14. Transformerless single phase inverters categorized by decoupling methods.

This research compares the H5 topology and H6 topology with the proposed H5 topology in the next chapter. The following describes the H4 or Full-Bridge, H5 and H6 topologies in brief.

2.3.1 Full-Bridge topology

Figure 15 shows the Full-Bridge topology and its unipolar switching sequence for a single phase transformerless inverter [89] [99] [100] [101]. In the unipolar modulation scheme, for the positive half cycle, Q2 and Q3 are turned OFF, Q1 stays ON continuously while Q4 turns ON based on the reference and carrier signal comparisons to make the output voltage equal to the input voltage at the times Q1 and Q4 are on. For the freewheeling period when Q1 is ON and Q4 is OFF, the output current flows through Q1 and the antiparallel diode of Q2. For this schematic, the pairs of Q1 with Q4 and Q2 with

Q3 are complimentary and the opposite occurs for the negative half cycle. In this case, Q1 and Q4 are OFF, Q2 stays ON constantly while Q3 is modulated and the antiparallel diode of Q1 conducts during freewheeling. This topology has low CM current, constant CM voltage but the leakage current is high [89].

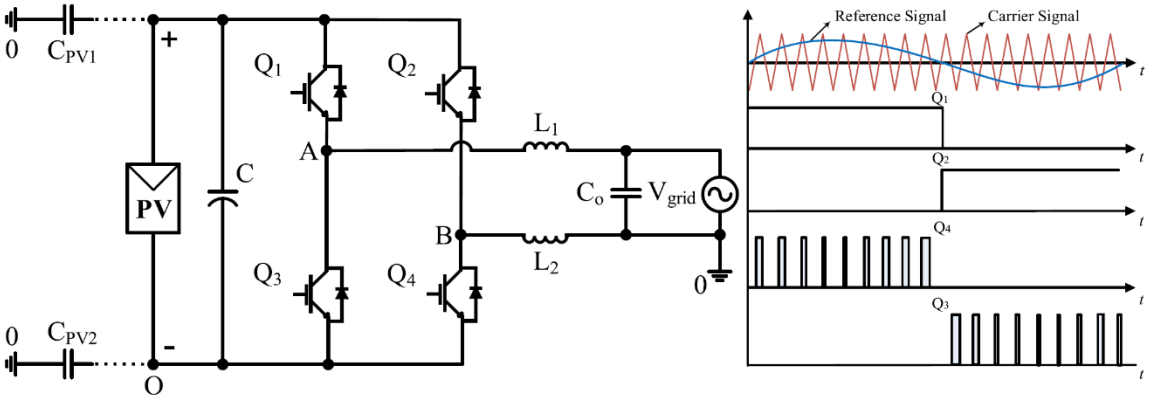

Figure 15. Full Bridge inverter with unipolar switching.

2.3.2 H5 Topology

Figure 16 shows the H5 topology and its switching sequence [89] [99] [100] [101]. Its operation is almost the same as the Full-Bridge topology but has higher efficiencies than the Full-Bridge. The main difference between the two is that a DC decoupling switch (Q5) is used on the DC side and is modulated at the switching frequency (f_{sw}) based on the comparisons between the reference and carrier signals [89]. Q3 and Q4 are also modulated at f_{sw} while Q1 and Q2 are switched at the grid frequency (f_G). The inverter goes into freewheeling mode every time Q5 turns OFF during either the positive or negative half cycles which prevents output current from flowing into the DC side and thus reduces I_{CM}.

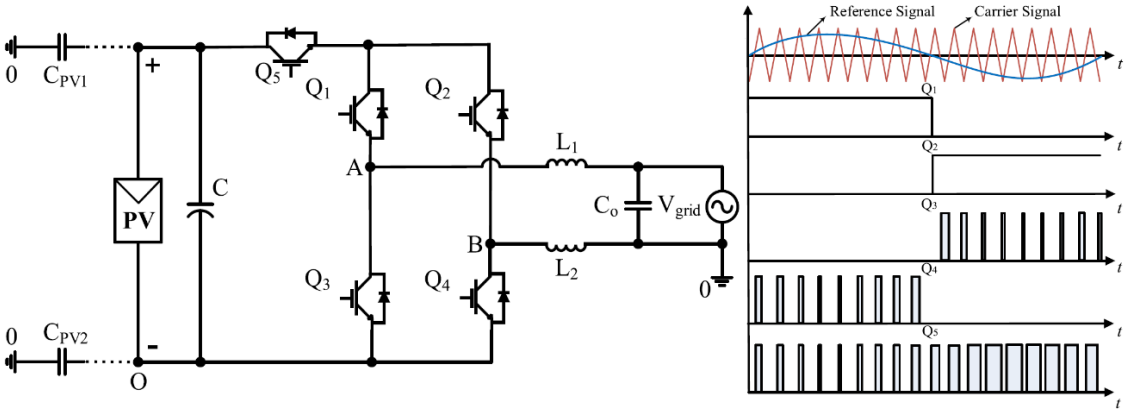

Figure 16. H5 inverter with its switching sequence.

During the positive half cycle, Q1 stays ON continuously at the f_G while Q4 and Q5 switch at the f_{SW} while the other switches are turned OFF. The freewheeling period when Q5 is OFF for this positive half cycle has current flowing through Q1 and the body diode of Q2. For the negative half cycle, Q2, Q4 and Q5 conduct during the active period while Q2 and the body diode of Q1 conduct during the freewheeling period. The main disadvantage of this topology is that there are more conduction losses during the active period with the addition of an extra switch.

2.3.3 H6 Topology

Figure 17 shows one design of an H6 topology with two diodes and its switching sequence [89] [99] [100] [101]. Its operation is similar to the H5 topology but has one more switch and two extra conducting diodes. In this topology, Q5 and Q6 switch at the f_G while Q1, Q2, Q3 and Q4 are modulated at the f_{SW}. As seen in figure 17, in the positive half cycle, Q6 is ON continuously while Q1 and Q4 are modulated at f_{SW} with

the rest of the switches turned OFF in the active period. During the freewheeling period of this cycle, only Q6 is ON and so the current flows through Q6 and the diode D2.

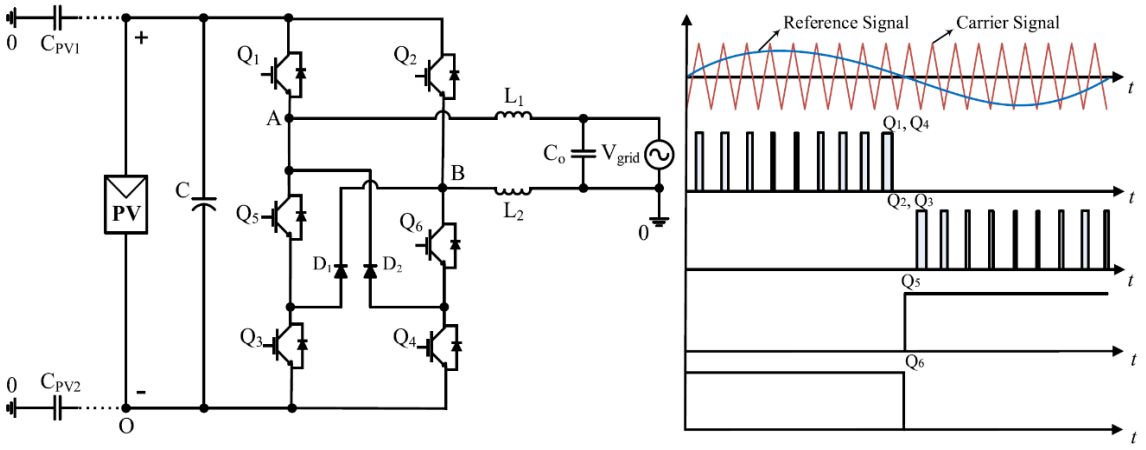

Figure 17. H6 inverter with its switching sequence.

In the negative half cycle, all switches except for Q2, Q5 and Q3 are turned ON for the active period at their respective switching frequencies as mentioned above. The freewheeling period of this cycle has only Q5 and the diode D5 conducting with the rest of the switches turned OFF. The I_{CM} is low for this topology as well but just like the H5, it suffers from higher conduction losses in the active period [89].

2.4 Digital Prototyping

2.4.1 FEA and COMSOL

Accurate digital prototyping software like COMSOL Multiphysics, ANSYS, Matlab etc. simplifies the product design process by reducing the number of actual physical iterations and saving time and cost of such builds. COMSOL is an FEA/Finite Element Method (FEM) software used for solving complex engineering numerical problems [102]. FEA is a computational technique used to find approximate solutions to

boundary value differential equations in physical structures [103] [104] [105]. Boundary value problems have dependent variable that need to satisfy specific differential equation conditions at specific regions or domains and specific values at the edge or boundary of these domains. FEM breaks down the large domains into smaller sub domains called Finite Elements to numerically approximate the solutions to the differential equations instead of analytically solving the equations at once. FEM is useful in solving problems with complex geometries and a multitude of dependent and independent variables where analytical methods are difficult to apply. FEM can be used to solve multi-physics integrated problems but the main disadvantages are that the solutions are approximate and are only as accurate as the ability of the user and the degree of precision with which the problem is defined [103] [104] [105].

FEA was first introduced in 1956 by M. J. Turner and it gained popularity in the aeronautics industry to solve complex structural analysis problems of aircrafts and missiles [103] [104]. Today, FEA has found applications in several scientific and engineering fields to solve problems in electromagnetics, heat transfer, acoustics, fluid mechanics etc. [103] [104] [105].

FEA divides the geometry into finite elements in a process called Meshing and the more smaller the elements, the finer the mesh and greater the chance of having the approximations converge to a consistent solutions. Although finer meshes don’t always guarantee convergent solutions while increasing usage of resources and computational time. The balance between meshing refinement and solution accuracy depends on the user’s knowledge and ability to use the FEA software [103] [104] [105].

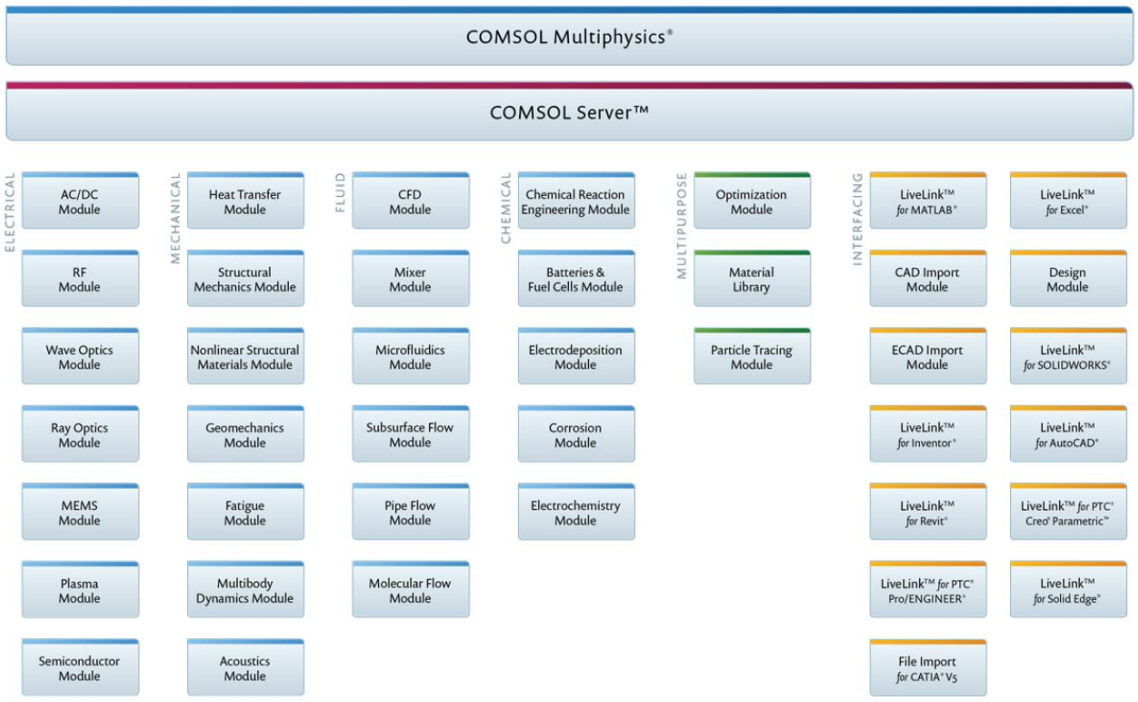

Figure 18. COMSOL Multiphysics features.

In general, all FEA software environment consists of three steps to solve for boundary value problems. The first step is called the Preprocessing step where the problem is defined in terms of geometry of the structure, the physics involved, the dependent and independent variables, material properties, meshing, initial and boundary values and the solver methods [103] [104] [105]. The Solution step involves the software solving for the dependent variables using the definitions made in the Preprocessing step [103] [104] [105]. The third step is the Post-Processing step where the solutions can be interpreted and analyzed in terms of graphs, tables, images etc. and the complexity of this step depends on the features available in the software [103] [104] [105].

COMSOL Multiphysics is an FEM software capable of simulating and solving for a variety of physics problems. Some of the physics available on COMSOL are shown in

figure 18 [6]. COMSOL is a multiplatform software package and has features to interface with multiple software like Matlab, Solidworks, Java, Microsoft Excel etc. It can solve for Steady state and time dependent transient problems as well as those with parametric sweeps with a multitude of built-in visualization tools for postprocessing of the results [102] [106].

The use of COMSOL to simulate WBG power devices to analyze their structures and performance has been reported in literature. Manandhar et al. demonstrated the thermal cooling requirements and electrical performance of different WBG materials in MOSFET and HEMT structures in [17] [26] [27] [106] [107]. Akbari et al. demonstrated the non-uniformity of heating inside SiC MOSFET structures in COMSOL that can be useful in predicting the life expectancy of the devices [108]. Naghibi et al. simulated MOSFET modules in 3D to monitor the temperatures of SiC MOSFET modules in [109]. Bagnall and Li et al. separately investigated the thermal heating effects of GaN HEMT devices in [110] and [111]. Temperatures and electric performance of AlGaN/GaN HEMTs have also been reported in literature [112] and [113].

2.4.2 PSIM

PSIM is an electronic circuit simulation software specifically designed for power electronics and motor drives [114]. PSIM provides a fast and powerful simulation environment for power electronics, analog and digital control, magnetics, motor drives, and dynamic system studies [114]. The PSIM environment has a circuit schematic section for designing the circuits, the simulation engine to calculate the simulation parameters

and the waveform processing program SIMVIEW to display the waveforms of the simulation [114]. PSIM has multiple add-on modules like the SimCoupler to run co-simulations with Matlab/Simulink, the Thermal Module to compute power losses of semiconductor devices within the circuits, the Renewable Energy Module to simulate solar and wind turbine models etc. PSIM has a built-in database of semiconductor devices from various vendors and has options to add custom devices as well. PSIM has been reported in literature in simulating different transformerless topologies using WBG materials as seen with single phase modified H5 inverters with SiC and GaN switches in [26] and [27], a full bridge GaN FET inverter in [115], three phase inverter comparisons with SiC MOSFETs and Si IGBTs in [116], the use of GaN transistors in T-type inverters for wireless inductive charging in [117] etc.

3. Methods

3.1 Model Definition in COMSOL for VDMOSFETs for different Semiconductor materials

2D [16] and 3D [17] stationary models were created in COMSOL to simulate the steady state effects of Joule Heating for each of the materials of SiC, GaN and AlGaN as VDMOSFET semiconductors in comparison to Si. The Semiconductor Physics and the Heat Transfer in Solids Physics modules were used to model the two parts of the physics involved [16] [17]. The two physics used solved for the electric potential, the electron and hole concentrations and the temperatures within the structure of the VDMOSFETs [16] [17]. The semiconductor physics module were run first to calculate the heat generated due to Joule heating while the initial temperature of the VDMOSFETs were set to room temperature i.e. 20 ˚C. The Semiconductor module solves for the electric potential in the MOSFET structure and the total heat generated within the device [16] [17]. The Heat Transfer in Solids module solves for the temperature induced by the heat generated [16] [17]. The geometric structure of the devices remained the same for all the materials that were modeled with only the material properties being different for each material [16] [17].

3.1.1 Model Geometry and Boundary Conditions

The 2D cross section of a VDMOSFET device is shown in figure 4 [14]. Unlike the LDMOSFET, the VDMOSFET structure has the highly doped drain region vertically below the lightly doped n-drift region [16]. The source terminals are on either side of the gate terminal [16]. A highly doped n+ region is embedded in a p base region above the n-drift region. The application of a positive gate to source voltage (VGS) creates a channel from the heavily doped n+ region to the drift n- drift region through the p base [16].

Only half of the structure for 2D and a quarter of the structure for 3D were modeled owing to the symmetry of the device as shown in figures 19 and 20. Figure 19 also shows the dimensions and the log of the dopant concentrations within the device in 2D and figure 21 shows the same for the 3D models [16] [17]. The basic structure of a VDMOSFET consists of the source and gate terminals on the top and drain terminal at the bottom of the VDMOSFET as shown earlier in figure 4 with the source terminals lying on either side of the gate terminal. The gate metal contact is insulated from the semiconductor material by a thin oxide layer [17]. A heavily doped n+ region sits on top of the drain contact [17]. The source contact is placed on top of a heavily doped p+ region with a heavily doped n+ region nestled within it [17]. When a drain to source voltage (V_{DS}) is applied, the direct flow of electrons from the source to the drain through the n-drift region is prevented by this heavily doped p-region [17]. The application of a gate to source voltage (V_{GS}) creates a channel within this p+ region so that current can flow from the source to the drain [17]. The dimensions of the VDMOSFET structure and dopant concentrations were obtained from [15]. The y-axis (left hand vertical edge) in

figure 19 shows the axis of symmetry for the 2D VDMOSFET models while the xz-plane (front) and the yz-plane (left) in figure 20 show the two planes of symmetry for the 3D models.

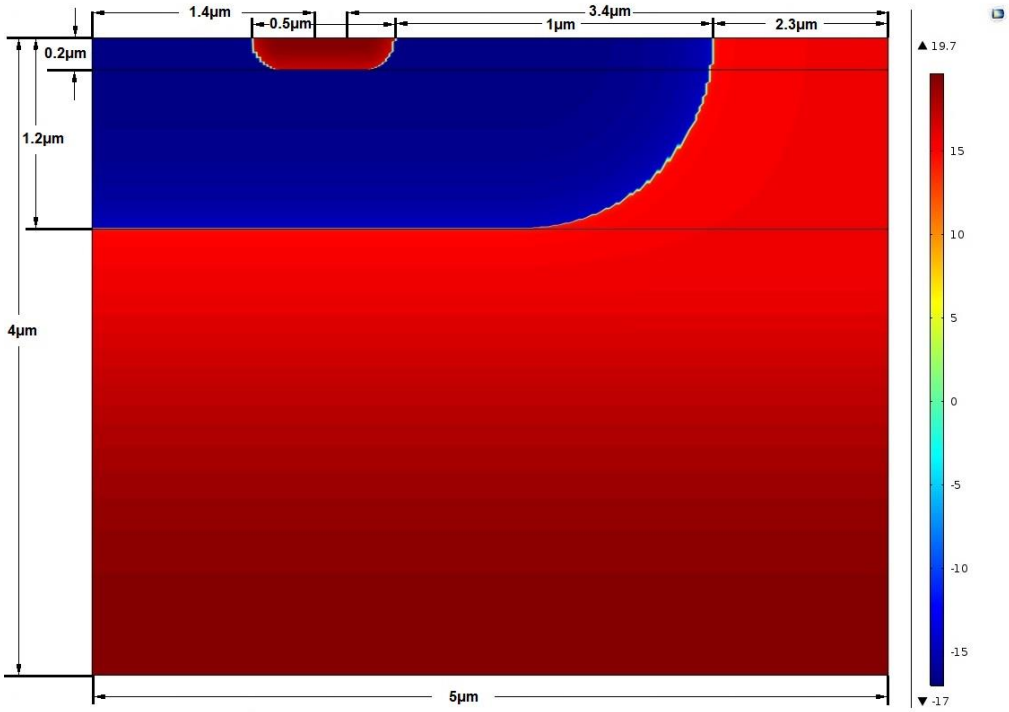

Figure 19. Half cross section of the VDMOSFET structure with log of dopant concentrations of the 2D models.

COMSOL solves for approximate solutions of dependent variables where those variables satisfy specific differential equations under the domain of known independent variables [118]. The values of the dependent variables at the edges of the known independent variable domains are set as the Boundary Values [118]. The boundary values for the models were set separately for each of the two Heat Transfer in Solids and Semiconductor physics modules.

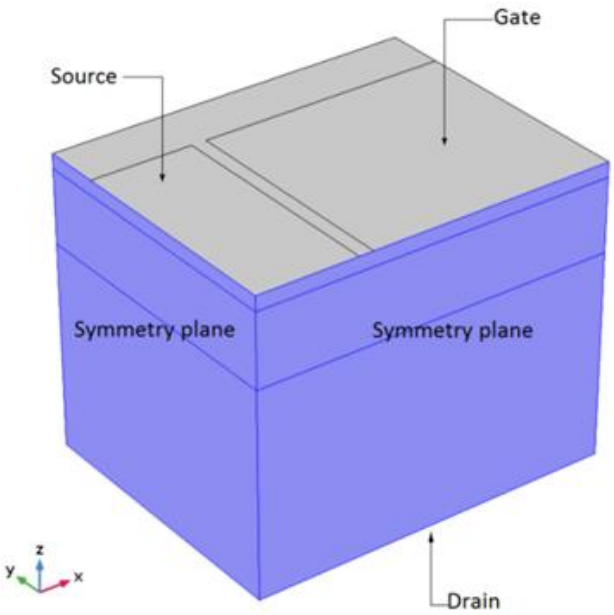

Figure 20. 3D model of a quarter section of the VDMOSFET structure.

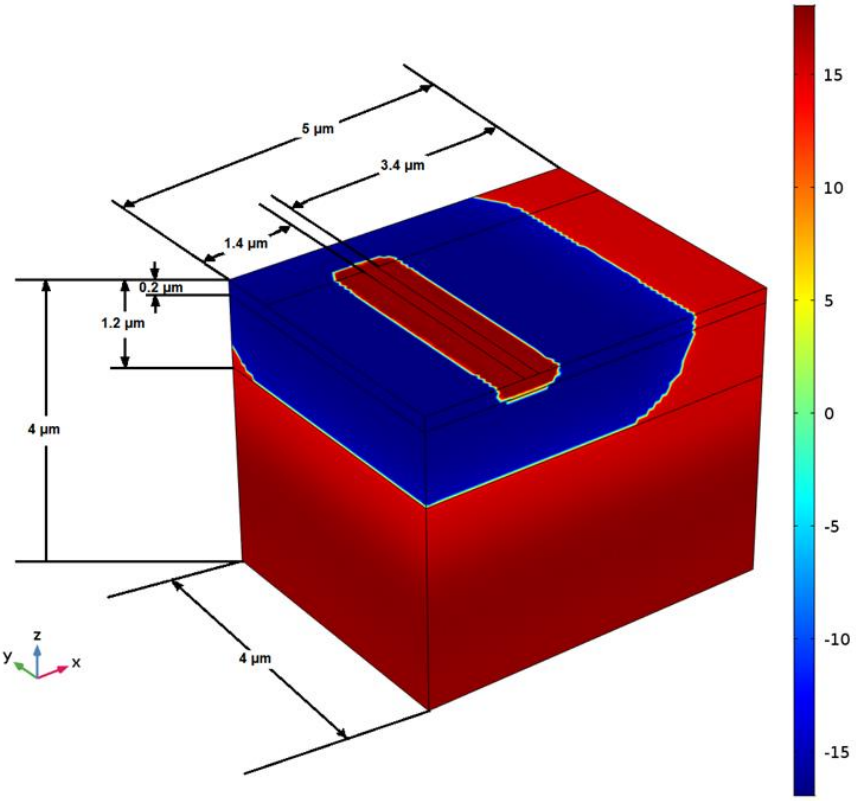

Figure 21. Quarter cross section of VDMOSFET structure with log of dopant concentrations.

Axial symmetry was set on the respective axes and planes as mentioned earlier for both semiconductor and heat transfer modules. The Source and Drain terminals were set as Metal Contact boundary conditions while the Gate terminal was set as a Thin Insulator Gate boundary condition with an insulator thickness of 0.1 μm in the semiconductor module [16]. These three terminals were set with Convective Heat Flux boundary conditions to account for convective heat losses from the terminal contacts to simulate dissipation of heat loss to the ambient air at room temperature without any forced air cooling [16]. The two inner boundaries between the top and bottom surfaces were set to Continuity boundary conditions to represent thermal and electrical continuity within the MOSFET semiconductor heterostructure. The remaining boundaries were set as thermal and electrical insulator boundaries [16].

3.1.2. Material Properties

All semiconductors were assumed to be isotropic with all material properties remaining uniform in all spatial directions as setup in COMSOL. Material properties for Si, GaN and $Al_{0.15}Ga_{0.85}N$ were used from predefined material libraries in COMSOL while the properties for SiC were obtained from [119] and [120]. Table 1 shows the material properties for the semiconductor materials. The thermal conductivity for AlGaN was obtained from [82].

Table 1. Semiconductor material properties.

Property	Name	Unit	Si	GaN	SiC	$Al_{0.15}Ga_{0.85}N$
Relative Permittivity	ε_r	1	11.7	8.9	9.7	9.7
Thermal Conductivity	k	W/(m.K)	131	130	490	50
Density	ρ	kg/m^3	2329	6070	3216	6070
Heat Capacity at constant pressure	C_p	J/(kg.˚C)	700	490	690	490
Band gap	E_{g0}	V	1.12	3.39	3.26	3.7
Electron Affinity	χ_0	V	4.05	4.1	3.1	4.1
Effective Density of states, valence band	N_v	cm^{-3}	$T^{3/2}\times 2.0\times 10^{15}$	$T^{3/2}\times 8.9\times 10^{15}$	$T^{3/2}\times 4.8\times 10^{15}$	$T^{3/2}\times 8\times 10^{15}$
Effective Density of states, conduction band	N_c	cm^{-3}	$T^{3/2}\times 5.3\times 10^{15}$	$T^{3/2}\times 4.3\times 10^{14}$	$T^{3/2}\times 3.25\times 10^{15}$	$T^{3/2}\times 2.3\times 10^{14}$
Electron Mobility	μ_n	$cm^2/(V.s)$	1450	1000	900	1000
Hole Mobility	μ_p	$cm^2/(V.s)$	500	200	100	350

3.1.3 Semiconductor Physics modeling

The semiconductor physics module of COMSOL uses partial differential equations with the conventional drift-diffusion approach to solve for the dependent variables [17] [118]. The module solves Poisson's equation and current continuity equations to obtain solutions for the dependent variables of electric potential and electron and hole concentrations respectively [17] [118]. Poisson's equation is expressed as:

$$\nabla \cdot (\varepsilon \nabla V) = -q(p - n + N_D^+ - N_A^-) \quad (1)$$

Where ε is the permittivity of the material, V is the electric potential, q is the elementary charge, p and n are the hole and electron concentrations respectively and N_D^+ and N_A^- are ionized donor and acceptor concentrations respectively [16] [118].

The current continuity equations are given as:

$$\begin{aligned} \nabla \cdot \boldsymbol{J}_n &= -qU_n \\ \nabla \cdot \boldsymbol{J}_p &= -qU_p \end{aligned} \tag{2}$$

Where J_n and J_p are the electron and hole current densities respectively obtained from the drift-diffusion equations and U_n and U_p are the net electron and hole recombination rates respectively for all generation and recombination mechanisms [16] [118].

In order to simplify the process of solving these equations, COMSOL assumes the simplified relaxation-time approximation to describe scattering processes and does not consider the effects of magnetic fields, any time dependent conductivity phenomenon or the complex nature of the energy bands and instead assumes them to be parabolic [17] [118]. The simulations performed use Fermi-Dirac statistics to solve for the probability of carriers energies instead of Maxwell-Boltzmann distribution due to the heavy doping levels involved in the semiconductor materials [17] [118].

COMSOL relies on dividing the material domains into smaller components using different meshing techniques to solve for the differential equations involved. It offers two options of finite element or finite volume formulations for this discretization of the domain structures - Finite Element Discretization and Finite Volume Discretization [17]. Finite volume discretization conserves current while finite element discretization

conserves energy [17] [118]. Finite element discretization is faster but finite volume discretization provides more accurate results for the current density of charge carriers and so, finite volume discretization was used for the 3D models [17] [118].

The doping profiles of the device as shown in figures 19 and 21 were obtained by following the typical doping regions for VDMOSFETs as seen in figure 4 [17]. User defined analytical box doping models were used to create the doping profiles [17]. Gaussian decay profiles were used to simulate the variation in dopant concentrations within the structure when going away from the external surfaces of the semiconductor substrate [17]. The heavy n+ doped region and heavy p+ doped region had maximum dopant concentration values of 5×10^{19} cm^{-3} and 1×10^{17} cm^{-3} respectively while the n-drift region had a maximum dopant concentration value of 5×10^{15} cm^{-3} [17]. These dopant concentrations were obtained from literature [15] and the initial models for Si, SiC, GaN and AlGaN used these values. A separate set of models were simulated with lower dopant concentrations of heavy n+ region at 5×10^{17} cm^{-3}, n-drift region at 5×10^{14} cm^{-3} and heavy p+ doped region at 1×10^{15} cm^{-3} to simulate electrical breakdown of the device. These same concentration values were then applied to Si, GaN and AlGaN VDMOSFET structures of the same dimensions to make like for like comparisons. The trapping and release of carriers in the defects within the semiconductor material is called the generation and recombination process and it generates heat in the material [17] [118]. This recombination process was simulated using the Shockley-Reed-Hall model [17] [118].

3.1.4 Heat Transfer in Solid modeling

The reference temperature for the semiconductor module was set to 293.15 K or 20 ˚C to calculate the heat generated due to Joule heating and generation-recombination processes [16] [118]. The Heat Transfer in Solids module then calculated the temperature of the device using the heat generated as its heat source.

In order to model heat loss from the terminal contacts of the MOSFET, and effective thermal resistance (R) of 100 K/W was chosen, which is a number generally used for Si transistors [16] [118]. This thermal resistance value was used to calculate the effective heat transfer coefficient, h_0 of the contact boundaries given by [118]:

$$h_0 = \frac{1}{R.A} \tag{3}$$

Where A is the total area of the terminal contacts. A convective heat flux boundary condition was set on the terminal contact boundaries to account for this heat loss [16] [118].

To verify the effects of the radiation emitted by the VDMOSFET structures on their temperatures, additional studies were added to the studies of the Si and GaN models under normal operating conditions. This was done by adding a boundary heat flux condition of Surface to Ambient Radiation on the top and right surfaces of the VDMOSFETs structures. The bottom surface was considered to be on a substrate and not radiating while the left surface was not applicable to be a radiating surface as it is an axis of symmetry. The net inward heat flux, $\boldsymbol{q}$, from surface-to-ambient radiation is given by

$$-\boldsymbol{n}.\boldsymbol{q} = \varepsilon\sigma(T_{amb}^4 - T^4) \quad (4)$$

where ε is the surface emissivity, σ is the Stefan-Boltzmann constant (a predefined physical constant), T is the structure's temperature, T_{amb} is the ambient temperature. The ambient temperature was set to room temperature of 20 ˚C. The values of emissivity for Si and GaN were assumed to be constant for all wavelengths and temperatures for simplicity. The emissivity for Si was set to 0.67 as reported in [121] and that for GaN was set to 0.89 as reported in [122]. Surface to ambient radiation was not simulated for any other material model, under normal or breakdown conditions, as the effects of radiation were found to be negligible as shown in the results section.

3.2 PSIM simulation of modified H5 Inverter with Si and GaN devices

A single-phase inverter topology derived from the H5 topology was used to compare the performance of power switching devices made using Si, GaN and AlGaN/GaN as their semiconductors. These devices were used in PSIM to simulate their power losses at different operating conditions to compare their performance.

3.2.1 Modified H5 Inverter topology

Figure 22 shows a single-phase PV tied H5 Inverter topology while Figure 23 shows the proposed Inverter topology derived from this H5 topology by disconnecting S5 from S1 and connecting it to terminal A such that during the positive half cycle, current flows through switches S4 and S5 [27]. An extra switch, S6, is added between the DC link and terminal B which forms a new current path [27]. With this switch, current flows

through S6 and S2 during the negative half cycle of the active mode [27]. The derived topology has S2, S4, S5 and S6 as high frequency switches while S1 and S3 act as low frequency free-wheeling switches [27]. This topology creates new current paths that lower conduction losses as compared to the H5 topology. Table 2 shows a comparison between the proposed topology, H5 topology and H6 topology in terms of the number of conducting switches during the active states and freewheeling states and shows that the proposed modified H5 topology has fewer conducting switches during either state.

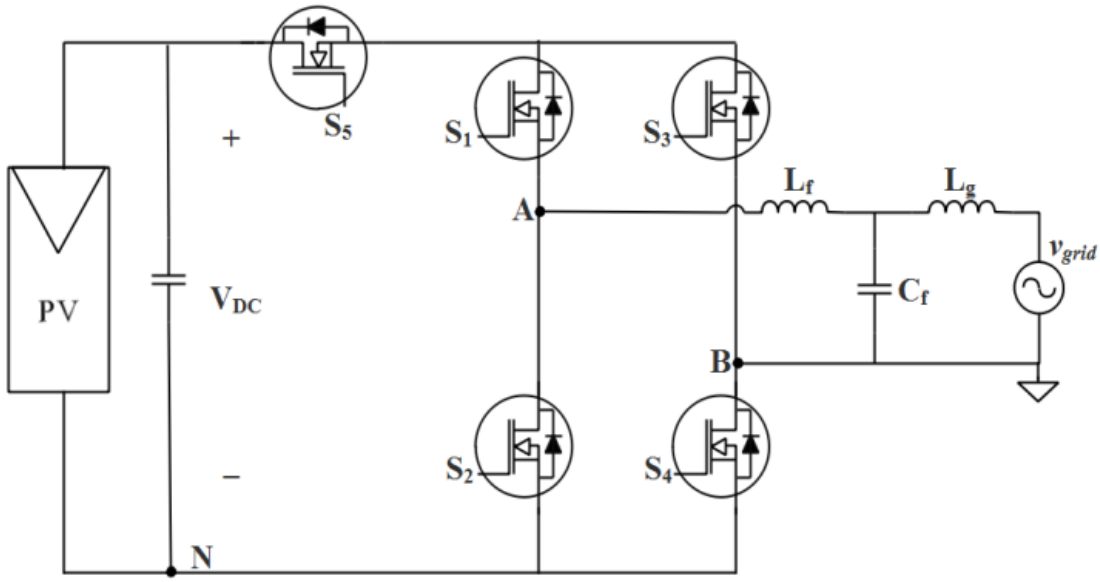

Figure 22. Single phase H5 Inverter topology.

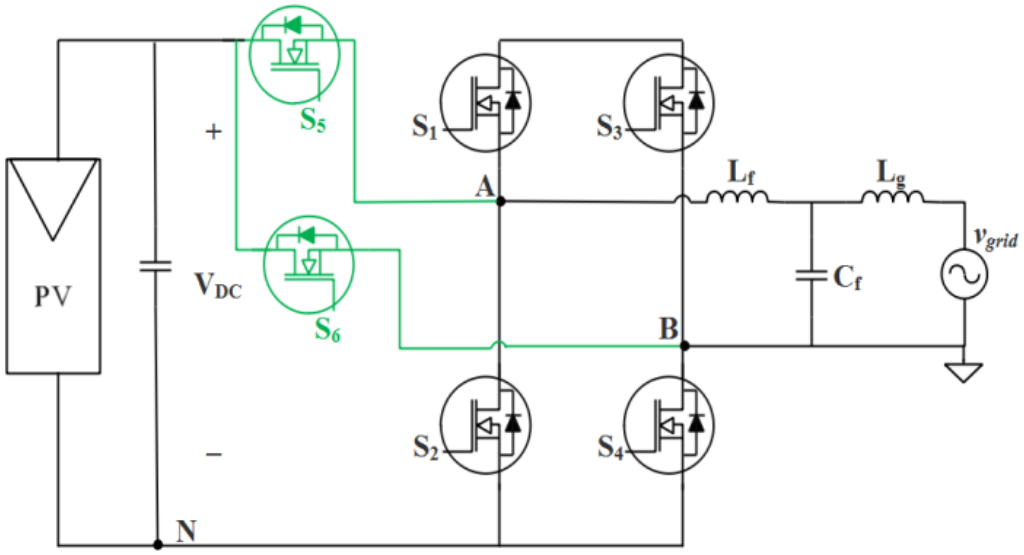

Figure 23. Proposed modified single phase H5 inverter topology.

Table 2. Comparison of H5, H6 and modified H5 topologies.

Topology type	H5	H6	Modified H5
Total number of switching devices	5	6	6
Number of conducting devices (V > 0)	3	3	2
Number of conducting devices (V < 0)	3	3	2
Number of conducting devices during active states	6	6	4
Number of devices during freewheeling states	2	2	2

3.2.2 Operation mode analysis in PSIM

The gate drive signaling sequence of the proposed topology are shown in Figure 24, where v_g is the grid voltage, I_{ref} is the reference current of the system, and v_{gs1}, v_{gs2}, v_{gs3}, v_{gs4}, v_{gs5} and v_{gs6} are the gate drive signals of switches S1, S2, S3, S4, S5 and S6, respectively for unity power factor [26]. Modes of operation of the proposed topology are shown in Figure 25 [27].

There are four operation modes to generate inverter output voltage as shown in figure 8 [27]. In Mode 1, S1, S4 and S5 are turned ON, for the positive half-period in the active state with all other switches turned OFF [27]. The current during this mode flows through S4 and S5. $V_{AB} = V_{DC}$, and the Common Mode voltage

$$V_{CM} = \frac{V_{A\,N} + V_{BN}}{2} = \frac{V_{DC} + 0}{2} = \frac{V_{DC}}{2} \tag{5}$$

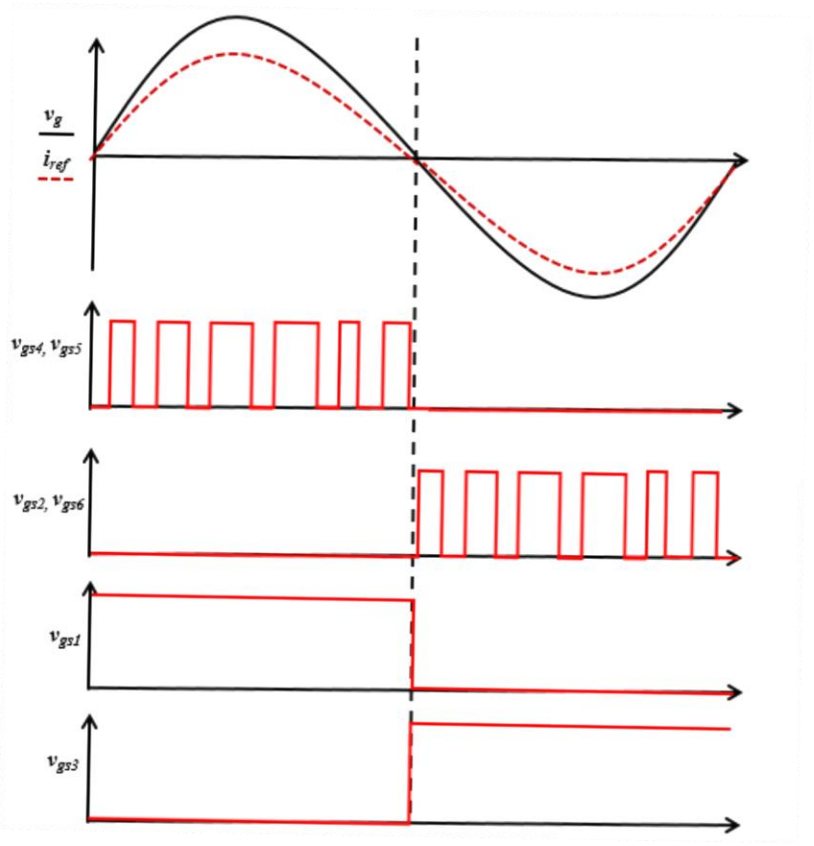

Figure 24. Gate drive signaling for modified H5 inverter.

In Mode 2, S1 is turned ON, for the positive half-period in the freewheeling state and all other switches are turned OFF [27]. The current during this mode flows through S1, and the anti-parallel diode of S3. $V_{AB} = 0$, and

$$V_{CM} = \frac{V_{A\,N} + V_{BN}}{2} = \frac{\left(\frac{V_{DC}}{2} + \frac{V_{DC}}{2}\right)}{2} = \frac{V_{DC}}{2} \tag{6}$$

In Mode 3, S2, S6 and S3 are turned ON, for the negative half-period in the active state and all other switches are turned OFF [27]. The current during this mode flows in the opposite direction through S6 and S2. V_{AB} = - V_{DC}, and

$$V_{CM} = \frac{V_{A\,N} + V_{BN}}{2} = \frac{0 + V_{DC}}{2} = \frac{V_{DC}}{2} \tag{7}$$

In Mode 4, S3 is turned ON, for the negative half-period in the freewheeling state and all other switches turned OFF [27]. The current during this mode flows through S3, the anti-paralleled diode of S1. V_{AB} = *0*, and

$$V_{CM} = \frac{V_{A\,N} + V_{BN}}{2} = \frac{\left(\frac{V_{DC}}{2} + \frac{V_{DC}}{2}\right)}{2} = \frac{V_{DC}}{2} \tag{8}$$

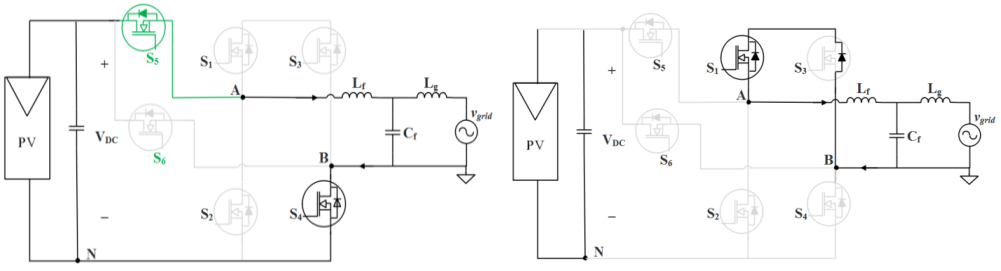

(a) (b)

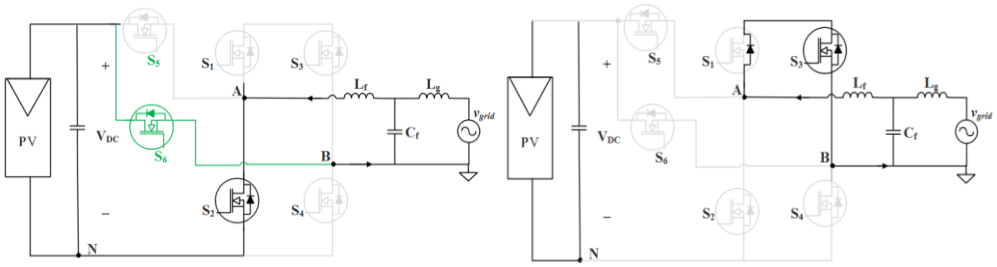

(c) (d)

Figure 25. Operating modes (a) Active positive half cycle, (b) Zero state positive half cycle, (c) Active state Negative half cycle and (d) Zero state Negative half cycle.

3.2.3 PSIM input parameters for power loss calculations

The topology in figure 23 was simulated in PSIM with Si MOSFET, GaN HEMT and AlGaN/GaN HEMTs as the switching devices in separate models [27]. The DC link voltage in the figure 23 was set to 400 V so 650-V rated devices are required for the switching devices in this application [27]. The Infineon Si CoolMOS MOSFET (IPW60R045CP), GaN Systems GaN HEMT (GS66516T) and MASTERGAN1 AlGaN/GaN 2-in-1 HEMTs manufactured by STMicroelectronics were selected based on them having similar operating parameters [27]. The maximum VDS for all three devices were rated at 650 V with $R_{DS(ON)}$ values of 45 mΩ, 25 nΩ and 150 mΩ for the IPW60R045CP, the GS66516T and the MASTERGAN1 respectively. Table 3 shows the operating parameters set for all the models in PSIM [27].

Table 3. Operating parameters for PSIM models.

Parameter	**Value**
System Power	5 kW
Input Voltage	400 V
Grid Voltage	120 V
Grid Frequency	60 Hz

Switching Frequency	50 kHz
Input Capacitance (CDC)	1 mF

The Infineon Si CoolMOS MOSFET (IPW60R045CP), the GaN Systems GaN HEMT (GS66516T) and the STMicroelectronics AlGaN/GaN 2-in-1 HEMTs (MASTERGAN1) were used in PSIM as the switches in the schematic in figure 23 with switching sequence for each switching device as shown in figure 24. The average power losses for each of the switches were then obtained from PSIM to be fed to COMSOL models as the heat sources.

PSIM calculates instantaneous power losses and graphs it on SIMVIEW. These power losses consist of the conduction losses and the switch ON and OFF losses. PSIM uses the ideal switch models to calculate the power losses of the devices available in its database. The on-resistance $R_{DS(ON)}$ is a function of the junction temperature [114], expressed as:

$$R_{DS(ON)} = R_{DS(ON)\_b} \times (1 + K_T \times (T_j - T_{j\_b})) \tag{9}$$

where $R_{DS(ON)\_b}$ and T_{j_b} are the base values of $R_{DS(ON)}$ and the junction temperature, T_j, at the test conditions, normally at 25 ˚C. The temperature coefficient, K_T, [114] is expressed as:

$$K_T = \frac{\left(\frac{R_{DS(ON)}}{R_{DS(ON)\_b}} - 1\right)}{(T_j - T_{j\_b})} \tag{10}$$

This can be written in terms of the normalized value as:

$$K_T = \frac{\left(R_{DS(ON\_normalized)} - 1\right)}{(T_j - 25)} \tag{11}$$

The PSIM simulation calculates the voltage and currents of the switch and diode at each instant based on the ideal models [114]. The power loss calculations are done using these voltage and current values.

The *switch conduction loss* is calculated as:

$$Switch\ Conduction\ Loss = I_D \times I_D \times R_{DS(ON)} \tag{12}$$

where I_D is the drain current.

The *Switch turn-on loss* is calculated as:

$$Switch\ turn-on\ loss = E_{ON} \times f \tag{13}$$

Where E_{ON} is the switch turn-on energy loss, and f is the frequency as defined in the input parameters [114].

The *Switch turn-off loss* is calculated as:

$$Switch\ turn-off\ loss = E_{OFF} \times f \tag{14}$$

Where E_{OFF} is the switch turn-off energy loss. E_{ON} and E_{OFF} are calculated based on the values of gate current, transfer capacitances, and gate charges of the switching devices.

3.3 Thermal Model definition of Power modules in COMSOL using PSIM data

The use of simulation software for modelling thermal performance of heatsinks is not new and has been reported in literature [123] [124] [125] [126] [127]. Commercial software like COMSOL Multiphysics, FLUENT, ANSYS, Pro-MECHANICA etc. are prime examples of simulation software that use numerical methods, Finite Element and Finite Volume Methods (FEM and FEV) along with Computer Aided Design (CAD) tools to model the thermal performance of heatsinks [123] [124] [125] [126] [127]. Heatsink manufacturing companies like Mersen, Boyd Corp, Midas Information Technology Co. Ltd. etc. provide purchasable software as well as online tools that can be used to simulate the thermal properties of their heatsinks as per the customer's requirements [27].

COMSOL Multiphysics was used to create three 3D models of a 6-pack module with Si, GaN and AlGaN/AlGaN switches as their respective power devices [27]. Heatsinks were added to these modules to reduce the structures' temperatures and to compare each semiconductors' thermal performance [27]. Boyd Corp's online tool AAVID Genie was used to verify the results of the simulated structures with their commercially available heatsinks that were simulated in COMSOL [27]. The Joule heating generated by electric currents passing through each of the modules were obtained from calculations made in PSIM which acted as the heat sources for COMSOL [27]. A stationary study was created for each model to study the steady state effects of the Joule heating on the temperature of each structure [27]. The physical dimensions the 6-pack module were obtained from [128]. The dimensions of the heatsink for the GaN and

AlGaN/GaN models were made smaller to demonstrate the superiority of these WBG materials in terms of heatsink requirements for similar steady state temperatures [27].

3.3.1 Model Geometry

The internal structure of the CREE 1200V, 50A 6-pack SiC MOSFET module consists of multiple layers and components. The dimensions of this internal structure were obtained from [128] to create the 3D CAD model of the module in COMSOL, which acted as the template for simulating all the other semiconductor 6 pack models [27]. The module starts from the bottom to the top with a Copper (Cu) Baseplate, a solder layer, a Copper layer, an Aluminum Nitride (AlN) layer and a Copper layer [128]. Six sets of SiC MOSFETs and Diodes are soldered on top of the final Copper layer [128]. These six SiC MOSFETs and diodes were replaced by six Si MOSFETs and diodes while keeping the multiple layers of other materials the same for the Si 6 pack model. The model for GaN consisted of all the layers as the Si module with the exception of the diode and its corresponding solder layer [27]. The dimensions of the HEMTs for the GaN module were obtained from [129]. Each MASTERGAN1 HEMT package has two HEMTs in a single unit so only 3 of these HEMT packages were placed on the 6 pack module for the AlGaN/GaN model. Figures 26, 27 and 28 show the 3D view, the dimensioned yz-plane view and the xy-plane view of the Si module while figures 29, 30 and 31 show the same for the GaN module [27]. Figures 32, 33 and 34 show these views for the AlGaN/GaN module. The yz-plane views are scaled to make all the layers viewable [27].

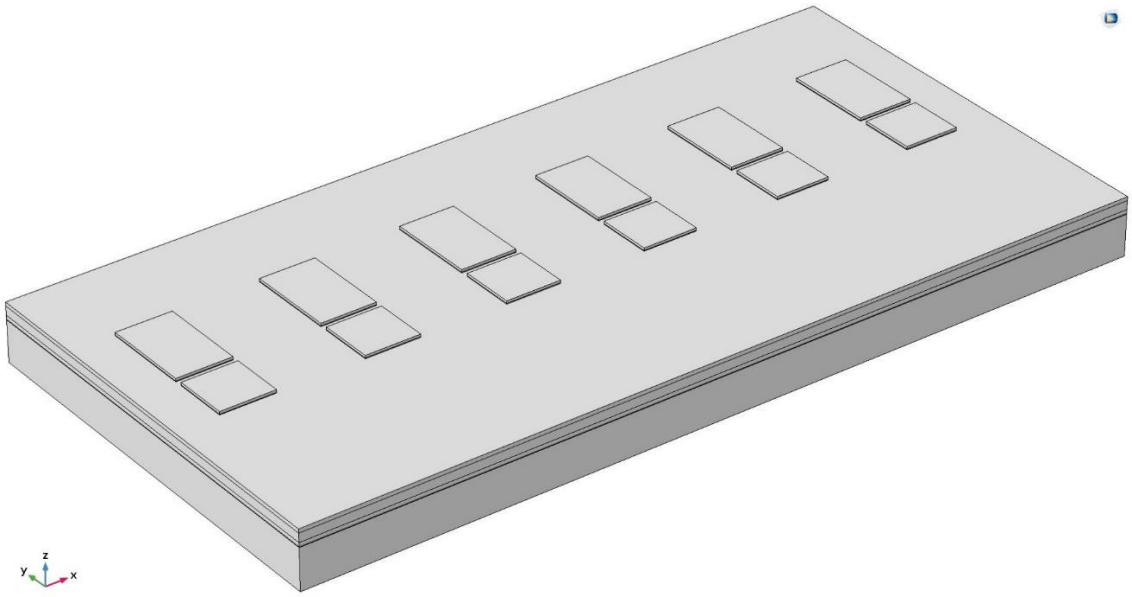

Figure 26. 3D view of Si Module.

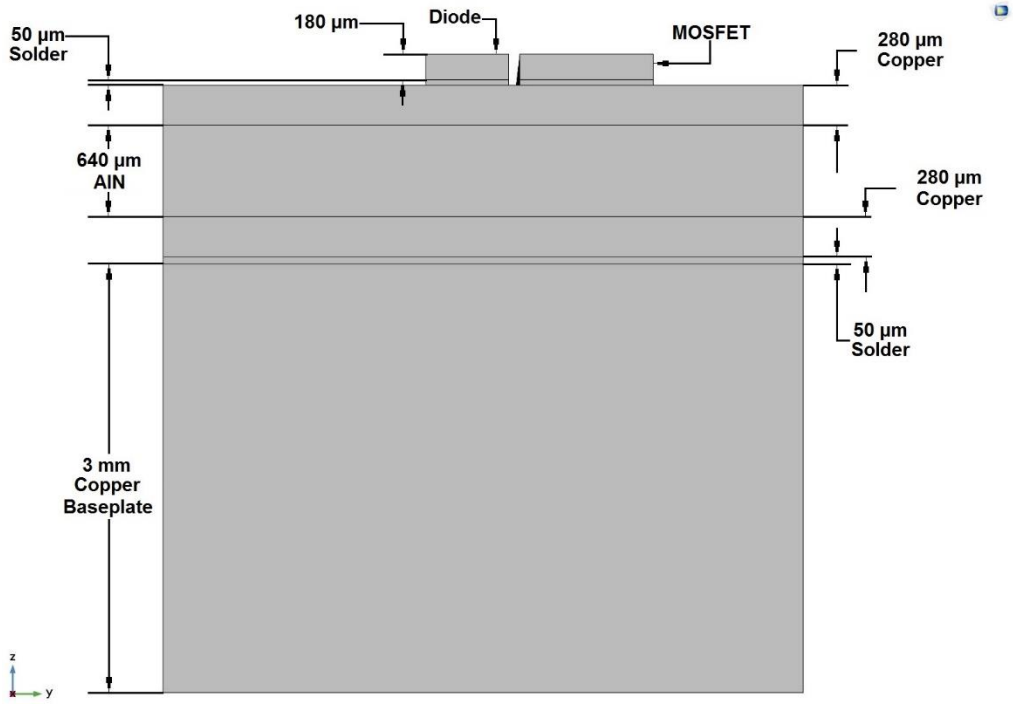

Figure 27. yz-plane view of Si Module.

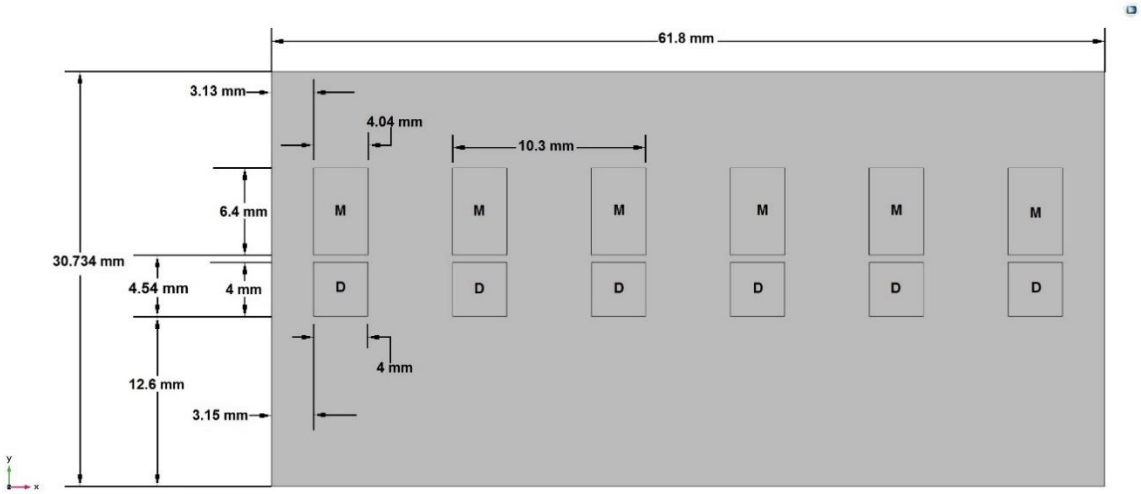

Figure 28. xy-plane view of Si Module.

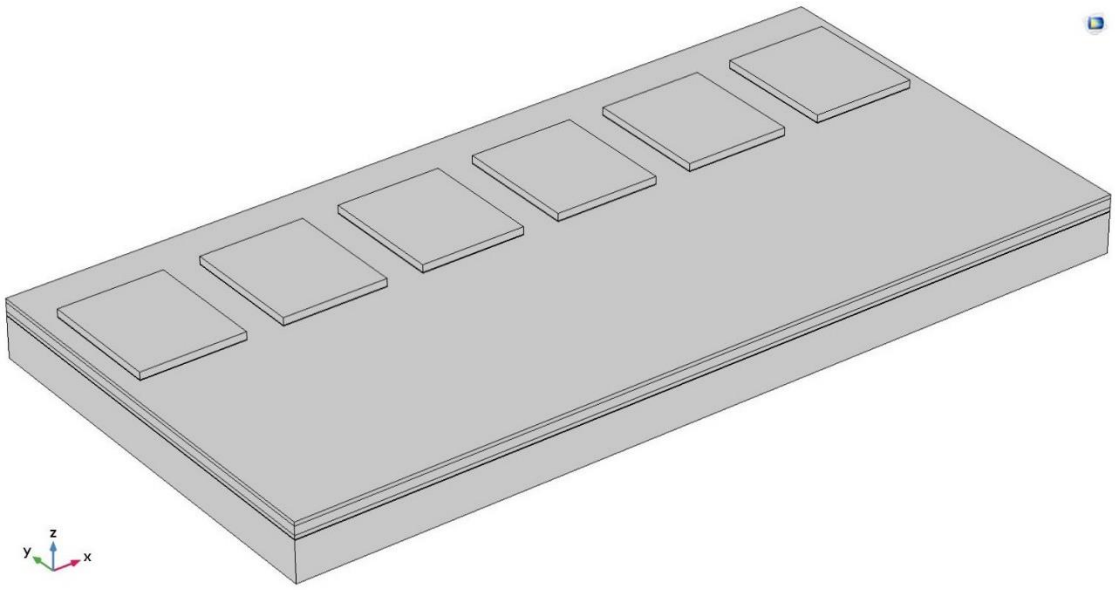

Figure 29. 3D view of GaN Module.

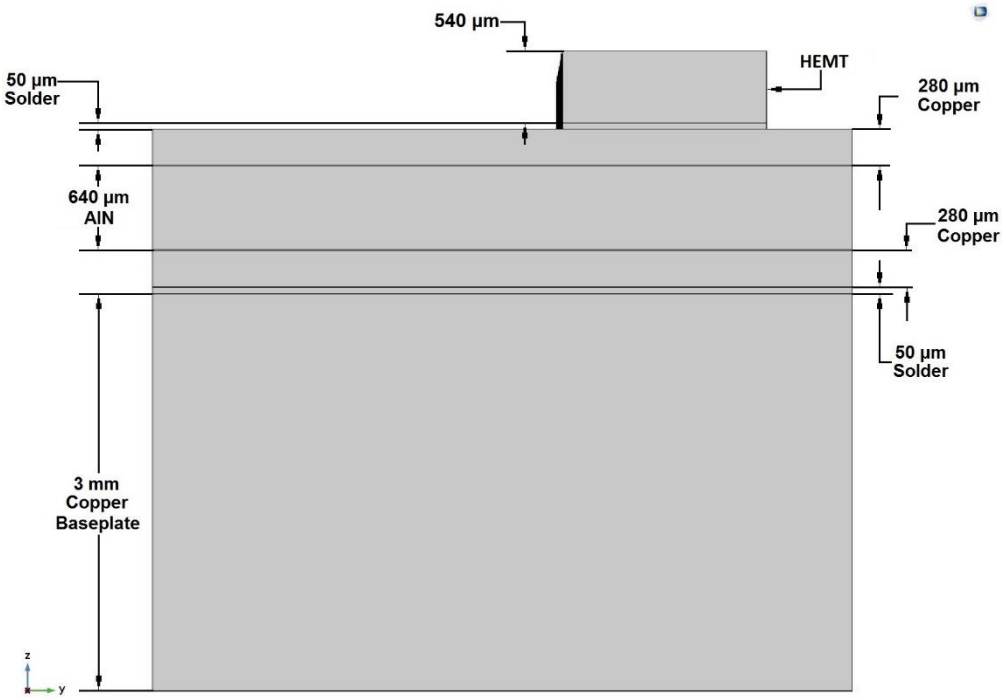

Figure 30. yz-plane view of GaN Module.

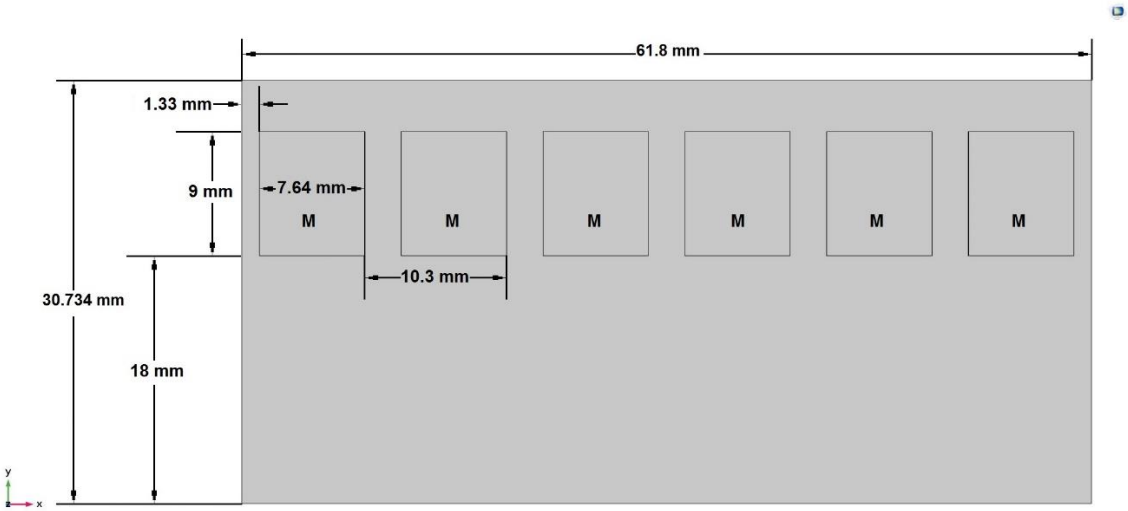

Figure 31. xy-plane view of GaN Module.

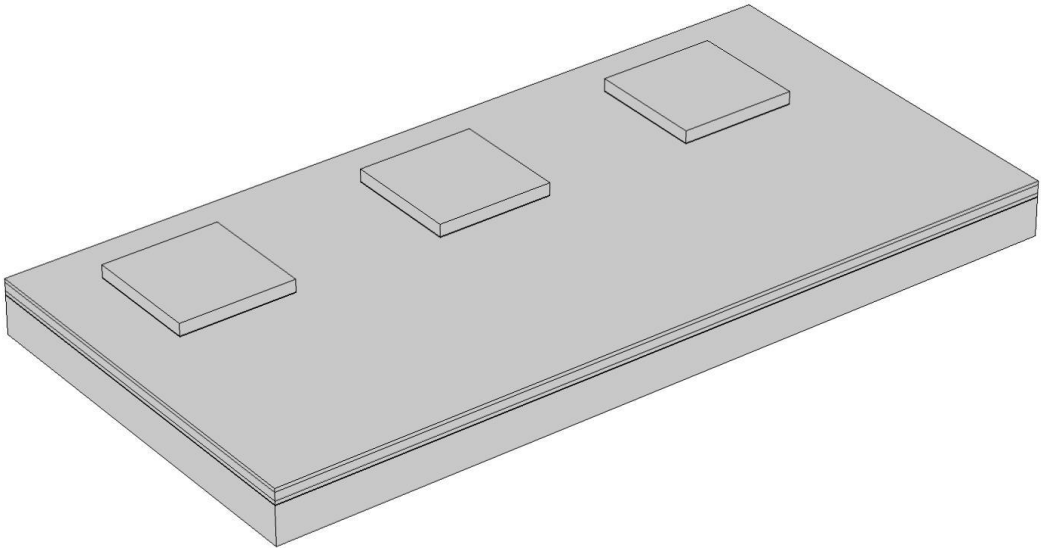

Figure 32. 3D view of AlGaN/GaN Module.

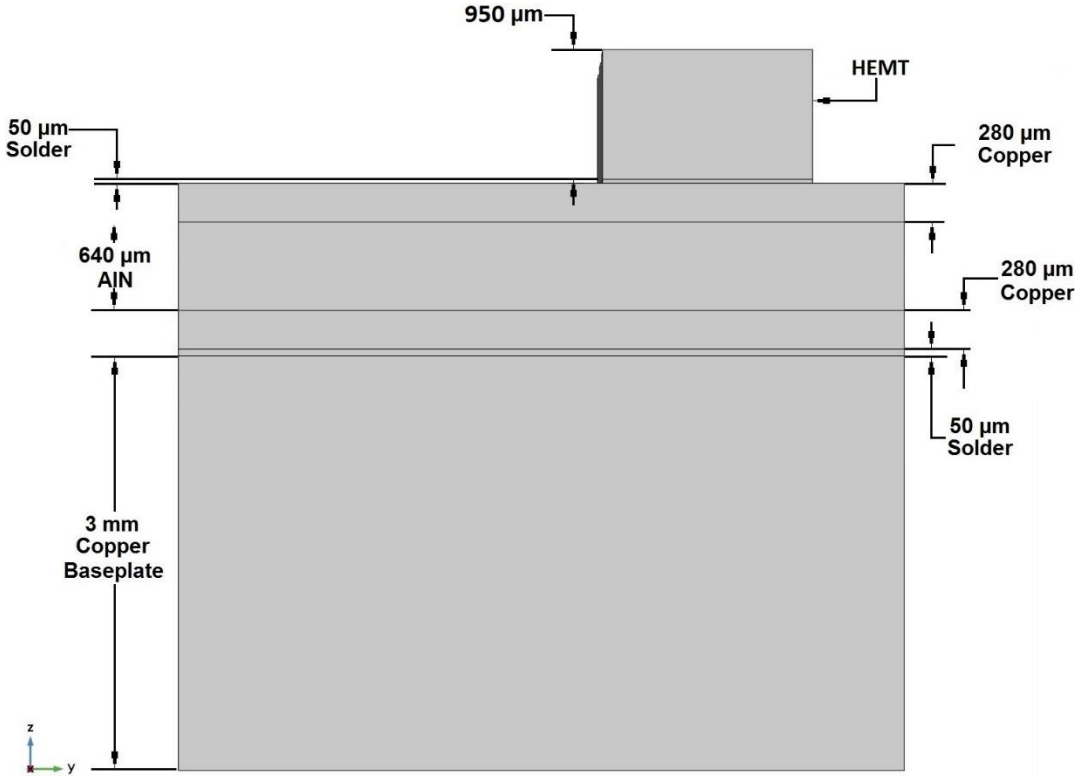

Figure 33. yz-plane view of AlGaN/GaN Module.

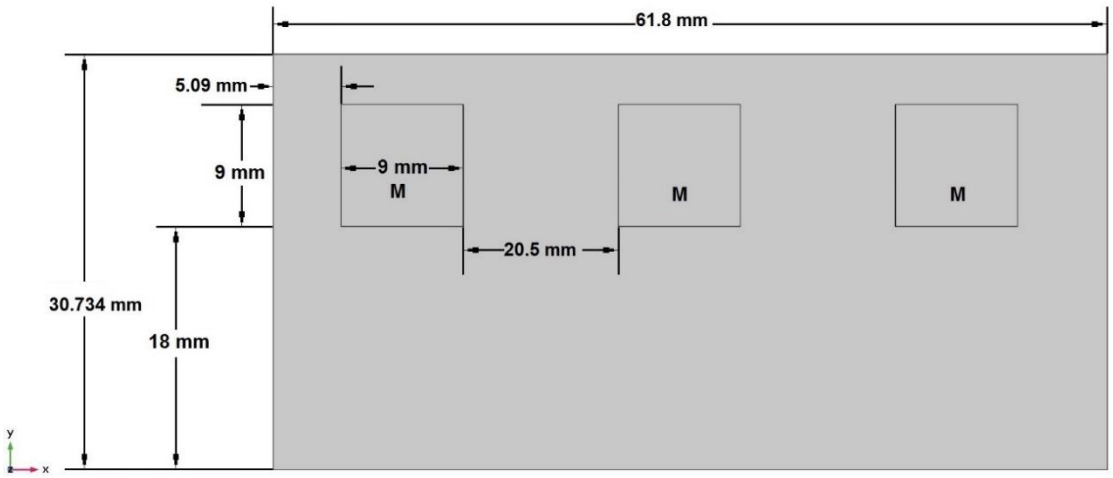

Figure 34. xy-plane view of AlGaN/GaN Module.

The final layer of each model consisted of an Aluminum (Al) heatsink which rested on top of the switching device and diode layers [27]. The dimensions of the heatsinks were obtained from Boyd Corp's online tool AAVID [27]. These dimensions were based on real world heatsinks sold by Boyd Corp that would make the maximum temperatures of the module-heatsink combinations below 100 ºC [27]. Figures 35 and 36 show the heatsinks used for the Si and GaN modules respectively [27]. Each heatsink consists of a solid Aluminum block of dimensions 141.8 mm × 104.3 mm × 6.6 mm. 16 aluminum fins of width 1.134 mm and separated by 6.8 mm were added on top of this block with heights of 33.5 mm, 10.89 mm and 10 mm for the Si, GaN and AlGaN/GaN models respectively [27]. These height values were selected to obtain similar minimum temperatures for the three models [27].

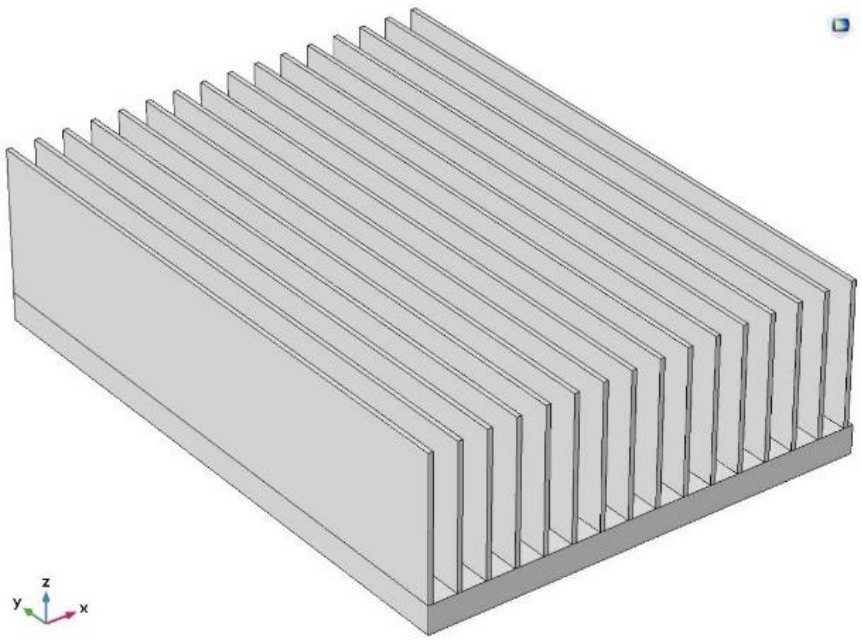

Figure 35. Heatsink for Si Model.

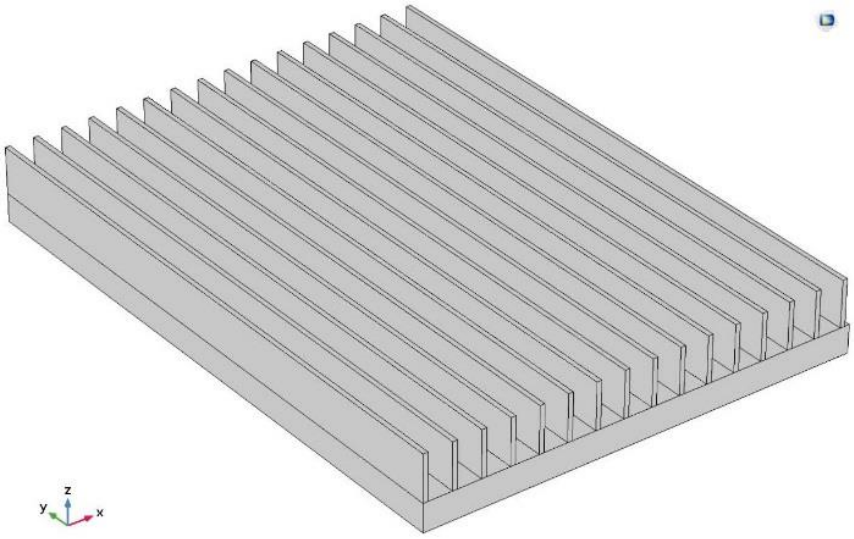

Figure 36. Heatsink for GaN Model.

3.3.2 Material Properties

The physical material properties used for the models were the Density (ρ), the Heat capacity at constant pressure (C_p) and Thermal conductivity (k) [27]. Only these

three properties were used for the simulations because heat transfer in solids was the only physics being studied [27]. The materials were assumed to be isotropic with every property considered to be constant in all 3 directions [27]. The properties for all materials simulated in the models except for the Solder were obtained from built-in libraries in COMSOL [27]. SAC396 solder, an alloy of Tin, Silver and Copper, was chosen for the models and its properties were obtained from [130]. Table 4 shows these three material properties for all the materials used.

Table 4. Material properties used for heatsink models.

Symbol	Unit	Cu	SAC396	AlN	Si	GaN	AlGaN	Al
ρ	kg/m^3	8960	7400	3260	2329	6070	6070	2700
C_p	J/(kg.K)	385	220	740	700	490	490	900
k	W/(m.K)	400	61.1	160	131	130	50	238

3.3.3 Heat Transfer Physics modelling

The heat transfer in solids physics module of COMSOL was used to simulate the thermal performance of each model [27]. The heat losses calculated from PSIM for each switching device in each semiconductor model were input as heat sources for the simulations [27]. As the heatsinks dissipate thermal energy from the heat generated by the switches to the surrounding air, a convective heat flux boundary condition for all heatsink surfaces in contact with air was set up [27]. The convective heat transfer coefficient was given a value of 10.45 $W/m^2.K$ to simulate non-forced free flowing air [27]. The initial temperature of the structures and surrounding air was set to room

temperature i.e. 293.15 K or 20 ˚C [27]. Using these inputs and boundary conditions, COMSOL solved the heat equation in solids to obtain the temperature profiles of each model [27].

4. Results and Discussions

4.1 Results for VDMOSFETs models

The VDMOSFET structure with the geometry and high doping concentrations shown in figure 19 was simulated for Si, SiC and GaN as the semiconductor material in both 2D and 3D with high dopant concentrations for normal conduction conditions [16] [17]. The same was done in 2D for AlGaN. The input variables for each model were the VDS and VGS values with the source terminal remaining at ground potential. The Drain to Source voltage (VDS) was swept from 0 V to 55 V for the 2D models and 0 V to 45 V for the 3D models while the Gate to Source voltage (VGS) was swept from of 0 V to 20 V for both 2D and 3D models for the Si, SiC and GaN models and for the 2D AlGaN model, VGS was swept from 0V to 20 V and VDS from 0 V to 49 V. While solving for multiple input voltages that cause different currents to flow within the semiconductor, it is best to ramp up input voltages slowly so as to initialize the solutions for subsequent input parameters [118]. In order to achieve this, auxiliary parametric sweeps for VGS and VDS were configured in the study steps of the model so that solutions from one set of input voltage values were reused as initial solutions for the next set of input voltages. The values for VGS and VDS were not ramped up in equal voltage intervals as the simulations solutions tended not to converge at certain specific values. This was also the reason for VDS not being swept to 55 V in 2D and 3D models for all materials.

COMSOL was configured to run the parametric sweeps first by keeping a VGS value constant and changing the VDS values until all the VDS values were solved for, with the solution for one VDS value acting as the initial solution for the next. For the next VGS value, the initial solution for VDS = 0 V for the previous VGS value was used as an initial solution for that VGS value at VDS = 0 V.

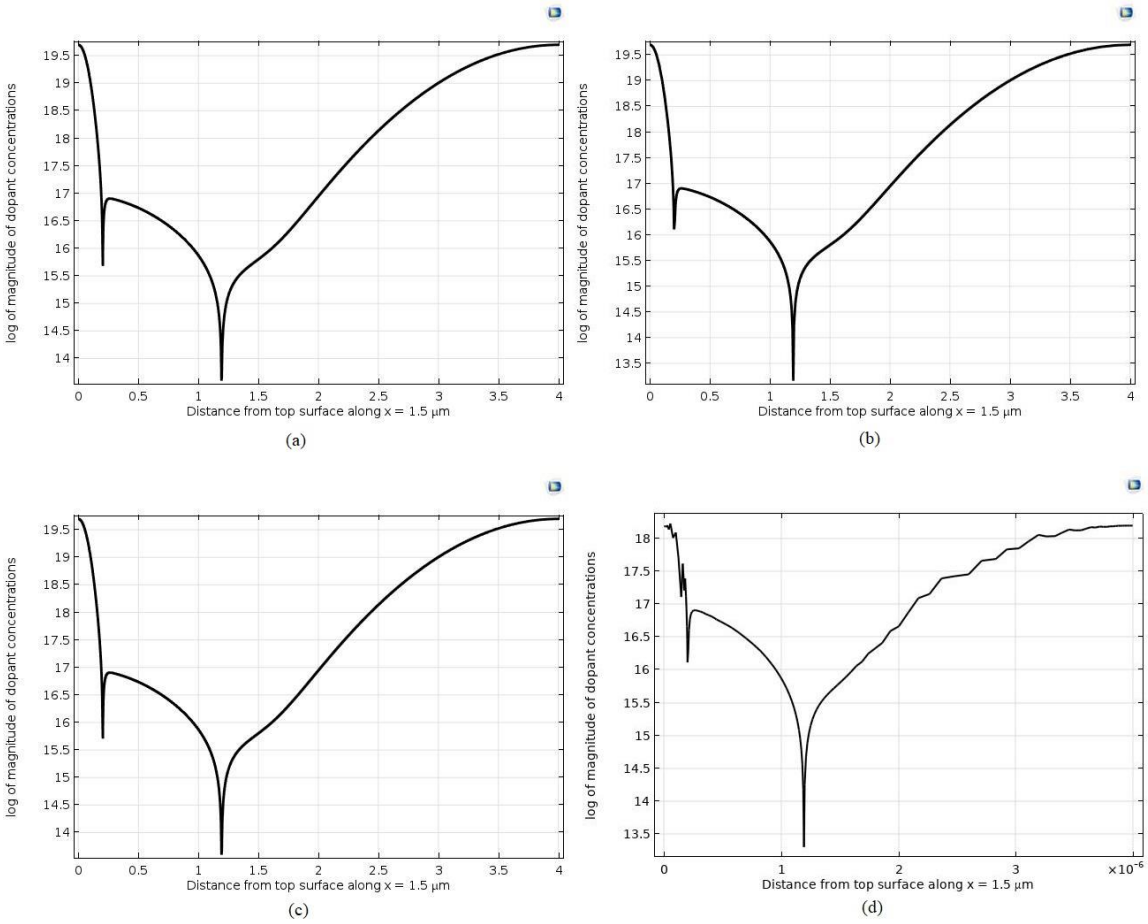

Figure 37. Doping profiles for (a) Si, (b) SiC, (c) GaN and (d) AlGaN VDMOSFET structures at x = 1.5 μm for normal conduction.

Figure 37 shows the doping profile for each of the three MOSFETs on a vertical line going through the heavily n-doped region of the device structure at 1.5 μm. The

slight differences in the doping profile for each material arises from the varying material properties for each semiconductor material.

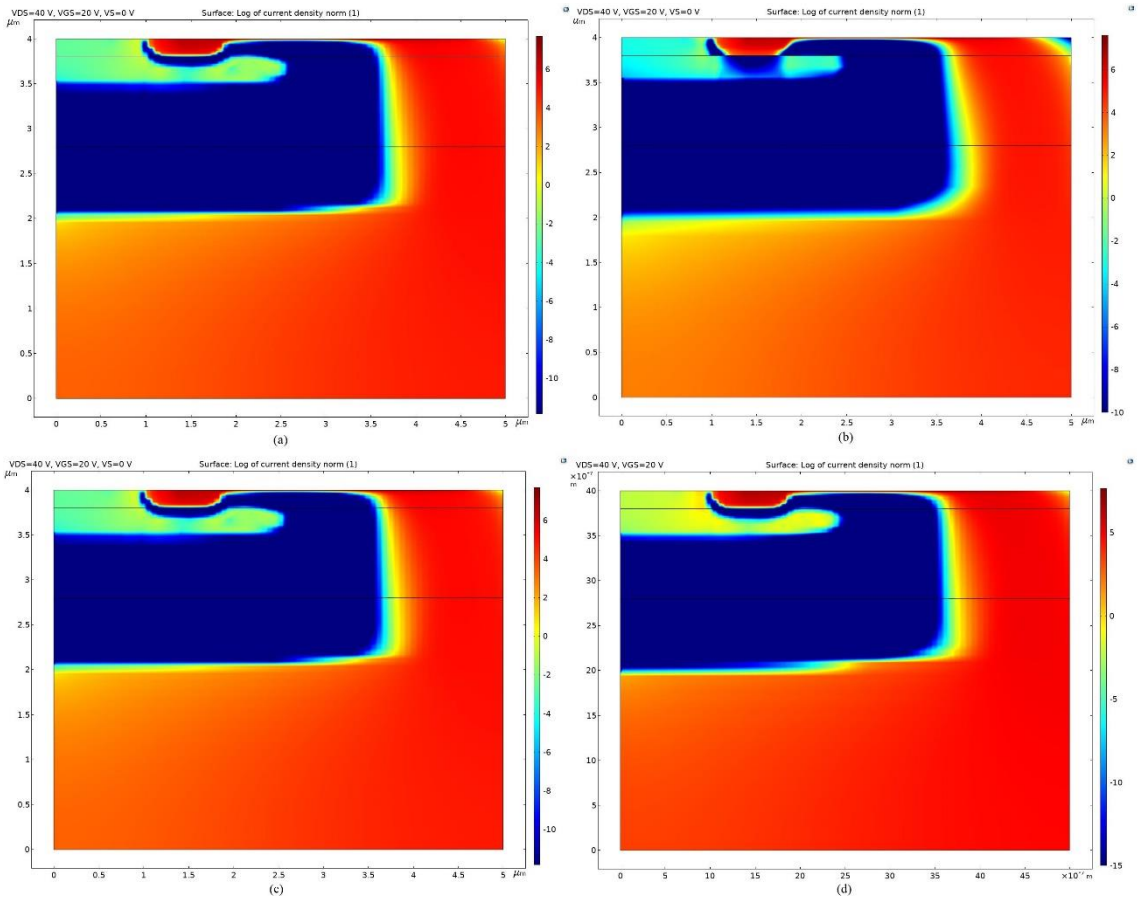

Figure 38. 2D log of norm of current density for (a) Si, (b) SiC, (c) GaN and (d) AlGaN VDMOSFETs at VGS = 20 V and VDS = 40 V for normal conduction.

Figure 38 shows the log of the norm of current densities for one combination of terminal voltages at VGS = 20 V and VDS = 40 V for the 2D models. The creation of the channel from the heavily n-doped region through the p-doped region into the Drain terminal can be seen in this figure. It also shows current density to be highest in the channel region right below the Gate terminal while the p-doped region acts as a barrier for the flow of current [16].

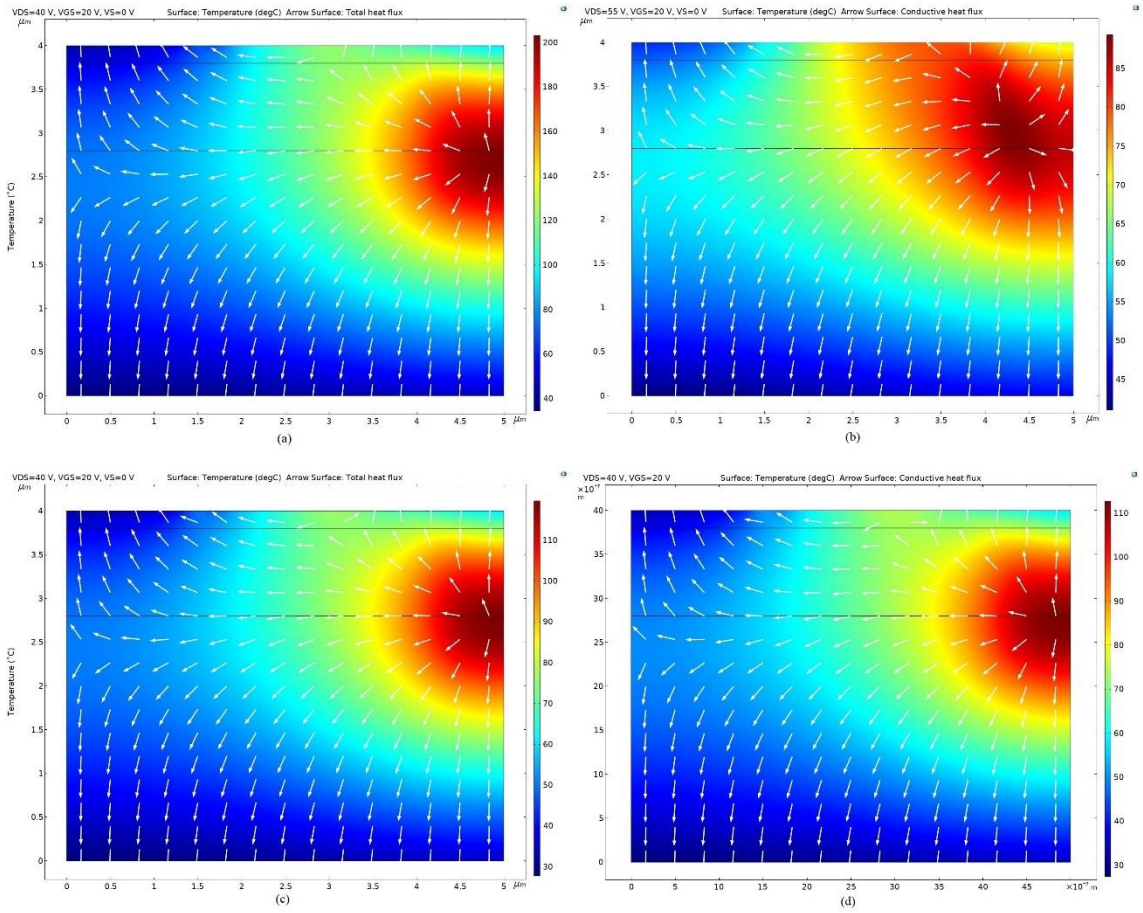

Figure 39. 2D Temperature profile for (a) Si, (b) SiC, (c) GaN and (d) AlGaN VDMOSFETs at VGS = 20 V and VDS = 40 V for normal conduction.

The temperature profile for the 2D structures is shown in figure 39 for the same combination of VGS = 20 V and VDS = 40 V. This figure also shows the direction of heat flux within the structures. It is clear to see that the region with the highest current density in the channel region below the Gate terminal also has the highest temperature values. The heat is generated by the high current densities at this region and flows away from it towards the Source, Gate and Drain terminals contacts. The temperature distribution within the structures for each material are similar to each other. However, the maximum temperatures in Si are highest and the ones for SiC are the lowest [16].

Temperatures are also lower for the GaN and AlGaN models with the AlGaN model having a slightly lower maximum temperature at these operating conditions.

Figures 40, 41 and 42 show the log of the norm of current densities (on the left) and temperature (on the right) profiles of the 3D VDMSOFET structures for VGS = 20 V and VDS = 45 V. The figures also show the direction of conventional current flow in the current density plot and the position of maximum and minimum temperatures in the temperature plot. It is clear from these plots that the areas with high current densities also have higher temperature values, which are located below the gate terminal. SiC also demonstrates the lowest maximum temperature value among all three semiconductor materials as also shown in [17]. The arrows in the current density plots show the direction of current densities within the structure. The creation of the channel for charges to flow from the drain to the source can be seen by these arrows. These plots are for the maximum voltage values applied in the simulations.

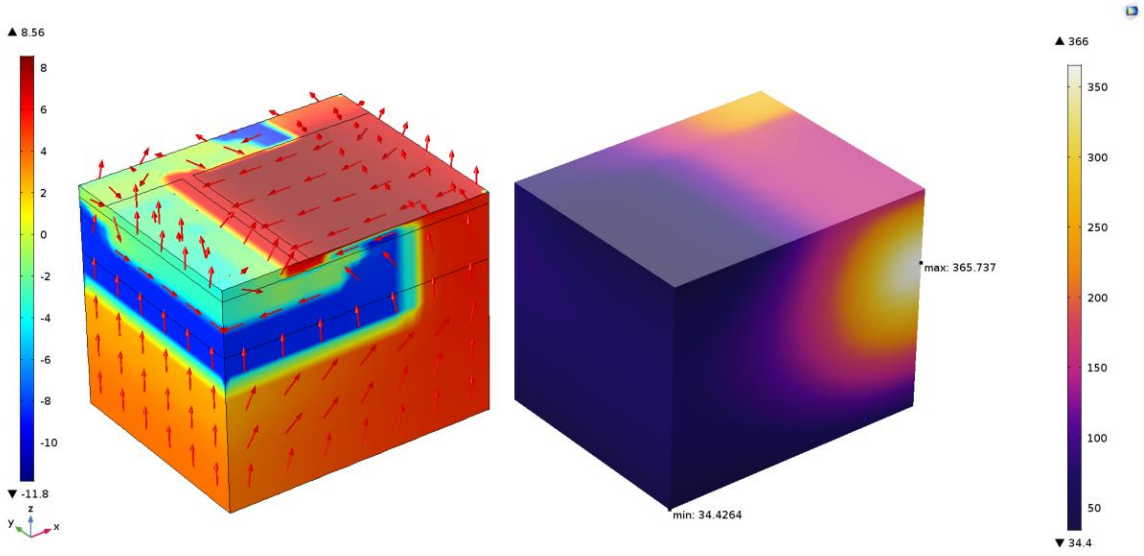

Figure 40. Log of norm of current density and temperature profile in 3D for Si at VDS 20 V and VGS 45 V for normal conduction.

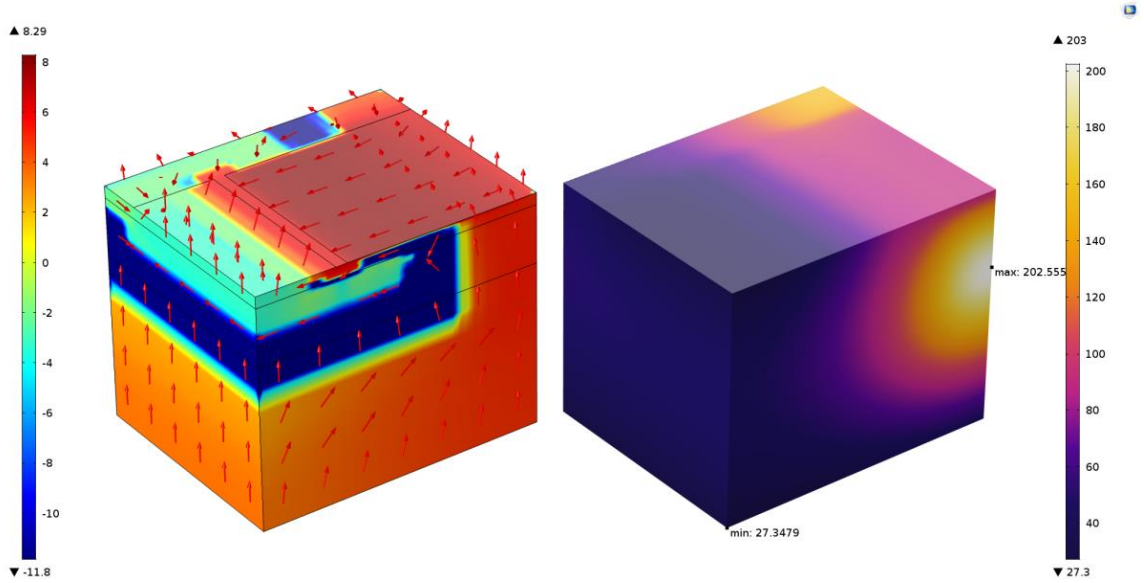

Figure 41. Log of norm of current density and temperature profile in 3D for GaN at VGS 20 V and VDS 45 V for normal conduction.

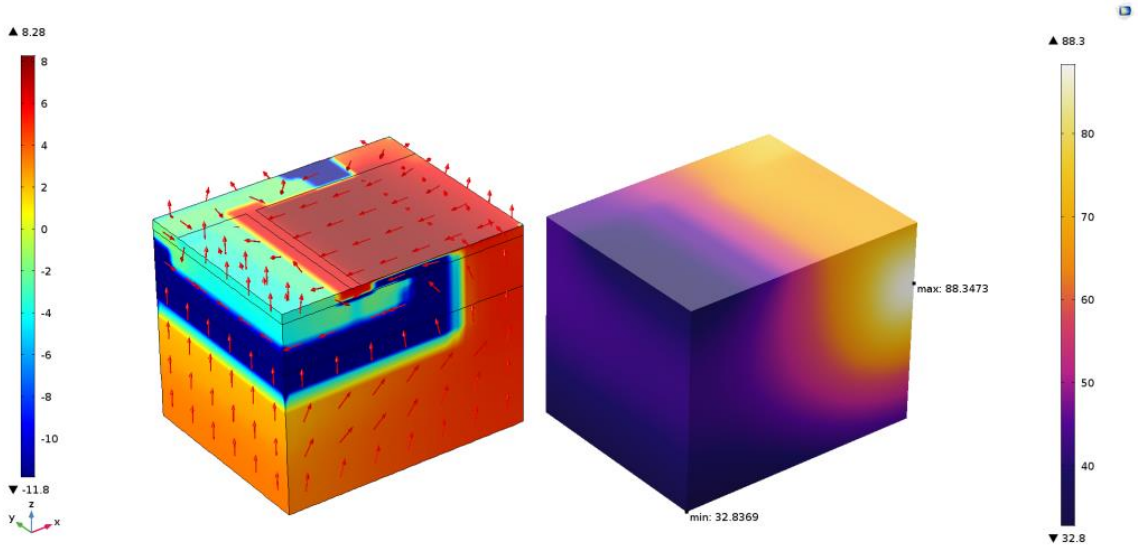

Figure 42. Log of norm of current density and temperature profile in 3D for SiC at VGS 20 V and VDS 45 V for normal conduction.

Figures 43 and 44 are the graphs for the maximum and average temperatures for each device in 2D for all terminal voltage combinations. The graphs clearly show that for the same terminal voltages, SiC has the lowest average and maximum temperatures while AlGaN has the second lowest very closely followed by GaN. The difference in average and maximum temperatures between Si and the other WBG materials start to become significantly large once the VDS is at 18 V and VGS is at 12 V. For most terminal voltages below these values, the average and maximum temperature differences between Si and SiC as well as Si and GaN/AlGaN were below 5 ˚C and 10 ˚C respectively. The maximum temperature for Si exceeded 280 ˚C for a VDS of 50 V and VGS of 20 V while for the same conditions, SiC, GaN and AlGaN had maximum temperatures of less than 90 ˚C, 180 ˚C and 145 ˚C.

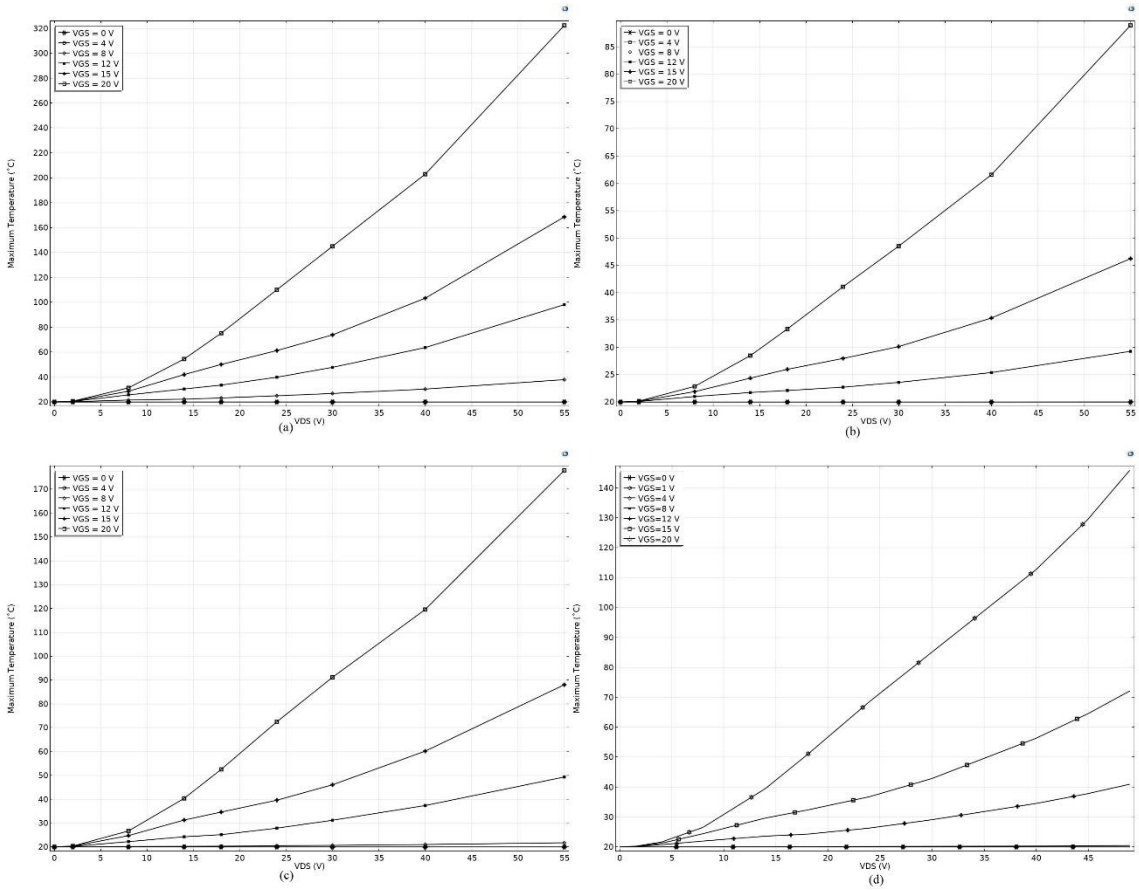

Figure 43. Maximum temperatures for (a) Si, (b) SiC, (c) GaN and (d) AlGaN VDMOSFETs for normal conduction.

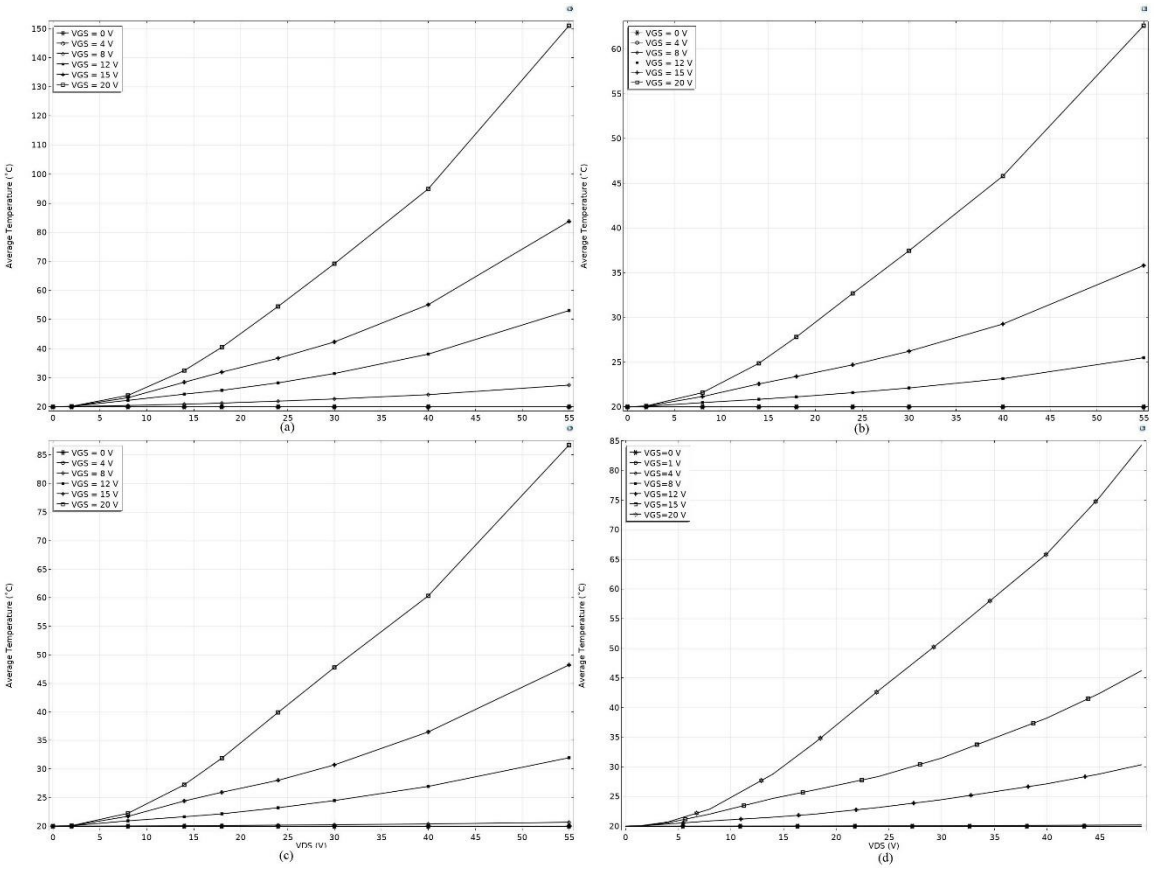

Figure 44. Average temperatures for (a) Si, (b) SiC, (c) GaN and (d) AlGaN VDMOSFETs for normal conduction.

Additionally, for the Si and GaN models with Surface to Ambient Radiation added to the Heat Transfer in Solids physics module under normal conduction conditions, the difference in temperatures for the models with and without the radiation effects added were extremely negligible. The maximum and average temperatures for the Si model with and without radiation effects had a difference of 0% for almost all VDS and VDS combinations and a highest difference of 0.0069% and 0.0026% respectively. There was a similar trend for the GaN models with and without radiation effects with most VDS and VGS combination giving 0% difference and a highest difference of -0.0056% and -0.0046% respectively for maximum and average temperatures.

These plots clearly show that for higher terminal voltages, the WBG materials perform significantly better in terms of keeping the device temperatures lower [16]. For the same operating voltages values, the maximum temperatures range from about 7% to 45% higher for Si as compared to AlGaN and the average temperatures have a similar trend ranging from 2% to 30% higher for Silicon. The maximum temperatures in the Si models were over 3.5 times as compared to SiC and about twice that of GaN in both 2D and 3D models at high dopant concentrations. The average temperatures were almost 3 times more in Si as compared to SiC and almost twice as compared to GaN for high dopant concentrations.

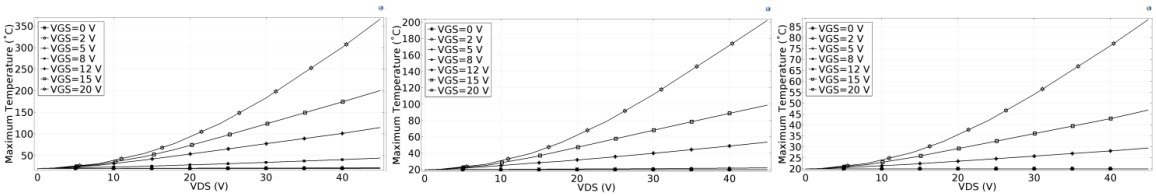

Figure 45. Maximum temperatures for (from left to right) Si, GaN and SiC 3D models.

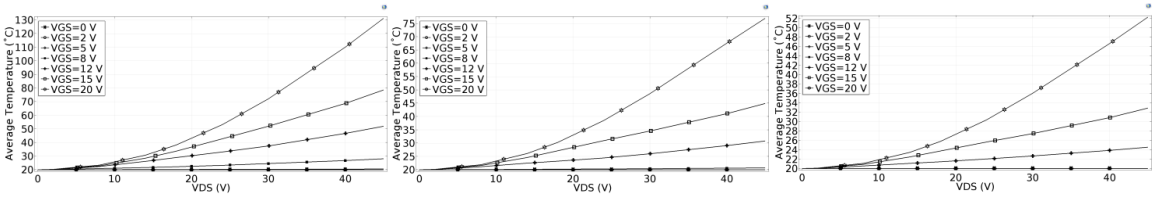

Figure 46. Average temperatures for (from left to right) Si, GaN and SiC 3D models.

Figures 45 and 46 show the maximum and average temperatures of the 3D models for the different input voltage values and the trend of rise in temperatures based on VGS values causing significant current to flow in the 3D structures is clearly seen in these plots. SiC again, shows the lowest average and maximum temperatures with GaN having the second lowest temperatures as compared to Si [17].

Similar to the high dopant concentrations for the Si, SiC and GaN models in 2D and 3D, the same model geometry, physics module definitions and initial conditions were setup for a new set of 2D models which were simulated with lower dopant concentrations to compare the Si, GaN and AlGaN VDMOSFET models. Figure 47 shows the temperature profiles for the three models at VGS = 20 V and VDS at 40 V. Figure 48 shows the current density profiles for the same voltage conditions for the three models. These figures show that the current starts flowing vertically from the Source to the Drain directly instead of through a small channel created by VGS below the Gate. Maximum temperatures for all three models occur near the left side of the structure directly below the Source where maximum current density is located. This is different from their current density and temperature profiles of the highly doped normal conduction models counterparts in figures 38 and 39 as higher current and temperatures occur on the right side directly below the Gate terminals. Electrons punch through the low doped p- region and cause current to flow vertically from the Drain to the Source. There is no narrow channel required for this current flow as compared to the normal conduction models and the current densities are almost 3 times higher. The temperatures are also more than twice than those in the normal conduction models.

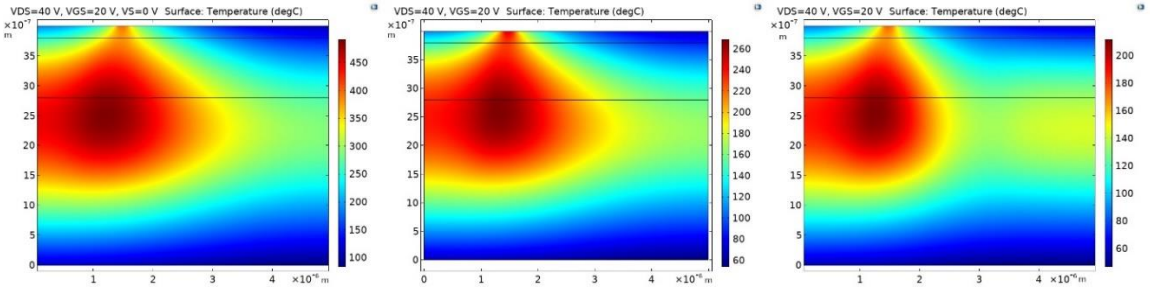

Figure 47. 2D Temperature profile for (from left to right) Si, GaN and AlGaN structures for VGS = 20 V and VDS = 40 V at lower dopant concentrations.

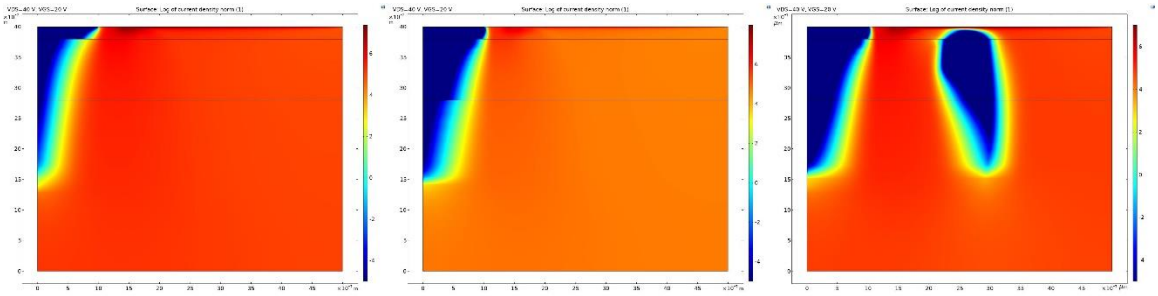

Figure 48. 2D Current density profile for (from left to right) Si, GaN and AlGaN structures for VGS = 20 V and VDS = 40 V at lower dopant concentrations.

The WBG materials show significantly lower temperatures as compared to Si with AlGaN having less than half of the highest temperatures as compared to Si. The maximum and average temperature graphs of figures 49 and 50 also show a similar trend with AlGaN having the lowest average and maximum temperatures as compared to Si. For the breakdown conditions of these low dopant concentrations, the current and temperatures start increasing at a much faster rate as compared to the normal operating conditions of high dopant concentrations. Conduction of current begins even at VGS = 0 V and so the temperatures start increasing rapidly for all three models. The maximum temperatures for the Si model are almost twice that for GaN and almost 2.5 times that for AlGaN. There is a similar trend for average temperatures as well with AlGaN having almost 1.4 times less average temperatures as compared to GaN.

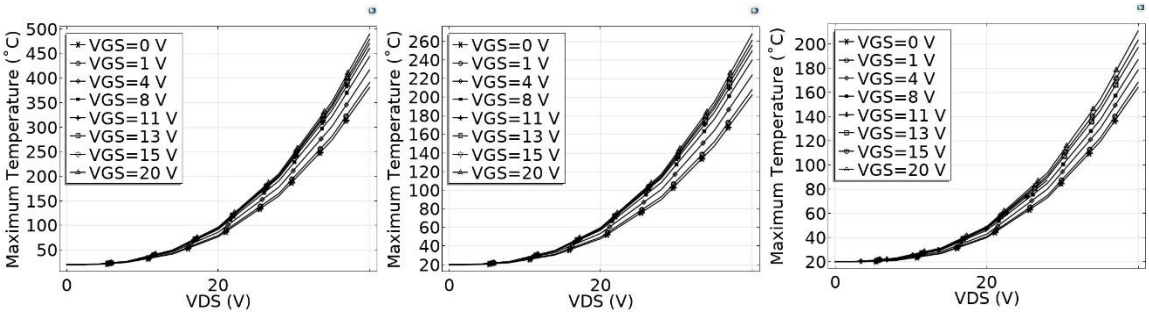

Figure 49. Maximum temperatures for (from left to right) Si, GaN and AlGaN structures in 2D at lower dopant concentrations.

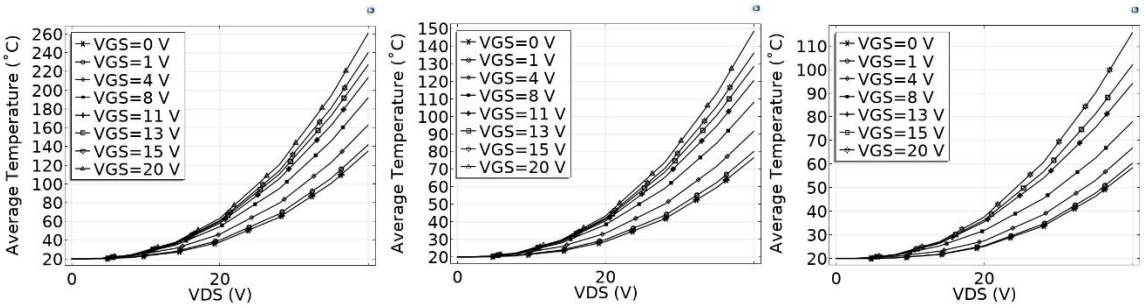

Figure 50. Average temperatures for (from left to right) Si, GaN and AlGaN structures in 2D at lower dopant concentrations.

4.2 Results for modified H5 inverter topology

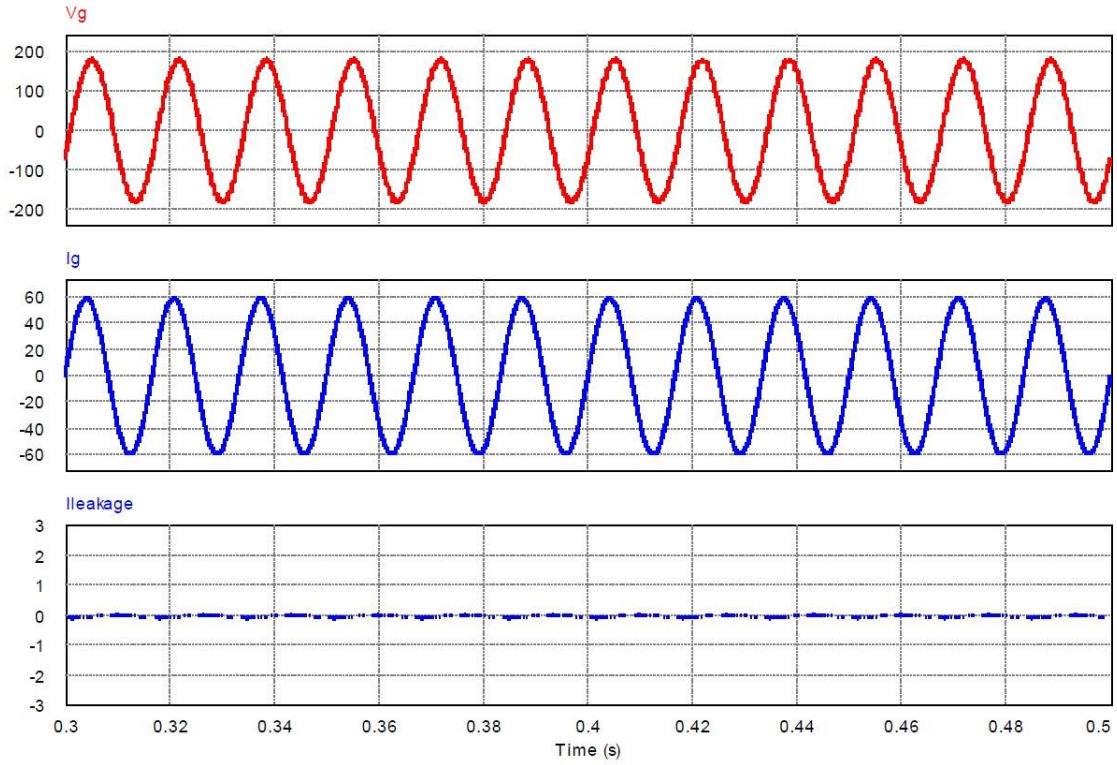

Figure 51. Grid Voltage (V_g), Grid Current (I_g) and Leakage Current ($I_{leakage}$) of the proposed modified H5 topology.

The modified H5 inverter topology of figure 23 was simulated in PSIM with the operating parameters listed in the previous chapter and its grid voltage, grid current and leakage current are shown in figure 51 [27]. The Root Mean Squared (rms) leakage current for this modified H5 topology is 11.7 mA which is much less than that of the H5 topology's 134.6 mA and very close to the H6 topology's 12.2 mA [27]. The Si, GaN and AlGaN/GaN switching devices, with their specifications mentioned in the previous chapter, were set in this modified H5 inverter to find the combined average power losses for the operating conditions of Table 3. For the Si model, these losses for the MOSFETs, going from left to right in figure 9, were 19.9 W, 19.9 W, 19.9 W, 19.9 W, 21.3 W and

21.3 W while losses for the GaN model were 7.1 W, 7.1 W, 7.1 W, 7.1 W, 12.6 W and 13 W respectively [27]. The power losses for the three AlGaN/GaN HEMTs in figure 12 were set to 14.2 W, 14.2 W and 25.6 W from left to right.

4.3 Heatsink simulation results

The power loss values obtained from PSIM for the Infineon Si CoolMOS MOSFET (IPW60R045CP), GaN Systems GaN HEMT (GS66516T) and MASTERGAN1 AlGaN/GaN 2-in-1 HEMTs were used to design heatsinks for the power switching modules for each device. The heatsink structures were designed in Boyd Corp's online tool, AAVID, using their commercially available heatsinks models [27].

The 3D models were iteratively simulated for different heights to find the minimum size of heatsinks that could reduce the maximum temperature of the switching module down to 100 ˚C without requiring any forced air convective cooling [27]. Figures 52, 53 and 54 show the temperature profile of the Si, GaN and AlGaN/GaN models with the heatsinks hidden while figures 55, 56 and 57 show the temperature profiles for the Si, GaN and AlGaN/GaN models with the heatsinks made visible [27]. The temperatures displayed on the legends are in ˚C [27]. The temperature profiles for the three models with the heatsink not visible show that the highest of temperatures are concentrated around the switching devices that have the highest power losses [27]. As the heat losses for all Si MOSFETs are close to 20 W, the temperatures are fairly uniform throughout the Si MOSFET module structure whereas for the GaN model the temperatures are higher at

the right end near the HEMTs with higher losses while the left end with lower losses have lower temperatures [27].

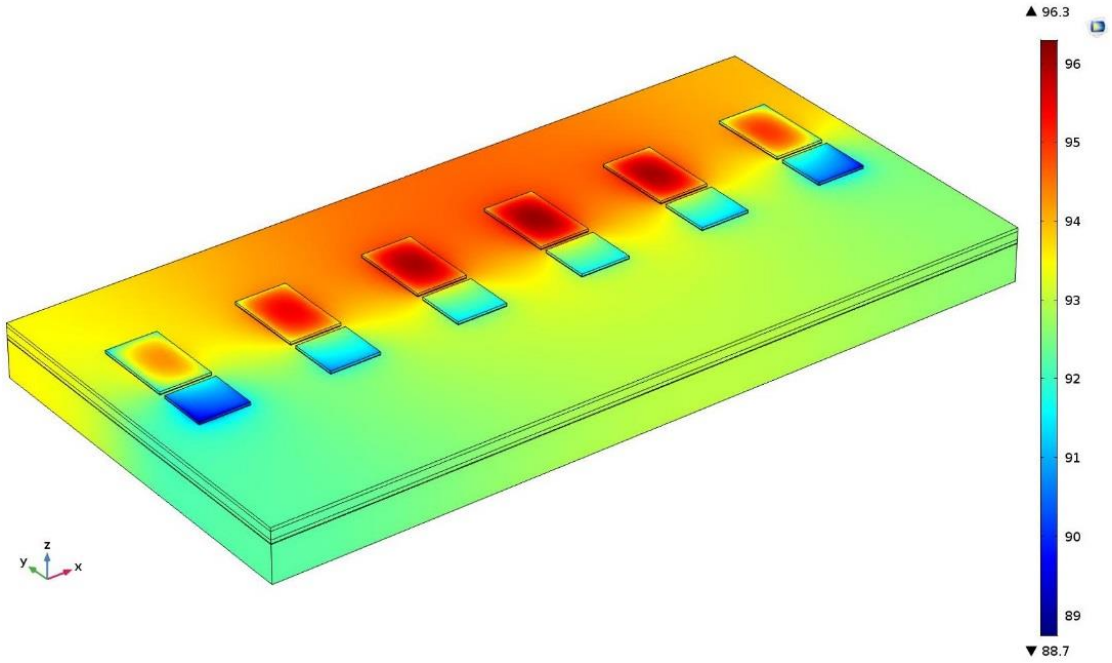

Figure 52. Temperature profile of Si model with heatsink not visible.

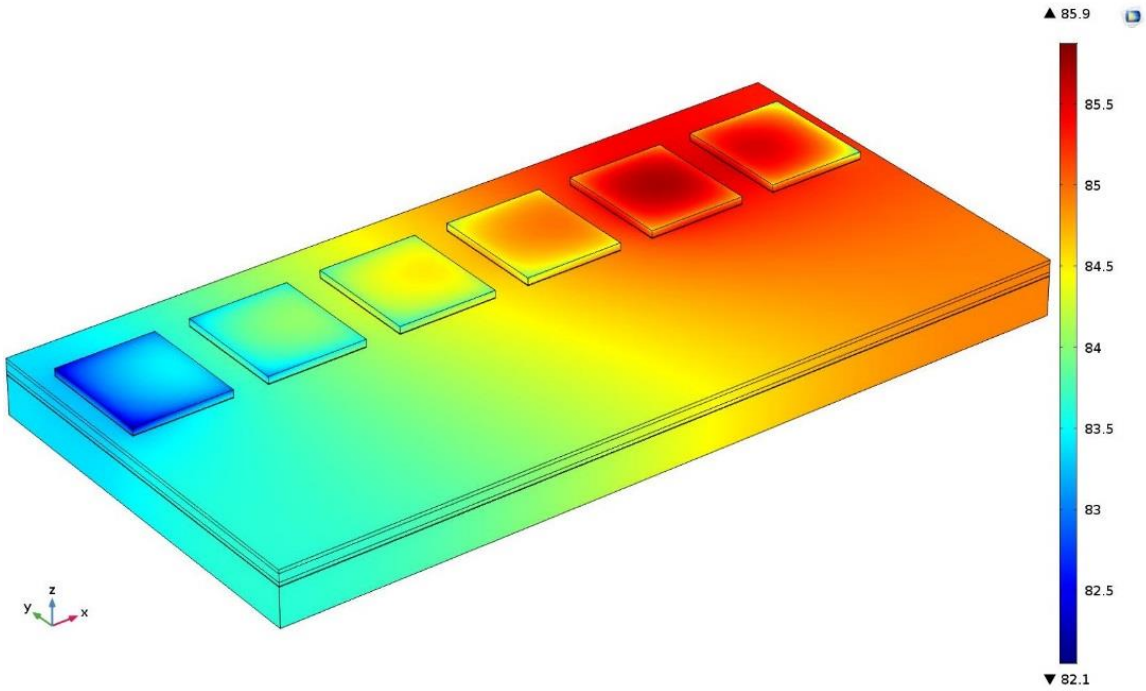

Figure 53. Temperature profile of GaN model with heatsink not visible.

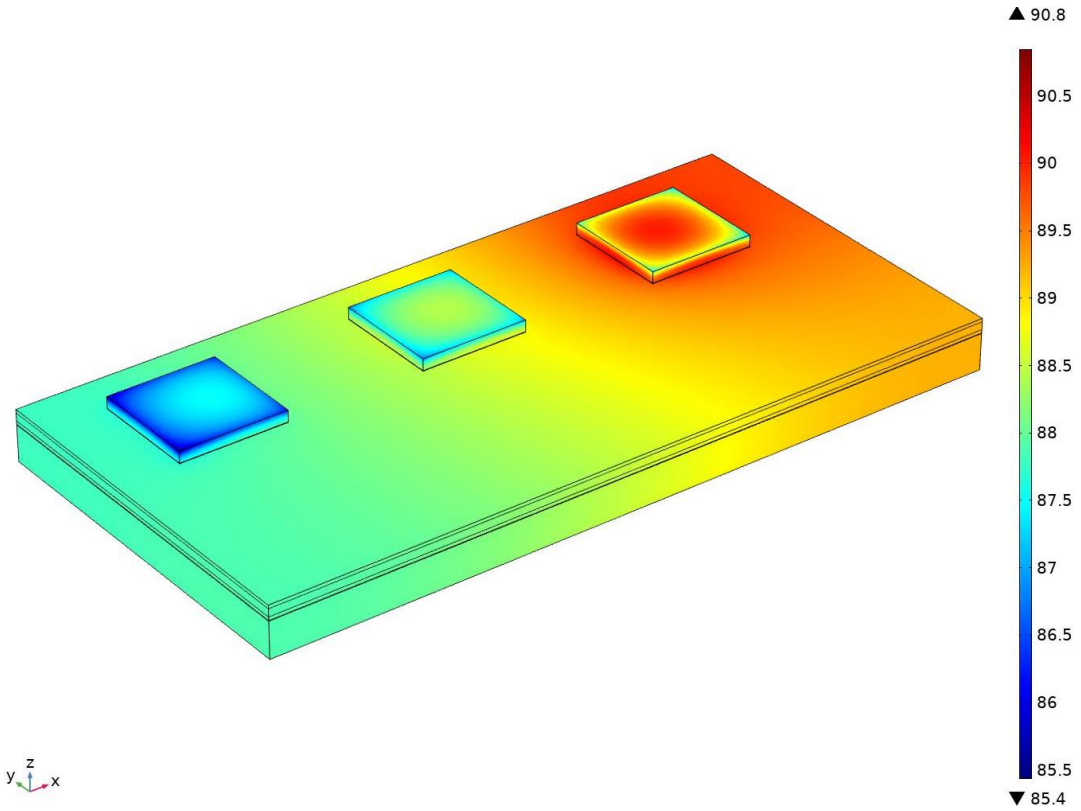

Figure 54. Temperature profile of AlGaN/GaN model with heatsink not visible.

The temperature range for the GaN model is within 4 ˚C which is smaller than for Si. This is because the power losses for the MOSFETs have a wider range as compared to the GaN model [27]. For the AlGaN/GaN model, the temperature range is within 5 ˚C as compared to Si in terms of maximum and minimum temperatures.

The temperature profiles for the two models with the heatsink visible also show similar distribution of temperatures [27]. The Si, GaN and AlGaN/GaN models have higher temperatures on the heatsink uniformly around all the switching devices but the range of temperatures for the heatsinks are much lower in the GaN and AlGaN/GaN models than the Si model [27].

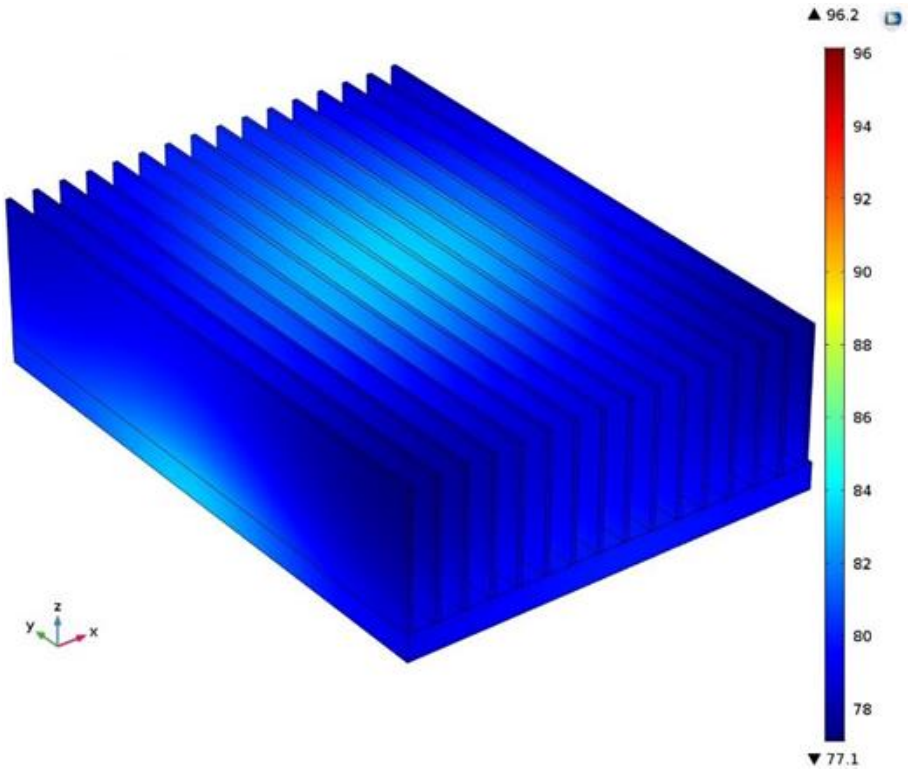

Figure 55. Temperature profile of Si model with heatsink visible.

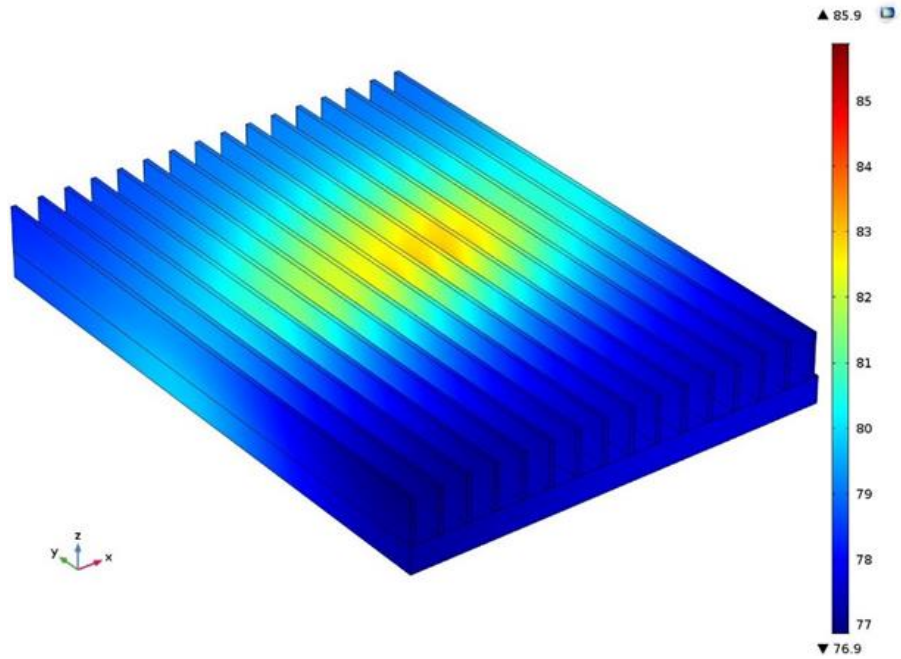

Figure 56. Temperature profile of GaN model with heatsink visible.

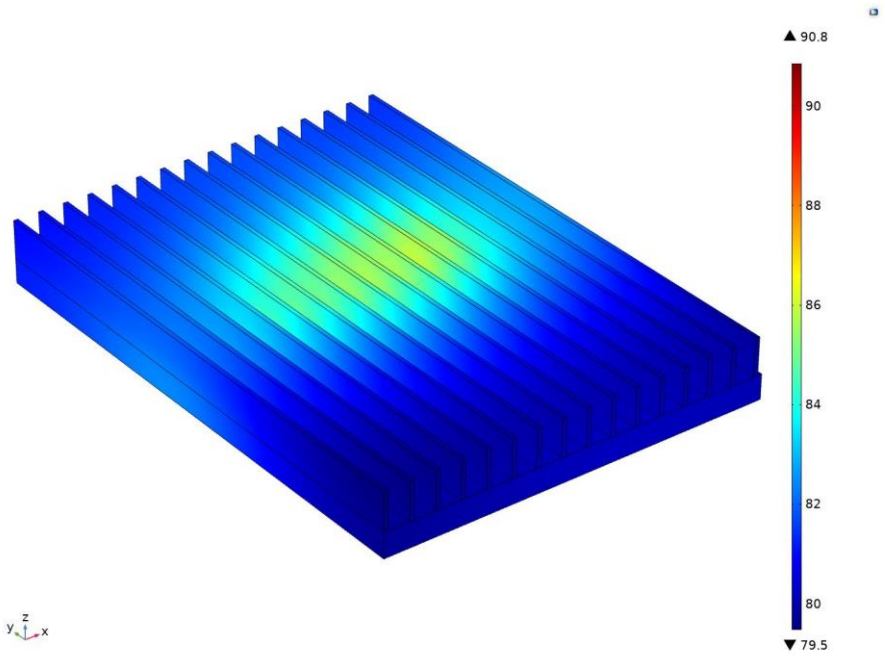

Figure 57. Temperature profile of AlGaN/GaN model with heatsink visible.

The maximum temperatures for the Si, GaN and AlGaN/GaN models were found to be 96.36 ˚C, 85.91 ˚C and 90.91 ˚C respectively [27]. The minimum temperatures were 77.14 ˚C, 76.87 ˚C and 79.47 ˚C for the Si, GaN and AlGaN/GaN models respectively [27]. The 3D model for Si MOSFETs had a volume of 183.8 cm^3, the GaN model had a heatsink volume of 125.6 cm^3 while the AlGaN/GaN model's heatsink had a volume of 123.34 cm^3. From the simulations for the two models, it is clear that both the WBG material modules required a smaller heatsink in terms of volume. The GaN module required a heatsink 1.46 times smaller while the AlGaN/GaN module required a heatsink 1.49 times smaller than the Si model for maximum temperatures within 5 ˚C of each other.

5. Conclusions and Future Work

5.1 Conclusions

Although typically large voltage values of operation for power devices were not simulated, it was shown that even at the relatively low gate and drain voltages of 20 V and 55 V respectively, the temperatures in the WBG materials were significantly lower as compared to Si for both high and lower dopant concentration levels. For lower dopant concentration levels, AlGaN also showed similar advantages in terms of lower average and maximum temperatures as compared to Si, with GaN performing better than Si but not as good as AlGaN. In summary, the models developed in COMSOL Multiphysics successfully demonstrated the superiority of the WBG materials SiC, GaN and AlGaN in terms of thermal performance for power switching device structures.

The use of GaN and AlGaN/GaN HEMTs of specifications similar to Si MOSFETs yielded significantly better power loss performance for a modified H5 inverter topology which also increased the system efficiency, as simulated in PSIM. The results of these power loss values were used in COMSOL to verify and quantify the reduction in heatsink size when replacing Si MOSFETs with GaN and AlGaN/GaN HEMTs of similar specifications.

In general, SiC, with its relatively better material properties and more mature market performed better in terms of temperatures for the VDMOSFET simulations while the AlGaN/GaN devices performing slightly better than their GaN counterparts. For the

heatsink simulations, the GaN devices HEMTs performed slightly better than the AlGaN/GaN HEMTs. The main reason for the similarities between the results from the GaN and AlGaN/GaN simulations for both the VDMOSFETs and heatsinks comes from the fact that the material properties of AlGaN depends on the molar fraction of Al and Ga present in the alloy. $Al_{0.15}Ga_{0.85}N$ has properties much closer to GaN than AlN since it only contains 15% molar fraction of Al and since $Al_{0.15}Ga_{0.85}N$ was used for all the simulations, the results are very similar to the ones for GaN. AlGaN is a major component of GaN HEMTs but power devices made of AlGaN are not available commercially. This results of this research shows that AlGaN can be a viable material for power switching devices with similar performance to GaN.

5.2 Future work

The following points are recommended for future work to study the merits of WBG and UWBG materials:

- $Al_{0.15}Ga_{0.85}N$ was tested for the purposes of this research. However, the properties of AlGaN depend on the content of Al and Ga in the alloy with the material properties leaning towards AlN as the molar content of Al in the alloy increases. As more material properties of AlGaN with different Al contents become available/studied, these AlGaN alloys can be tested to compare their performance in the VDMOSFET models.

- Switches made of AlN are not commercially available and AlN power devices have only recently been investigated. AlN can also be tested in the VDMOSFET model for its thermal performance.
- WBG power switches can be tested in other inverter topologies to test out their power loss advantages and heatsink requirements.

6. List of Publications

Journal Articles:

[1] **M. Manandhar**, M. Matin, " Comparative Modelling and Thermal Analysis of AlGaN/GaN power devices, " (Submitted and under review).

[2] **M. Manandhar**, M. Matin, “Electrical performance of AlGaN/GaN and AlGaS/GaS HEMT structures, " (Manuscript under completion).

[3] K. Alatawi, F. Almasoudi, **M. Manandhar** and M. Matin, "Comparative Analysis of Si- and GaN-Based Single-Phase Transformer-Less PV Grid-Tied Inverter," Electronics, vol. 7, no. 3, p. 34, 2018.

[4] F. Almasoudi, K. Alatawi, **M. Manandhar** and M. Matin, "Simulation and Performance Comparison of Si and SiC Based on a Proposed H6 Inverter for PV Grid-tied Applications," 2018.

Conference Proceedings:

[1] **M. B. Manandhar** and M. A. Matin, "Thermal Modeling of Wide Bandgap Materials for Power MOSFETs," in Wide Bandgap Power Devices and Applications, vol. 9957, San Diego, 2016.

[2] **M. B. Manandhar** and M. A. Matin, "3D analysis of thermal and electrical performance of wide bandgap VDMOSFETs," in Wide Bandgap Power Devices and Applications II, San Diego, 2017.

[3] **M. B. Manandhar**, K. Alatawi, F. Almasoudi and M. A. Matin, "Comparative study of Heatsink materials for Gallium Nitride HEMT modules using thermal modelling," in Wide Bandgap Power and Energy Devices and Applications III, San Diego, 2018.

7. References

[1] J. Millán, P. Godignon and A. Pérez-Tomás, "Wide Band Gap Semiconductor Devices for Power Electronics," *Automatika*, vol. 53, no. 2, pp. 107-116, 2012.

[2] J. Millán, "A review of WBG power semiconductor devices," in *CAS 2012 (International Semiconductor Conference)*, Sinaia, 2012.

[3] B. Ozpineci, L. M. Tolbert, S. K. Islam and M. Chinthavali, "Comparision of wide band gap semiconductors for power electronics applications," in *10th European Conference on Power Electronics and Applications*, Toulouse, 2003.

[4] N. Kaminski, "State of the Art and the Future of Wide Band-Gap Devices," in *13th European Conference on Power Electronics and Applications*, Barcelona, 2009.

[5] J. Casady and R. Johnson, "Status of silicon carbide (SiC) as a wide-bandgap semiconductor for high-temperature applications: A review," *Solid-State Electronics*, vol. 39, no. 10, pp. 1409-1422, October 1996.

[6] COMSOL Multiphysics, "Multiphysics Simulation of Power Electronics," COMSOL Multiphysics, 2015.

[7] H. Jain, S. Rajawat and P. Agrawal, "Comparision of wide band gap semiconductors for power electronics applications," in *2008 International Conference on Recent Advances in Microwave Theory and Applications*, Jaipur, 2008.

[8] P. Alexakis, O. Alatise, J. Hu, S. Jahdi, L. Ran and P. A. Mawby, "Improved Electrothermal Ruggedness in SiC MOSFETs Compared With Silicon IGBTs," *IEEE Transactions on Electron Devices*, vol. 61, no. 7, pp. 2278 - 2286, 2014.

[9] B. K. Bose, "Evaluation of modern power semiconductor devices and future trends of converters," *IEEE Transactions on Industry Applications*, vol. 28, no. 2, pp. 403-413, 1992.

[10] M. Mataray, "Modern Power Semiconductor Devices (A Review)," *International Journal of Computer Science & Information Technologies*, vol. 3, no. 4, pp. 4571-4574, 2012.

[11] B. K. Bose, "Recent advances in power electronics," *IEEE Transactions on Power Electronics*, vol. 7, no. 1, pp. 2-16, 1992.

[12] K. Tokunaga, *Development, fabrication, and characterization of a vertical-diffused MOS process for power RF applications*, Rochester, New York, 2008.

[13] S. C. Sun and J. D. Plummer, "Modeling of the on-resistance of LDMOS,

VDMOS, and VMOS power transistors," *IEEE Transactions on Electron Devices,* vol. 27, no. 2, pp. 256-267, 1980.

[14] B. J. Baliga, "Vertical-Diffused MOSFETs," in *Silicon RF Power MOSFETs*, Singapore, World Scientific Publishing Co. Pte. Ltd., 2005, pp. 103-126.

[15] R. Vaid, N. Padha, A. Kumar, R. Gupta and C. D. Parikh, "Modeling power VDMOSFET transistors: Device physics and equivalent circuit model with parameter extraction," *Indian Journal of Pure and Applied Physics*, vol. 42, no. 10, pp. 775-782, 1 October 2004.

[16] M. B. Manandhar and M. A. Matin, "Thermal Modeling of Wide Bandgap Materials for Power MOSFETs," in *Wide Bandgap Power Devices and Applications*, San Diego, 2016.

[17] M. B. Manandhar and M. A. Matin, "3D analysis of thermal and electrical performance of wide bandgap VDMOSFETs," in *Wide Bandgap Power Devices and Applications II*, San Diego, 2017.

[18] J. Hu, O. Alatise, J. A. Ortiz-Gonzalez, P. Alexakis, L. Ran and P. Mawby, "Finite Element Modelling and Experimental Characterisation of Paralleled SiC MOSFET Failure under Avalanche Mode Conduction," in *17th European Conference on Power Electronics and Applications (EPE'15 ECCE-Europe)*, Geneva, 2015.

[19] J. Zarebski, "The compact d.c. electrothermal model of power MOSFETs," *International Journal of Numerical Modelling: Electronic Networks, Devices and Fields,* vol. 23, no. 2, pp. 140-150, 2009.

[20] B. N. Pushpakaran, S. B. Bayne and A. A. Ogunniyi, "Electro-Thermal Transient Simulation of Silicon Carbide Power Mosfet," in *2013 Abstracts IEEE International Conference on Plasma Science (ICOPS)*, San Francisco, 2013.

[21] S. A. Khan, Y. Guo and J. Zhu, "A High Efficiency Transformerless PV Grid-Connected Inverter with Leakage Current Suppression," in *9th International Conference on Electrical and Computer Engineering*, Dhaka, 2016.

[22] P. Kakosimos, A. Sarigiannidis, M. Beniakar and A. Kladas, "Investigation of transformerless topologies for renewable energy applications eliminating leakage currents," in *MedPower 2014*, Athens, 2014.

[23] H. Xiao and S. Xie, "Leakage Current Analytical Model and Application in Single-Phase Transformerless Photovoltaic Grid-Connected Inverter," *IEEE Transactions on Electromagnetic Compatibility,* vol. 52, no. 4, pp. 902 - 913, 2010.

[24] L. Wang, Y. Shi, Y. Shi, R. Xie and H. Li, "Ground leakage current suppression in a 50 kW 5-level T-type transformerless PV inverter," in *2016 IEEE Energy Conversion Congress and Exposition (ECCE)*, Milwaukee, 2016.

[25] B. Cole and S. Parke, "A Method to Overcome Self-Heating Effects in SOI MOSFETs," in *Proceedings of the 15th Biennial University/Government/Industry Microelectronics Symposium, 2003.*, Boise,

2003.

[26] F. Almasoudi, K. Alatawi, M. Manandhar and M. Matin, "Simulation and Performance Comparison of Si and SiC Based on a Proposed H6 Inverter for PV Grid-tied Applications," 2018.

[27] K. Alatawi, F. Almasoudi, M. Manandhar and M. Matin, "Comparative Analysis of Si- and GaN-Based Single-Phase Transformer-Less PV Grid-Tied Inverter," *Electronics,* vol. 7, no. 3, p. 34, 2018.

[28] J. Y. Tsao, S. Chowdhury, M. A. Hollis, D. Jena, N. M. Johnson, K. A. Jones, R. J. Kaplar, S. Rajan, C. G. Van de Walle, E. Bellotti, C. L. Chua, R. Collazo, M. E. Coltrin, J. A. Cooper, K. R. Evans, S. Graham, T. A. Grotjohn and E. Heller, "Ultrawide-Bandgap Semiconductors: Research Opportunities and Challenges," *Advanced Electronic Materials,* vol. 4, no. 1, 2018.

[29] R. Kaplar, A. A. Allerman, A. M. Armstrong, M. H. Crawford, J. R. Dickerson, A. J. Fischer, A. G. Baca and E. A. Douglas, "Review—Ultra-Wide-Bandgap AlGaN Power Electronic Devices," *ECS Journal of Solid State Science and Technology,* vol. 6, no. 2, 2016.

[30] J. S. Lundh, B. Chatterjee, Y. Song, A. G. Baca, R. J. Kaplar, T. E. Beechem, A. A. Allerman, A. M. Armstrong, B. A. Klein, A. Bansal, D. Talreja, A. Pogrebnyakov and E. Heller, "Multidimensional thermal analysis of an ultrawide bandgap AlGaN channel high electron mobility transistor," *Applied Physics Letters,* vol. 115, no. 15, 2019.

[31] Semiconductor Industry Association, "2020 State of the U.S. Semiconductor Industry," Semiconductor Industry Association, Washington, D.C., 2020.

[32] B. J. Baliga, Fundamentals of Power Semiconductor Devices, New York: Springer, 2008.

[33] J. Lutz, H. Schlangenotto, U. Scheuermann and R. De Doncker, Semiconductor Power Devices Physics, Characteristics, Reliablility, Berlin: Springer, 2011.

[34] J. L. Hudgins, "A review of modern power semiconductor devices," *Microelectronics Journal,* vol. 24, no. 1-2, pp. 41-54, 1993.

[35] I. N. Jiya and R. Gouws, "Overview of Power Electronic Switches: A Summary of the Past, State-of-the-Art and Illumination of the Future," *Micromachines* , vol. 11, no. 12, pp. 1-29, 2020.

[36] I. Batarseh and A. Harb, Power Electronics Circuit Analysis and Design, Cham: Springer, 2018.

[37] R. S. Pengelly, S. M. Wood, J. W. Milligan, S. T. Sheppard and W. L. Pribble, "A Review of GaN on SiC High Electron-Mobility Power Transistors and MMICs," *IEEE Transactions on Microwave Theory and Techniques,* vol. 60, no. 6, pp. 1764-1783, 2012.

[38] F. Zeng, J. X. An, G. Zhou, W. Li, H. Wang, T. Duan, L. Jiang and H. Yu, "A Comprehensive Review of Recent Progress on GaN High Electron Mobility

Transistors: Devices, Fabrication and Reliability," *Electronics,* vol. 7, no. 12, pp. 1-20, 2018.

[39] U. K. Mishra, P. Parikh and Y.-F. Wu, "AlGaN/GaN HEMTs-an overview of device operation and application," *Proceedings of the IEEE,* vol. 90, no. 6, pp. 1022-1031, 2002.

[40] A. S. Augustine Fletcher, D. Nirmal, J. J. Ajayan and L. Arivazhagan, "Analysis of AlGaN/GaN HEMT using discrete field plate technique for high power and high frequency applications," *AEU - International Journal of Electronics and Communications,* vol. 99, pp. 325-330, 2019.

[41] B. J. Baliga, "Lateral-Diffused MOSFETs," in *Silicon RF Power MOSFETs*, Singapore, World Scientific Publishing Co. Pte. Ltd., 2005, pp. 71-102.

[42] T. Sakai and N. Murakami, "A New VDMOSFET Structure with Reduced Reverse Transfer Capacitance," *IEEE Transactions on Electron Devices,* vol. 36, no. 7, pp. 1381-1386, 1989.

[43] N. Stojadinovic, I. Manic, V. Davidovic, D. Dankovic, S. Djoric-Veljkovic, S. Golubovic and S. Dimitrijev, "Effects of electrical stressing in power VDMOSFETs," in *IEEE Conference on Electron Devices and Solid-State Circuits*, Hong Kong, 2005.

[44] N. Nenadovic, V. Cuoco, S. Theeuwen, H. Schellevis, G. Spierings, A. Griffo, M. Pelk, L. Nanver, R. Jos and J. Slotboom, "RF Power Silicon-On-Glass VDMOSFETs," *IEEE Electron Device Letters* , vol. 25, no. 6, pp. 424-426, 2004.

[45] S. Yuan, Q. Zhang, Y. Liu and Y. Zhang, "4H-SiC and Si Based IGBTs/VDMOSFETs Characters Comparison," in *Symposium on Photonics and Optoelectronics*, Shanghai, 2012.

[46] Y. J. He, H. L. Lv, X. Y. Tang, Q. W. Song, Y. M. Zhang, C. Han, Y. M. Zhang and Y. M. Zhang, "Experimental study on the 4H-SiC-based VDMOSFETs with lightly doped P-well field-limiting rings termination," *Solid-state electronics,* vol. 129, no. 03, pp. 175-181, 2017.

[47] C.-Y. Chen, Y.-K. Lai, K.-Y. Lee, C.-F. Huang and S.-Y. Huang, "Investigation of 3.3 kV 4H-SiC DC-FSJ MOSFET Structures," *Micromachines*, vol. 12, no. 7, pp. 1-9, 2021.

[48] J. A. Z. Flores, *Device Characterization and Modeling of Large-Size GaN HEMTs,* Kassel: Kassel University Press GmbH, 2012.

[49] R. Garcia Perez, *AlGaN/GaN HEMT by Magnetron Sputtering System,* Ann Arbor: ProQuest Dissertations Publishing, 2017.

[50] S. Jeyabal and P. Vimala, "High electron mobility transistor-a review on analytical models," *International Journal for Innovative Research in Science & Technology,* vol. 3, no. 5, pp. 103-114, 2016.

[51] S. Tiku and D. Biswas, *III-V Integrated Circuit Fabrication Technology:*

Fabrication, Integration and Applications, Singapore: Jenny Stanford Publishing, 2016.

[52] R. Szweda, "HEMT materials and devices," *III-Vs Review,* vol. 16, no. 3, pp. 36-39, 2003.

[53] P. Luo, *GaN HEMT modeling including trapping effects based on Chalmers model and pulsed S-parameter measurements,* Göttingen: Cuvillier Verlag, 2018.

[54] C.-T. Ma and Z.-H. Gu, "Review of GaN HEMT Applications in Power Converters over 500 W," *Electronics,* vol. 8, no. 12, pp. 1-29, 2019.

[55] W. Wojtasiak, M. Góralczyk, D. Gryglewski, M. Zając, R. Kucharski, P. Prystawko, A. Piotrowska, M. Ekielski, E. Kamińska, A. Taube and M. Wzorek, "AlGaN/GaN High Electron Mobility Transistors on Semi-Insulating Ammono-GaN Substrates with Regrown Ohmic Contacts," *Micromachines,* vol. 9, no. 11, pp. 1-14, 2018.

[56] D. Dumka, T. Chou, J. Jimenez, D. Fanning, D. Francis, F. Faili, F. Ejeckam, M. Bernardoni, J. Pomeroy and M. Kuball, "Electrical and Thermal Performance of AlGaN/GaN HEMTs on Diamond Substrate for RF Applications," in *IEEE Compound Semiconductor Integrated Circuit Symposium (CSICS)*, Monterey, 2013.

[57] P. H. Carey, S. J. Pearton, F. Ren, A. G. Baca, B. A. Klein, A. A. Allerman, A. M. Armstrong, E. A. Douglas, R. J. Kaplar and P. G. Kotula, "Operation Up to 500 °C of Al0.85Ga0.15N/Al0.7Ga0.3N High Electron Mobility Transistors," *IEEE Journal of the Electron Devices Society,* vol. 7, pp. 444-452, 2019.

[58] M. Wośko, B. Paszkiewicz, T. Szymański and R. Paszkiewicz, "Comparison of electrical, optical and structural properties of epitaxially grown HEMT's type AlGaN/AlN/GaN heterostructures on Al2O3, Si and SiC substrates," *Superlattices and Microstructures,* vol. 100, pp. 619-626, 2016.

[59] A. G. Baca, A. M. Armstrong, A. A. Allerman, E. A. Douglas, C. A. Sanchez, M. P. King, M. E. Coltrin, C. D. Nordquist, T. R. Fortune and R. J. Kaplar, "An AlN/Al0.85Ga0.15N high electron mobility transistor with a regrown ohmic contact," in *74th Annual Device Research Conference (DRC)*, Newark, 2016.

[60] H. Okumura, "A roadmap for future wide bandgap semiconductor power electronics," *MRS Bulletin, suppl. Power Electronics with Wide Bandgap Materials,* vol. 40, no. 5, pp. 439-444, 2015.

[61] R. Davis, Z. Sitar, B. Williams, H. Kong, H. Kim, J. Palmour, J. Edmond, J. Ryu, J. Glass and C. Carter, "Critical evaluation of the status of the areas for future research regarding the wide band gap semiconductors diamond, gallium nitride and silicon carbide," *Materials Science and Engineering: B,* vol. 1, no. 1, pp. 77-104, 1988.

[62] K. Takahashi, A. Yoshikawa and A. Sandhu, Wide bandgap semiconductors: fundamental properties and modern photonic and electronic devices, Berlin: Springer, 2007.

[63] A. Matallana, E. Ibarra, I. López, J. Andreu, J. Garate, X. Jordà and J. Rebollo, "Power module electronics in HEV/EV applications: New trends in widebandgap semiconductor technologies and design aspects," *Renewable and Sustainable Energy Reviews,* vol. 113, pp. 1-33, 2019.

[64] K. Shenai, "Manufacturing Challenges in Wide Band Gap (WBG) Power Electronics," *ECS Transactions,* vol. 58, no. 4, pp. 301-310, 2013.

[65] J. Hudgins, G. Simin, E. Santi and M. Khan, "An assessment of wide bandgap semiconductors for power devices," *IEEE Transactions on Power Electronics,* vol. 18, no. 3, pp. 907-914, 2003.

[66] L. F. S. Alves, P. Lefranc, P.-O. Jeannin and B. Sarrazin, "Review on SiC-MOSFET Devices and Associated Gate Drivers," in *IEEE International Conference on Industrial Technology (ICIT)*, Lyon, 2018.

[67] S. Fujita, "Wide-bandgap semiconductor materials: For their full bloom," *Japanese Journal of Applied Physics,* vol. 54, no. 3, pp. 1-12, 2015.

[68] H. Lee, V. Smet and R. Tummala, "A Review of SiC Power Module Packaging Technologies: Challenges, Advances, and Emerging Issues," *IEEE Journal of Emerging and Selected Topics in Power Electronics,* vol. 8, no. 1, pp. 239-255, 2020.

[69] L. Han, L. Liang, Y. Kang and Y. Qiu, "A Review of SiC IGBT: Models, Fabrications, Characteristics, and Applications," *IEEE Transactions on Power Electronics*, vol. 36, no. 2, pp. 2080-2093, 2020.

[70] P. Gammon, "Silicon and the wide bandgap semiconductors, shaping the future power electronic device market," in *14th International Conference on Ultimate Integration on Silicon (ULIS)*, Coventry, 2013.

[71] L. Han, L. Liang, Y. Kang and Y. Qiu, "A Review of SiC IGBT: Models, Fabrications, Characteristics, and Applications," *IEEE Transactions on Power Electronic*, vol. 36, no. 2, pp. 2080-2093, 2020.

[72] N. G. Wright and A. B. Horsfall, "SiC sensors: a review," *Journal of Physics D: Applied Physics,* vol. 40, no. 20, pp. 6345-6354, 2007.

[73] T. J. Flack, B. N. Pushpakaran and S. B. Bayne, "GaN Technology for Power Electronic Applications: A Review," *Journal of Electronic Materials,* vol. 45, no. 6, pp. 2673-2682, 2016.

[74] E. A. Jones, F. F. Wang and D. Costinett, "Review of Commercial GaN Power Devices and GaN-Based Converter Design Challenges," *IEEE journal of emerging and selected topics in power electronics,* vol. 4, no. 3, pp. 707-719, 2016.

[75] E. A. Jones, F. Wang and B. Ozpineci, "Application-Based Review of GaN HFETs," in *IEEE Workshop on Wide Bandgap Power Devices and Applications*, Knoxville, 2014.

[76] B. N. Pushpakaran, A. S. Subburaj and S. B. Bayne, "Commercial GaN-Based

Power Electronic Systems: A Review," *Journal of electronic materials*, vol. 49, no. 11, pp. 6247-6262, 2020.

[77] P. Kung and M. Razeghi, "III-Nitride wide bandgap semiconductors: A survey of the current status and future trends of the material and device technology," *Opto-electronics Review*, vol. 8, no. 3, pp. 201-239, 2000.

[78] T. Kozawa, T. Mori, T. Ohwaki, Y. Taga and N. Sawaki, "UV Photoemission Study of AlGaN Grown by Metalorganic Vapor Phase Epitaxy," *Japanese Journal of Applied Physics*, vol. 39, no. 2, pp. L772-L774, 2000.

[79] H. Wang, D. Wei, J. Duan, Z. Qin, G. Qin, Y. Yao and M. Hu, "The exceptionally high thermal conductivity after 'alloying' two-dimensional gallium nitride (GaN) and aluminum nitride (AlN)," *Nanotechnology*, vol. 32, no. 13, pp. 135401-135412, 2021.

[80] S. M. Thahab, H. Abu Hassan and Z. Hassan, "Al0.15Ga0.85N/GaN Heterostructure Field Effect Transistors (HFET)Device Structure Optimization And Thermal Effects," in *Malaysia-Japan International Symposium On Advanced Technology*, Kuala Lumpur, 2007.

[81] A. Lundskog, *Characterization of advanced AlGaN HEMT structures*, Linköping: Linköping University, 2007.

[82] S. Dagli, K. A. Mengle and E. Kioupakis, "Thermal conductivity of AlN, GaN, and AlxGa1−xN alloys as a function of composition, temperature, crystallographic direction, and isotope disorder from first principles," *Material Science*, pp. 1-16, 2019.

[83] W. Liu and A. A. Balandin, "Thermal conduction in AlxGa1−xN alloys and thin films," *Journal of Applied Physics*, vol. 97, no. 7, p. 73710, 2005.

[84] E. Mitani, M. Aojima, Maekawa, Arata and S. Sano, "An 800-W AlGaN/GaN HEMT for S-band High-Power Application," in *International Conference on Compound Semiconductor Manufacturing Technology*, Austin, 2007.

[85] C.-T. Chang, S.-K. Hsiao, E. Chang, C.-Y. Lu, J.-C. Huang and C.-T. Lee, "Changes of Electrical Characteristics for AlGaN/GaN HEMTs Under Uniaxial Tensile Strain," *IEEE Electron Device Letters*, vol. 30, no. 3, pp. 213-215, 2009.

[86] Y. Nagasawa and H. Hirano, "A Review of AlGaN-Based Deep-Ultraviolet Light-Emitting Diodes on Sapphire," *Applied Sciences*, vol. 8, no. 8, pp. 1-36, 2018.

[87] A. Sztein, J. Haberstroh, J. E. Bowers, S. P. DenBaars and S. Nakamura, "Calculated thermoelectric properties of InxGa1−xN, InxAl1−xN, and AlxGa1−xN," *Journal of Applied Physics*, vol. 113, no. 18, p. 183707, 2013.

[88] T. Palacios, F. Calle, J. Grajal, E. Monroy, M. Eickhoff, O. Ambacher and F. Omnes, "High frequency SAW devices on AlGaN: fabrication, characterization and integration with optoelectronics," in *IEEE Ultrasonics Symposium*, Munich, 2002.

[89] M. Noman H. Khan, M. Forouzesh, Y. P. Siwakoti, L. Li, T. Kerekes and F. Blaabjerg, "Transformerless Inverter Topologies for Single-Phase Photovoltaic Systems: A Comparative Review," *IEEE Journal of Emerging and Selected Topics in Power Electronics,* vol. 8, no. 1, pp. 805 - 835, 2019.

[90] J. Jana, H. Saha and K. Das Bhattacharya, "A review of inverter topologies for single-phase grid-connected photovoltaic systems," *Renewable and Sustainable Energy Reviews,* vol. 72, pp. 1256-1270, 2017.

[91] M. Shayestegan, M. Shakeri, H. Abunima, S. S. Reza, M. Akhtaruzzaman, B. Bais, S. Mat, K. Sopian and N. Amin, "An overview on prospects of new generation single-phase transformerless inverters for grid-connected photovoltaic (PV) systems," *Renewable and Sustainable Energy Reviews,* vol. 82, no. 1, pp. 515-530, 2018.

[92] A. Saha, S. Ahmad, S. Mekhilef, U. K. Jhuma, H. Islam, Z. A. Chowdhury and M. Islam, "Comparative Study of Different Transformer-less Inverter Topologies for Grid-tied Photovoltaic System," in *5th International Conference on Advances in Electrical Engineering (ICAEE),* Dhaka, 2019.

[93] M. Islam, S. Mekhilef and M. Hasan, "Single phase transformerless inverter topologies for grid-tied photovoltaic system: A review," *Renewable and Sustainable Energy Reviews,* vol. 45, pp. 69-86, 2015.

[94] H. Albalawi and S. A. Zaid, "An H5 Transformerless Inverter for Grid Connected PV Systems with Improved Utilization Factor and a Simple Maximum Power Point Algorithm," *Energies,* vol. 11, no. 11, pp. 1 - 17, 2018.

[95] F. Almasoudi and M. Matin, "An Improved Proposed Single Phase Transformerless Inverter with Leakage Current Elimination and Reactive Power Capability for PV Systems Application," *Journal of Low Power Electronics and Applications,* vol. 11, no. 1, pp. 1-15, 2018.

[96] H. Xiao and S. Xie, "Leakage Current Analytical Model and Application in Single-Phase Transformerless Photovoltaic Grid-Connected Inverter," *IEEE Transactions on Electromagnetic Compatibility,* vol. 52, no. 4, pp. 902-913, 2010.

[97] S. Chakraborty, M. M. Hasan and M. Abdur Razzak, "Transformer-less single-phase grid-tie photovoltaic inverter topologies for residential application with various filter circuits," *Renewable and Sustainable Energy Reviews,* vol. 72, pp. 1152-1166, 2017.

[98] G. El-Menofy, A. F. Abdou, H. Z. Azazi, E. E. El-Kholy and A. El-hefnawy, "An Overview on Single-phase Transformerless inverter topologies for Grid-tied PV system," in *Proceedings of 4th International Conference on Energy Engineering,* Aswan, 2017.

[99] P. Kakosimos, A. Sarigiannidis, M. Beniakar and A. Kladas, "Investigation of transformerless topologies for renewable energy applications eliminating leakage currents," in *MedPower 2014,* Athens, 2014.

[100] G. Rizzoli, M. Mengoni, L. Zarri, A. Tani, G. Serra and D. Casadei, "Comparison of single-phase H4, H5, H6 inverters for transformerless photovoltaic applications," in *IECON 2016 - 42nd Annual Conference of the IEEE Industrial Electronics Society*, Florence, 2016.

[101] M. A. Khan, A. Haque and V. B. Kurukuru, "Performance assessment of stand-alone transformerless inverters," *International Transactions on Electrical Energy Systems*, vol. 30, pp. 1-21, 2019.

[102] COMSOL Multiphysics, "COMSOL Multiphysics User's Guide," Palo Alto, 2012.

[103] D. V. Hutton, Fundamentals of Finite Element Analysis, 1st Edition ed., New York: Mcgraw-Hill, 2004.

[104] E. Madenci and I. Guven, Finite Element Method and Applications in Engineering Using ANSYS, New York: Springer, 2007.

[105] D. G. Pavlou, Essentials of the Finite Element Method: For Mechanical and Structural Engineers, London: Elsevier, 2015.

[106] M. B. Manandhar, *Thermal and Structural Modeling of Electrochromics On Glass*, Denver: University of Denver, 2014.

[107] M. B. Manandhar, K. Alatawi, F. Almasoudi and M. A. Matin, "Comparative study of Heatsink materials for Gallium Nitride HEMT modules using thermal modelling," in *Wide Bandgap Power and Energy Devices and Applications III.*, San Diego, 2018.

[108] M. Akbari, A. S. Bahman, P. D. Reigosa, L. Ceccarelli, F. Iannuzzo and M. Tavakoli, "Non-uniform Temperature Distribution Implications on Thermal Analysis Accuracy of Si IGBTs and SiC MOSFETs," in *24rd International Workshop on Thermal Investigations of ICs and Systems (THERMINIC)*, Stockholm, 2018.

[109] J. Naghibi, K. Mehran and M. P. Foster, "An Online Failure Assessment Approach for SiC-based MOSFET Power Modules Using Iterative Condition Monitoring Technique," in *IEEE 21st Workshop on Control and Modeling for Power Electronics (COMPEL)*, Aalborg, 2020.

[110] K. R. Bagnall, *Device-level Thermal Analysis of GaN-based Electronics*, Cambridge: Massachusetts Institute of Technology, 2013.

[111] Y. Li, S. Mao, Y. Fu, R. Xu, B. Yan, Y. Zhang and Y. Xu, "A scalable electrothermal model using a three-dimensional thermal analysis model for GaN-on-diamond high-electron-mobility transistors," *International Journal of Numerical Modelling*, pp. 1-11, 2021.

[112] R. Zhang, W. Zhao and W. Yin, "Investigation on thermo-mechanical responses in high power multi-finger AlGaN/GaN HEMTs," *Microelectronics and Reliability*, vol. 54, no. 3, pp. 575-581, 2014.

[113] A. Wang, S. Martin-Horcajo, M. J. Tadjer and F. Calle, "Simulation of

temperature and electric field-dependent barrier traps effects in AlGaN GaN HEMTs," *Semiconductor Science and Technology,* vol. 30, no. 1, pp. 1-8, 2014.

[114] Powersim, "Knowledge Base," Powersim, [Online]. Available: http://powersimtech.com/resources/knowledge-base/. [Accessed 14 March 2021].

[115] R. P. Ready, *High-frequency GaN-Based Inverter Control Design Using PSIM,* Ann Arbor: Proquest, 2020.

[116] C. K. Liu, H. Lee and T. C. Chang, "The Study of Comparative Characterization between SiC MOSFET and Si- IGBT for Power Module and Three-Phase SPWM Inverter," *Materials Science Forum,* vol. 1004, pp. 1045-1053, 2020.

[117] V. Shevchenko, B. Pakhaliuk, O. Husev, O. Veligorskyi, D. Stepins and R. Strzelecki, "Feasibility Study GaN Transistors Application in the Novel Split-Coils Inductive Power Transfer System with T-Type Inverter," *Energies,* vol. 13, no. 17, p. 4535, 2020.

[118] COMSOL Multiphysics, Semiconductor Module User's Guide, COMSOL Multiphysics, 2016.

[119] M. Ruff, H. Mitlehner and R. Helbig, "SiC devices: physics and numerical simulation," *IEEE Transactions on Electron Devices,* vol. 41, no. 6, pp. 1040 - 1054, 1994.

[120] ROHM Semiconductor, "ROHM Semiconductor SiC Power Devices," August 2014. [Online]. Available: http://rohmfs.rohm.com/en/products/databook/applinote/discrete/sic/common/sic_appli-e.pdf. [Accessed March 2016].

[121] N. M. Ravindra, B. Sopori, O. H. Gokce, S. X. Cheng, A. Shenoy, L. Jin, S. Abedrabbo, W. Chen and Y. Zhang, "Emissivity Measurements and Modeling of Silicon-Related Materials: An Overview," *International Journal of Thermophysics,* vol. 22, no. 5, pp. 1593-1611, 2001.

[122] S. V. Muley and N. M. Ravindra, "Emissivity of Electronic Materials, Coatings, and Structures," *JOM,* vol. 66, no. 4, pp. 616-636, 2014.

[123] A. Plești, "Optimal Heatsink Design for a Solid-State Relay Using a 3D Modeling and Simulation Software," in *International Conference on Power System Technology*, Chongqing, 2006.

[124] A. Raciti, D. Cristaldi, G. Greco, G. Vinci and G. Bazzano, "Electrothermal PSpice Modeling and Simulation of Power Modules," *IEEE Transactions on Industrial Electronics,* vol. 62, no. 10, pp. 6260 - 6271, 2015.

[125] S. Ravikumar, P. S. Chandra, R. Harish and T. Sivaji, "Experimental and Transient Thermal Analysis of Heat Sink Fin for CPU processor for better performance," in *IOP Conference Series: Materials Science and Engineering*, Chennai, 2017.

[126] P. Tarvydas, A. Noreika and Z. Staliulionis, "Analysis of Heat Sink Modelling

Performance," *ELEKTRONIKA IR ELEKTROTECHNIKA*, vol. 19, no. 3, pp. 43-46, 2013.

[127] B. A. Zahn, "Using Design of Experiment Simulation Responses to Predict Thermal Performance Limits of the Heatsink Small Outline Package (HSOP) Considering Both Die Bond and Heatsink Solder Voiding," in *Semiconductor Thermal Measurement and Management Symposium*, San Diego, 1998.

[128] A. J. Morgan, Y. Xu, D. C. Hopkins, I. Husain and W. Yu, "Decomposition and Electro-Physical Model Creation of the CREE 1200V, 50A 3-Ph SiC Module," in *Applied Power Electronics Conference and Exposition (APEC)*, Long Beach, 2016.

[129] GaN Systems Inc., "GS66516T Datasheet," 2017. [Online]. Available: http://www.gansystems.com/gs66516t.php. [Accessed 7 December 2017].

[130] T. Sawamura and T. Igararshi, "Difference Between Various Sn/Ag/Cu Solder Compositions," 29 June 2005. [Online]. Available: www.almit.com/dloads/Agents/SAC%20Alloy%20Comparison.pdf. [Accessed 19 July 2017].

[131] Toshiba, "TK35A65W5," 2017. [Online]. Available: https://toshiba.semicon-storage.com/ap-en/semiconductor/product/mosfets/400v-900v-mosfets/detail.TK35A65W5.html. [Accessed 7 December 2017].